ATTENTION: The Singapore Copyright Act applies to the use of this document. Nanyang Technological University Library

NANYANG TECHNOLOGICAL UNIVERSITY

CAPILLARY WETTING AND INTERFACIAL PHENOMENA IN MICROSTRUCTURES

MILAD RADIOM

SCHOOL OF MECHANICAL AND AEROSPACE ENGINEERING

2010

CAPILLARY WETTING AND INTERFACIAL PHENOMENA IN MICROSTRUCTURES MILAD RADIOM 2010

ATTENTION: The Singapore Copyright Act applies to the use of this document. Nanyang Technological University Library

CAPILLARY WETTING AND INTERFACIAL PHENOMENA IN MICROSTRUCTURES

MILAD RADIOM

School of Mechanical and Aerospace Engineering

A thesis submitted to the Nanyang Technological University in fulfillment of the requirement for the degree of

Master of Engineering

2010

ATTENTION: The Singapore Copyright Act applies to the use of this document. Nanyang Technological University Library

Acknowledgments

It is with great pleasure for me to express my sincere gratitude to my supervisors Prof. Charles Yang Chun and Prof. Chan Weng Kong. Their continuous support and invaluable guidance to carry out this work are highly appreciated. It had been great experience learning from their scholarly advice.

I would like to acknowledge the financial assistance provided by A*STAR Graduate Academy, International Graduate Studies (IGS) in form of a research scholarship.

I also would like to thank Mr. Liu Junting Jason, Mr. Choo Te-Xian Lionel, Mr. Lim Li Tian Eugene and Ms. Chew Mei Ying for their help and contribution in the experimental part of this study. I am also grateful to the laboratory technical staff, Mr. Yuan Kee Hock, from Thermal and Fluids Research Laboratory for his support in the experiments.

My deep heartfelt gratitude goes to my family members for their great sacrifices and moral support.

I would like to extend my warm thanks to all of my friends especially Talebi family who have encouraged me during the project work.

ATTENTION: The Singapore Copyright Act applies to the use of this document. Nanyang Technological University Library

DEDICATED TO

my beloved father, MOHAMMAD HOSSEIN

my beloved mother, SOHEILA

my beloved brother, SOHEIL

ATTENTION: The Singapore Copyright Act applies to the use of this document. Nanyang Technological University Library

Contents

ATTENTION: The Singapore Copyright Act applies to the use of this document. Nanyang Technological University Library

ATTENTION: The Singapore Copyright Act applies to the use of this document. Nanyang Technological University Library

ATTENTION: The Singapore Copyright Act applies to the use of this document. Nanyang Technological University Library

ATTENTION: The Singapore Copyright Act applies to the use of this document. Nanyang Technological University Library

Summary

Fluid penetration into capillary tubes resulting from the interplay between solid-liquid adhesive interactions and liquid-liquid cohesive interactions is a ubiquitous phenomenon. In nature, the rise of underground water in the soil is due to capillary pressure. Moreover, a wide variety of technological applications, e.g. oil extraction through porous rocks, washing process with detergents, surface coating etc, are based fundamentally on capillarity effects. As a result, studies with respect to the physics of capillary flows, both from the engineering and applied sciences and from a theoretical point of view, have been constantly renewed for almost a century.

In addition, carrier liquids containing nano-sized particles are termed as nanofluids that can result in novel thermophysical properties and thus are of practical importance. Many practical applications like underfill flow process in flip chip technology and spin coating involve flow of nanofluids driven by wetting forces. In addition, with the trend towards device miniaturization, cooling of microelectronics with the aid of surface tension driven nanofluid flow has become a potential application. Thus, characterization of the capillarity of nanofluids is essential for flow control purposes in those applications.

In order to better understand the physics involved in the motion of three-phase contact line over a solid surface, this thesis research primarily presents investigations on the capillarity of simple liquids in two novel configurations. Firstly, the capillary filling with the effect of pneumatic pressure of trapped air is studied. The novelty of this work is on the effect of air backpressure on the capillary flow; such a pressure is built up as a result of the air confined within the closed end of the capillary. Both the filling experiment and the theoretical prediction have been done and compared. Secondly, experiment and theoretical study on the

ATTENTION: The Singapore Copyright Act applies to the use of this document. Nanyang Technological University Library

capillary flow from a pendant droplet are performed. The effects of finite sized reservoir on the dynamics of flow are examined. The novelty of this work is on the effect of changes in pendant droplet surface area on the capillary flow, resulting in much faster displacement of the meniscus. Both systems studied herein are of practical importance in techniques employed in the field of microfluidics.

In continuance, surface tension and contact angle, spreading and capillarity of nanofluids are studied. For many years, the physics involved in the shape and contact angle of a droplet on a solid surface has received considerable attention and the physiochemical and physical-statistical parameters controlling surface wettability have been clarified for a long time. For nanofluids, however, there is a lack of systematic studies on the effect of nanoparticles concentration on surface tension, contact angle and wetting behavior. Presence of nano-sized particles within a very thin nanofluid film over the solid surface results in complex flow patterns and new phenomena. The results from the first-part of this thesis research can help to enhance our understanding of the physics involved in the capillarity of nanofluids. Both experiments and theoretical predictions have been conducted and compared.

ATTENTION: The Singapore Copyright Act applies to the use of this document. Nanyang Technological University Library

Nomenclature

A	interface area (m^2)
a	nanoparticles size (m)
AV	attached volume (m^3)
D	capillary tube diameter (m)
D_b	coefficient of particle diffusion due to Brownian motion
D_c	coefficient of particle diffusion due to gradient in particle volume fraction
D_s	coefficient of particle diffusion due to gradient in flow shear rate
F_{AB}	air back pressure force (N)
F_{ST}	surface tension force (N)
F_V	viscous drag force (N)
G	Gibb's free energy of surface (J)
G^*	activation free energy of wetting (J)
g	gravitational acceleration (m/s^2)
g^*	specific activation free energy of wetting (J/m^2)
h	Plank constant (J s)
H	film thickness (m)

ATTENTION: The Singapore Copyright Act applies to the use of this document. Nanyang Technological University Library

K	rate constant in activated rate processes (s^{-1})
	Proportionality factor of power-law non-Newtonian Fluids
K^+, K^-	frequency of displacement of a molecule between two adjacent adsorption cites on a solid surface in forward and backward directions (s^{-1})
K_{net}	net frequency of displacement of a molecule between two adjacent adsorption cites on a solid surface (s^{-1})
K_W^0	equilibrium frequency of displacement of a molecule between two adjacent adsorption cites on a solid surface (s^{-1})
k	dimensionless droplet shape
k_B	Boltzmann constant (J/K)
L	capillary tube length (m)
N_z	particle migration flux (m/s)
n	number of attachment cites per unit area of solid surface (m^{-2})
	Power-law index of non-Newtonian fluids
$\nabla\hat{n}$	unit normal to interface
p_a	air back pressure (Pa)
p_{atm}	atmospheric pressure (Pa)
p_c	capillary pressure (Pa)
Δp	pressure drop across an interface (Pa)

ATTENTION: The Singapore Copyright Act applies to the use of this document. Nanyang Technological University Library

q	flow rate in Darcy's law (m/s)
R	gas constant (J/K)
R_1, R_2	principal radii of curvature (m)
r	capillary radius (m)
T	absolute temperature (K)
t	time (s)
U	mean meniscus velocity (m/s)
U_{max}	maximum meniscus velocity (m/s)
u	meniscus velocity (m/s)
$\bar{u}$	average fluid velocity (m/s)
W	film interaction energy (J/m^2)
W_a^0	equilibrium work of adhesion (J)
w	energy liberated upon motion between two different energy levels (J)
x	meniscus position (m)

Dimensionless Parameters

Bo	Bond number
Ca	Capillary number

ATTENTION: The Singapore Copyright Act applies to the use of this document. Nanyang Technological University Library

Re	Reynolds number
Pe	Péclet number
We	Weber number

Greek Symbols

γ	interfacial tension (N/m)
$\dot{\gamma}$	shear rate (s^{-1})
θ	contact angle
η	viscosity (Pa s)
$\nabla\Phi$	gradient of potential field in Darcy's law (N/m^2s^2)
ϕ	particle volume fraction
υ	volume of the unit flow (m^3)
λ	average distance between the centers of adsorptions cites on solid surface (m)
ζ	frictional coefficient at the meniscus front
κ	interface radius of curvature (m^{-1})
δ_s	Dirac delta function (m^{-1})
ρ	density (kg/m^3)

ATTENTION: The Singapore Copyright Act applies to the use of this document. Nanyang Technological University Library

τ	characteristic time (s)
Π	disjoining pressure (Pa)

Subscripts

d	dynamic behavior
e	equilibrium
	electrostatic
l	local
la	liquid-air
m	molecular
n	nanofluid
p	particle
s	structural
sa	solid-air
sl	solid-liquid
S	contribution of surface effect
s	static condition
t	changing with time

ATTENTION: The Singapore Copyright Act applies to the use of this document. Nanyang Technological University Library

V	contribution of viscous effect
W	wetting process
∞	at equilibrium position

ATTENTION: The Singapore Copyright Act applies to the use of this document. Nanyang Technological University Library

List of figures

ATTENTION: The Singapore Copyright Act applies to the use of this document. Nanyang Technological University Library

ATTENTION: The Singapore Copyright Act applies to the use of this document. Nanyang Technological University Library

ATTENTION: The Singapore Copyright Act applies to the use of this document. Nanyang Technological University Library

ATTENTION: The Singapore Copyright Act applies to the use of this document. Nanyang Technological University Library

ATTENTION: The Singapore Copyright Act applies to the use of this document. Nanyang Technological University Library

List of tables

ATTENTION: The Singapore Copyright Act applies to the use of this document. Nanyang Technological University Library

ATTENTION: The Singapore Copyright Act applies to the use of this document. Nanyang Technological University Library

Publications arising from this thesis

Journal papers

1. M. Radiom, W.K. Chan and C. Yang (2009) *A study of capillary flow from a pendant droplet* Microfluidics and Nanofluidics, vol. 7, no. 5, pp. 697-707.

2. M. Radiom, W.K. Chan and C. Yang (2009) *Capillary filling with the effect of pneumatic pressure of trapped air* Microfluidics and Nanofluidics, Article in Press.

Conference papers

1. M. Radiom, W.K. Chan and C. Yang (2009) *Study of capillary effects from a pendant droplet* 3rd International Conference on Advanced Computational Engineering and Experimenting, Rome, Italy, 22-23 June.

2. M. Radiom, W.K. Chan and C. Yang (2009) *Surface tension driven flow in a closed-end capillary* 3rd International Conference on Advanced Computational Engineering and Experimenting, Rome, Italy, 22-23 June.

3. M. Radiom, C. Yang, and W.K. Chan (2009) *Characterization of surface tension and contact angle of nanofluids* 4th International Conference on Experimental Mechanics, Singapore, 18-20 November. This paper is published in the proceedings of SPIE, Vol. 7522.

ATTENTION: The Singapore Copyright Act applies to the use of this document. Nanyang Technological University Library

Chapter 1: Introduction

1. Background of this study

During the past century, a great deal of research efforts has been devoted to the studies of surface tension driven flows. This interest stems from the dominance of surface tension forces and capillary forces in a variety of physical and natural processes. Examples of these applications are dip-coating of wire for electrical insulation [1-3], and flow of oil through porous rocks in petroleum reservoirs [4]. Also, applications have been extended to lubrication processes [5], and surface cleaning techniques and detergent systems [6, 7]. In addition, use of surface effects has led to a new material processing technique by spraying to form very small droplets that paint and cover a surface uniformly without forming drips and runs.

Furthermore, fluid flow inside capillary tubes is a ubiquitous phenomenon which can be found throughout nature and science in areas ranging from medicine to engineering [8-14]. In medicine, it is possible to determine the presence of diseased red blood cells by observing the dynamic behavior of blood in capillary tubes [15]. The process of sample loading in BioMEMs is another application where tiny doses of medicines can be administered accurately and experiments can be carried out using minute quantities [16].

Along with the development of microfluidics technology and its extensive applications, the importance of understanding the flow behavior in microchannels involved in miniaturized instrument for clinical diagnoses, chemical and biomedical analysis becomes critical [17-19]. As a result, extensive experiments have been conducted, such as liquid rise in capillaries with varying cross sections [20, 21] or heterogeneous (chemically or patterned) walls, and around fibers. Along with these improvements, the dynamics of interface motion, being a

ATTENTION: The Singapore Copyright Act applies to the use of this document. Nanyang Technological University Library

challenging problem in hydrodynamics, received much attention. Thus, theoretical models have been developed to explain the physics involved and to give a clear understanding of these effects. However, despite the extensive experimental and theoretical works, there are several aspects of surface tension driven flows, which have not yet received much attention.

Despite wide applications of nanofluids, little information is available regarding the effect of nanoparticles concentration on surface tension, contact angle and wetting properties. Many practical applications like underfill flow process in flip chip technology [22, 23], spin coating [24], oil recovery and detergent systems [25, 26] may involve flow of nanofluids driven by wetting forces. In addition, with the trend towards device miniaturization, cooling of microelectronics with the aid of surface tension driven nanofluid flow has become a potential application [27, 28]. Thus, characterization of the capillarity of nanofluids is essential for flow control purposes in those applications.

2. The objectives and scope of this work

The characterization of surface tension driven flow in a horizontal closed-end capillary is the first objective of this project. As one end of the capillary is closed, the advancing meniscus is subjected to an increasing backpressure, namely a pneumatic pressure induced by trapped air. It is aimed to investigate the effect of this backpressure on the dynamics of meniscus motion. Capillary flow experiments were carried out for the glycerol-DI water mixture of various glycerol concentrations, with the viscosity ranging 8 to 80 mPa.s in borosilicate glass capillaries having diameters from 200 to 700 μm. As a result of these experiments, the possibility of using pneumatic pressure of trapped air as a new means of controlling interface position and velocity is discussed.

ATTENTION: The Singapore Copyright Act applies to the use of this document. Nanyang Technological University Library

The second objective is to study capillary flow from a pendant droplet (i.e. a finite reservoir). It is aimed to examine the effect of finite sized liquid reservoir on the dynamic behavior of such capillary flow in comparison with the surface tension driven capillary flow from an infinite reservoir. In these experiments, capillaries of 300 to 700 μm in diameter were used with glycerol-DI water solutions having viscosities ranging from 80 to 934 mPa.s. This method is also of practical importance where minute quantities of liquids are introduced in capillary systems, specifically under microgravity condition. These studies not only highlighted some aspects of capillarity which were conventionally ignored but also revealed the physics underlying the movement of the contact line when the liquid spreads over a solid surface.

The third objective of this part of work is to investigate the effects of nanoparticles concentration on the surface tension, contact angle, spreading and capillarity of nanofluids. Experiments were carried out for TiO_2 nanoparticles (15 nm) – DI water nanofluids of various nanoparticle volume concentrations ranging from 0.05% to 2%. With the FTA200 system, the surface tension of these nanofluids was measured by using the pendant droplet method, and the contact angles (both static and dynamic) were determined by using the sessile droplets on a borosilicate glass slide. Capillary filling experiments in three different capillary sizes were performed.

ATTENTION: The Singapore Copyright Act applies to the use of this document. Nanyang Technological University Library

Chapter 2: Literature review

Almost one century ago, interests in capillary driven flows started with the investigation of liquid flow in unsaturated zone of porous media, e.g. soil. It was found that while the liquid wets the solid surface, the pressure within the liquid filled portion of the unsaturated zone is less than the pressure within the gas filled portion. The pressure difference across the interface of the two-phase zones can be directly connected related to the surface tension and curvature of the interface as follows:

$$\Delta p = \gamma \left(\frac{1}{R_1} + \frac{1}{R_2} \right). \tag{2.1}$$

In the above equation, Δp is the pressure difference across the interface, γ is the liquid-gas surface tension, R_1 and R_2 are the principal radii of curvature, and $\left(1/R_1 + 1/R_2\right)$ is the mean curvature of the interface. This fundamental equation is well-known as the Laplace equation[1] [29].

The second fundamental equation was derived by Young [30]:

$$\gamma_{sa} = \gamma_{sl} + \gamma \cos\theta, \tag{2.2}$$

where γ_{sa} and γ_{sl} are the solid-gas and solid-liquid interfacial tensions, respectively, and θ is the contact angle[2]. This equation however holds for equilibrium state and shows balance of the three surface tension forces acting on the triple line (per unit of length of the triple line)

[1] Laplace or Young-Laplace equation ($\Delta p = \gamma \nabla \hat{n}$ where $\nabla \hat{n}$ is a unit normal to interface) is the balance of normal stresses at a point on the interface of two immiscible fluids. In the derivation of this formula, interface is considered as a surface, i.e. of zero thickness.

[2] The angle that the interface of two immiscible fluids makes with the solid surface and is measured toward the denser fluid.

ATTENTION: The Singapore Copyright Act applies to the use of this document. Nanyang Technological University Library

where solid, liquid and gas phases meet. Surface tension and contact angle are the two fundamental properties in interfacial phenomena as they reflect wetting properties of fluids on solid surfaces [31].

The first rigorous analysis of the dynamics of capillary penetration was attributed to Washburn in 1921 [32]. In his pioneering work, Washburn made the following assumptions:

(a) homogeneous tube with uniform cross section,

(b) incompressible Newtonian fluid,

(c) steady-state low Reynolds number viscous flow,

(d) constant contact angle, and,

(e) negligible resistance from driven (gas) phase.

Through many years of capillary flow investigations, these assumptions have been the points of contention of many researchers [33]. Taking these assumptions into consideration, it is possible to derive the equation of meniscus motion by balancing the surface tension force with viscous drag and gravitational forces as follows:

$$2\pi r\gamma\cos\theta = 8\pi\eta x\dot{x} + \pi r^2\rho g x \tag{2.3}$$

and the solution to equation (2.3) is:

$$\bar{t} = -\bar{x} - \cos\theta\ln\left(1 - \frac{\bar{x}}{\cos\theta}\right) \tag{2.4}$$

where $\bar{x} = x/L$ and $\bar{t} = t/T$; and of the reference length L and time T are $2\gamma/\rho g r$ and $16\gamma\eta/\rho^2 g^2 r^3$, respectively. ρ, η, g and r are the density, dynamic viscosity, gravitational acceleration and capillary radius, respectively. For very small gravitational force (microgravity condition), $\bar{x} \ll \cos\theta$ (i.e., $\pi r^2\rho g x \ll 2\pi r\gamma\cos\theta$), and a series expansion to the second order in $\bar{x}$ gives the well-known Washburn equation as follows:

ATTENTION: The Singapore Copyright Act applies to the use of this document. Nanyang Technological University Library

$$\bar{x}^2 = 2\bar{t}\cos\theta. \tag{2.5}$$

Washburn's equation shows that the distance traveled by the interface is proportional to the square root of time, and the proportionality factor is $\sqrt{r\gamma\cos\theta/2\eta}$. In other words, the rate at which a liquid penetrates a horizontal capillary tube (i.e. $dx/dt = r\gamma\cos\theta/4x\eta$, see equation (2.3)) is proportional to the radius of the capillary, cosine of the contact angle, the ratio of the surface tension to the viscosity of the liquid and inversely proportional to the liquid column length.

In 1931, Richards [34] considered adhesive and cohesive interactions[3], respectively between solid-liquid molecules and liquid-liquid molecules, as a means to produce the initial motion of liquid molecules on the dry surface of solid. The inequality between the corresponding adhesive and cohesive forces generates a free energy at the interface boundary. Richards considered two phases in the wetting process. In the initial phase, in which the liquid spreads over a dry surface, adhesive forces are effective in motion and thus determine the angle of contact. After the dry surface adsorbs a thin liquid film, adhesive forces are no longer effective in producing motion, and influence the capillary action only to the extent that the thin film is firmly in contact with the solid surface. The liquid lying outside the adsorbed film is free to move under the action of unbalanced forces like surface tension force due to the curvature of the interface. In other words, it is through the adsorbed film in contact with the solid surface and the curved liquid-gas interface that the capillary flow takes place.

In 1956, Miller and Miller [35] performed an analytical study on liquid motion within pores of a dry medium. They found that the interface shape depends on three fixed factors: pore

[3] Work of cohesion ($2\sigma_l$) is the work necessary to separate unit area of like-molecules within a liquid. Work of adhesion ($\sigma_l + \sigma_s - \sigma_{sl}$) is the work necessary to separate unit area of liquid molecules from solid molecules.

ATTENTION: The Singapore Copyright Act applies to the use of this document. Nanyang Technological University Library

geometry (i.e. channel geometry), surface tension, and contact angle; and on one variable factor: capillary pressure.

Following the pioneering works of Washburn, Richards, and Miller and Miller, in the second half of the twenties century researchers tried to develop rigorous theoretical models of capillary phenomena and wetting kinetics which could illuminate the uncertainties pertaining to Washburn's assumptions. Specifically, what mostly drew researchers' attention was the dynamic behavior in meniscus shape and contact angle (assumption (d)) while the liquid advances on a solid surface. In capillary flow, the driving energy is the out of equilibrium surface tension energy which is balanced by various mechanisms of energy dissipation at the wetting front [33]. The dynamic behavior in contact angle is attributed to these energy dissipative mechanisms which are broadly divided into two different categories: (i) frictional dissipation in the vicinity of the three phase contact line, and (ii) viscous dissipation in the wedge film [36]. Other subjects of research on capillary flows were however related to other Washburn's conventional assumptions.

1. Dynamic contact angle

Molecular kinetic theory

In 1968, Newman [37] studied the kinetics of wetting of polymer melts. He, instead of using the conventional assumption of constant contact angle, employed the following approximate relation for the change in contact angle during capillary penetration:

$$\cos\theta_d = \left(1 - ae^{-ct}\right)\cos\theta_\infty \tag{2.6}$$

ATTENTION: The Singapore Copyright Act applies to the use of this document. Nanyang Technological University Library

where *a* and *c* are adjustable constant, and *e* denotes the exponential function. θ_∞ and θ_d are the equilibrium and dynamic contact angles, respectively. In the past, it was assumed that the development of equilibrium state in contact angle (or meniscus shape) is much faster than the rate of movement of liquid on solid surface, and thus the transient change from initial to equilibrium contact angle does not need to be considered. Inserting equation (2.6) into equation (2.5) leads to the following equation for contact angle:

$$x^2 = \frac{r\gamma\cos\theta_\infty}{2\eta}\left[t - \left(\frac{a}{c}\right)\left(1 - e^{-ct}\right)\right] \tag{2.7}$$

This equation, although giving good results for capillary flow of polymer melts, was found to be incapable of predicting satisfactory results for other liquids.

One year later, Cherry and Holmes [38] investigated the kinetics of wetting of low density polyethylene at 150°C over stainless steel. They stated that the high viscosity of polymer melts dominates the dynamic behavior of contact angle, despite in a less viscous fluid, the effect of the solid surface becomes more important. As a general approach, Cherry and Holmes assumed wetting process as an activated rate process. Using Eyring's theory of absolute reaction rates[4], they obtained the rate constant for such wetting process as follows:

$$K = \left(\frac{2k_B T}{h}\right)\exp\left(\frac{-\Delta G^*}{RT}\right)\sinh\left(\frac{w}{2k_B T}\right) \tag{2.8}$$

where K is the rate constant, ΔG^* is the activation free energy, and $w = xy\,\gamma\left(\cos\theta_{\infty,1} - \cos\theta_{\infty,2}\right)$ is the net energy liberated upon advancement of drop edge from one equilibrium position to the next, x is the distance between two adjacent equilibrium positions and y is the dimension of jumping of the unit of flow in the direction parallel to the

[4] The general form of the Eyring's equation is $k = \left(k_B T/h\right).\exp\left(-\Delta G^*/RT\right)$.

ATTENTION: The Singapore Copyright Act applies to the use of this document. Nanyang Technological University Library

three-phase boundary. k_B, T, h and R are the Boltzmann constant, absolute temperature, Plank constant and gas constant, respectively. For $w \ll 2k_BT$, and considering $d(\cos\theta)/dt$ to be equal to K, and assumption of Eyring's treatment of viscous flow (i.e. $\eta = h/\nu \exp(\Delta G^*/RT)$), Cherry and Holmes rewrote equation (2.8) as follows:

$$\frac{d(\cos\theta)}{dt} = \frac{xy\ \gamma}{\eta\nu}(\cos\theta_\infty - \cos\theta) \tag{2.9}$$

Although the definitions of this approach are very similar to those in the molecular kinetic theory by Blake and Haynes [39] (which will be discussed later), comparisons of Cherry and Holmes' model with experimental results led to unreasonably large values for the characteristic parameter ν/xy.

Blake and Haynes studied the effect from adsorption/desorption of molecules within the interface of two immiscible liquids of low viscosities wetting a solid surface. They obtained an expression which gives the velocity dependence of contact angle in terms of a constant rate at which molecular displacement happens on the solid surface. Although both methods proposed in [38] and [39] are based on the theory of absolute reaction rates (Eyring's theory), the influencing mechanisms are different. Blake and Haynes's work is indeed the advent of the molecular kinetics theory of wetting. Blake and Haynes assumed identical adsorption sites on surface of the solid on which molecules of either liquid may be adsorbed or desorbed. They introduced two frequencies of displacement, K^+ and K^-, respectively in the positive direction and the negative direction as follows:

$$K^{\pm} = \frac{k_BT}{h}\exp\left(\frac{-\Delta g_W^{\pm}}{nk_BT}\right) \tag{2.10}$$

ATTENTION: The Singapore Copyright Act applies to the use of this document. Nanyang Technological University Library

where the specific activation free energies of wetting process in both directions are equal, i.e. $\Delta g_W^{*+} = \Delta g_W^{*-} = \Delta g_W^*$. The additional irreversible work (W, per unit displacement of unit length of the contact line) was approximated as the difference between pressure drop across the interface at a dynamic state ($\Delta p = 2\gamma \cos\theta / r$) and at an equilibrium state ($\Delta p_\infty = 2\gamma \cos\theta_\infty / r$), that is:

$$W = \left| \gamma \left(\cos\theta - \cos\theta_\infty \right) \right| \tag{2.11}$$

where $W = n.\delta w$ in which n is the number of adsorption sites per unit area of the solid surface, and δw is the work equally done on each adsorption site. During contact line motion, W/n alters the energy barriers Δg_W^{*+} and Δg_W^{*-}, lowering one and raising the other, to result in movement of the contact line in a favored direction. Based on this, Blake and Haynes developed the following equation for the net frequency of displacement:

$$K_{net} = \frac{k_B T}{h} \left[\exp\left(\frac{W - \Delta g_W^*}{n k_B T} \right) - \exp\left(\frac{-W - \Delta g_W^*}{n k_B T} \right) \right] \tag{2.12}$$

At equilibrium state $K^+ = K^- = K_W^0$. Introducing λ as the average distance between centers of adsorption sites, they found the following relation for the velocity of the three phase contact line ($u = K_{net} \lambda$):

$$u = 2K_W^0 \lambda \sinh\left[\left(\frac{\gamma}{2nk_B T} \right) . \left(\cos\theta - \cos\theta_\infty \right) \right], \tag{2.13}$$

where

$$K_W^0 = \left(\frac{k_B T}{h} \right) \exp\left(\frac{-\Delta g_W^*}{n k_B T} \right). \tag{2.14}$$

ATTENTION: The Singapore Copyright Act applies to the use of this document. Nanyang Technological University Library

Validity of the above equation was assessed with experiments of benzene and water in glass tubes of 0.2 mm radius.

Hayes and Ralston (1994) [40] examined the molecular kinetic theory of wetting. In their investigation, in order to avoid the uncertainty in experimentally determined equilibrium contact angles due to hysteresis effects, θ_∞ was treated as an additional adjustable parameter which was obtained by curve fitting to experimental data[5]. They stated that this theory is capable of describing both advancing and receding velocity dependence of dynamic contact angle as well as contact angle hysteresis satisfactorily.

Hamraoui et al. [41] interpreted the molecular kinetics definition of energy dissipation in terms of a friction factor (ζ) at the moving front as follows:

$$\zeta = \left(\frac{k_B T \upsilon n}{2\pi\lambda K_W^0 h} \right) \eta \tag{2.15}$$

They studied the kinetics of capillary rise of pure water, ethanol and their mixtures in prewetted and dry glass capillaries of radius 0.295 mm. It was shown that the dynamics of capillary penetration can be strongly influenced by the dynamic nature of contact angle. They claimed that the wetting front of the liquid changes the surface properties of the substrate in a finite time by reorientation of liquid molecules on the solid surface (see refs. [36, 42]). If this time is less than the time scale of contact line motion on the solid surface, the contact angle is no longer constant. Their results show that at the initial stage of the capillary rise, the liquid moves faster and it can precede the precursor film. Then, it is expected to observe a quasi-static contact angle. In continuance, Hamraoui and Nylander [43] performed more extensive experiments and their results showed a strong dependence of contact angle on the velocity of

[5] This is noted that in the present project the same approach is adopted in order to obtain values of equilibrium contact angle for each experiment.

ATTENTION: The Singapore Copyright Act applies to the use of this document. Nanyang Technological University Library

the meniscus. Moreover, they proposed that the frictional coefficient ζ (which dominates the dynamics of motion) is intrinsic of liquid-solid molecular interactions, and is independent of the solid geometry.

In 2002, Blake and De Coninck [44] developed new concepts on the molecular kinetic theory of Blake [39]. They stated that the molecules within the three-phase zone are resisted by two effects: interactions due to adsorption (i.e. solid-liquid molecular interactions) and interactions due to viscosity (i.e. liquid-liquid molecular interactions). As a result, the specific activation free energy of wetting (Δg_W^*, see equation (2.14)) is a combination of two terms: viscous interaction energy (Δg_V^*) and surface interaction energy (Δg_S^*). Based on this, they developed the following equation for the contact line velocity:

$$u = \frac{2k_B T \lambda}{\eta \upsilon} \exp\left[\frac{-\gamma.(1+\cos\theta_\infty)}{nk_B T}\right].\sinh\left[\frac{\gamma}{nk_B T}.(\cos\theta_\infty - \cos\theta)\right] \qquad (2.16)$$

θ_∞ can influence the driving force which helps in wetting (sinh argument) as well as the adsorption which conversely resists wetting (exp argument), thus rendering an intermediate level of interactions between solid-liquid molecules. It is obvious from the form of this equation that for strong solid-liquid interactions, i.e. small θ_∞, the driving force for wetting ($\gamma(\cos\theta_\infty - \cos\theta)$) increases, but at the same time the resistance to wetting ($\gamma(1+\cos\theta_\infty)$) increases too. Conversely, weak solid-liquid interactions will reduce both of them. Comparisons with experimental data show that these two opposing effects do not simply cancel out and as a result, the equilibrium contact angle should remain at some intermediate values. The details of this equation which is used in the present study to interpret the dynamic contact angle will be discussed in the next chapter. For small argument of sinh, and

ATTENTION: The Singapore Copyright Act applies to the use of this document. Nanyang Technological University Library

considering $\gamma\left(\cos\theta_{\infty}-\cos\theta\right)=\zeta\times u$ (see ref. [41]), it is possible to write the following equation for the frictional coefficient at the wetting front:

$$\zeta=\frac{\eta\upsilon}{\lambda^{3}}\exp\left[\frac{\gamma\left(1+\cos\theta_{\infty}\right)}{nk_{B}T}\right] \tag{2.17}$$

Later in 2003, Martic et al. [45] investigated the influence of dynamic contact angle on the characterization of porous media and estimation of the effective pore radius. They stated that the value of ζ depends on the relative strength of adsorption and liquid-liquid viscous interactions and is in the range of one to three orders of magnitude greater than the bulk dynamic viscosity (η) as found in the literature.

In 2007, Vega et al. [46] used equation (2.17) to study forced wetting of nylon filament. Comparison with experimental data confirmed the validity of equation (2.17) (see also refs. [47-51]).

Hydrodynamic theory

As discussed earlier, in contrast to the molecular kinetics approach, hydrodynamic models of spreading consider viscous friction in the wedge film to be the only significant dissipative mechanism leading to a dynamic behavior in contact angle. According to hydrodynamic models of spreading, no-slip boundary condition is required all over solid-liquid interfaces except at the moving front. When no-slip boundary condition is applied to the contact line, the velocity field appears realistic but viscous stresses and the resulting energy dissipation increase with no bound which is unrealistic [36]. In order to solve this problem, hydrodynamic models consider two or three regions in the moving liquid film: inner, intermediate and outer regions [33]. The inner region (precursor film) is in the immediate proximity to the contact line with a characteristic length comparable to slip length, namely

ATTENTION: The Singapore Copyright Act applies to the use of this document. Nanyang Technological University Library

10^{-11} to 10^{-2} mm. Conventional hydrodynamic theories cannot describe the precursor film, and thus either it is excluded from calculations or slip boundary condition is allowed in order to remove the viscous stress singularity [33]. Flow characteristics and shape of fluid interface are determined as balance of capillary and gravitational forces in the outer region and balance of balance of capillary and viscous drag forces in the intermediate region [33].

An example of these studies is the pioneering work by Huh and Scriven (1970) [52]. They applied the creeping flow model to a perfectly flat solid surface which was translated by a velocity U (mean meniscus velocity) from a perfectly flat fluid interface. The model resulted in the following viscous stress expression for a liquid-gas interface:

$$\tau_{r\theta} = \frac{2\eta}{r}\left(\frac{3U}{2\theta}\cos\theta - \frac{3U}{2\theta^2}\sin\theta\right) \tag{2.18}$$

It is obvious that the viscous stress is a function of r^{-1}, leading to infinite increase in energy dissipation as the contact line is approached.

In 1971, Phillips and Riddiford [53] used water, glycerol, formamide and methylene iodide on glass substrates coated with a dimethyl siloxane layer to investigate the effect of contact line velocity on the advancing and receding dynamic contact angles. The authors found that hydrodynamic theories cannot account for the effects exerted by solid surface on the meniscus including surface forces and molecular processes involved in the spreading of liquid over a solid surface. They stated that the initial rapid reorientation and subsequent penetration of liquid molecules on the solid surface can change the solid-liquid interfacial tension and are two factors controlling contact angle during spreading process, see ref. [54].

Voinov (1976) [55] studied the velocity dependence of dynamic contact angle in the cases of low Reynolds number. For flows inside a capillary tube, excluding the so-called the precursor

ATTENTION: The Singapore Copyright Act applies to the use of this document. Nanyang Technological University Library

film, he obtained the following expression for the dynamic contact angle through a hydrodynamic function:

$$\theta_d^3 = \theta_s^3 + 9\mathrm{Ca}\left[\ln\left(\frac{L}{L_S}\right) - 1.83\right] \tag{2.19}$$

where L is the experimentally accessible macroscopic distance from which the dynamic (apparent) contact angle can be measured, L_S is a limiting small length scale (several folds of the size of a liquid molecule) at which it is not possible to use the hydrodynamics theory, and θ_s is defined as the angle of slope to the interface at height L_S vertical to the solid wall. According to this definition, θ_s, the invisible (microscopic) contact angle at the vicinity of three-phase contact line, is always constant regardless of the velocity of motion and the changes in the apparent dynamic contact angle. As a result of this equation, for sufficiently small velocities, the viscous dissipation is negligible and for all $L > L_S$, $\theta_d = \theta_s$, see ref. [53].

Based on the molecular dynamics simulation, Thompson and Robbins [56] stated that the degree of change in interface shape near the contact line depends on an interplay between the viscous dissipation and the energy required to distort the interface. They also stated that the hydrodynamic theory breaks down at atomic length scales near the interface (namely 2 atomic spacing from the contact line) where the slip boundary condition should be assumed; at larger distances, no-slip boundary condition is again satisfied. They also found consistency with Cox's (1986) [57] hydrodynamic equation:

$$g(\theta) - g(\theta_s) = \mathrm{Ca}\left[\ln\left(\frac{L}{L_S}\right) + Q\right] \tag{2.20}$$

where Q depends on the slip and macroscopic boundary conditions, and g is a complex integral function. It is noted that in case that the displaced fluid is very low viscous, e.g. air,

ATTENTION: The Singapore Copyright Act applies to the use of this document. Nanyang Technological University Library

the function $g(\theta)$ can be approximated as $\theta^3/9$ for $\theta < 3\pi/4$, and the above equation can be written as follows (see the equation developed by Voinov [55] for comparison):

$$\theta^3 = \theta_\infty^3 + 9\mathrm{Ca}.\ln\left(\frac{L}{L_S}\right) \tag{2.21}$$

In 1980, Levine et al. [58] matched regions of no-slip boundary condition (at the bulk liquid) and slip boundary condition (at the contact line) by the method of inner and outer expansions. In addition, at the meniscus, the tangential shear stress was set to zero and the continuity of normal stress was approximated by assuming a fixed contact angle. They found that the assumption of meniscus slippage adds an extra drag equal to $8\pi\eta\dot{x}.\left(f(a)+ae\right)$ in the vicinity of the three-phase contact line.

In 1997, Shikhmurzaev [59] developed a new hydrodynamic theory of wetting taking into consideration of deviation of interfacial tensions at the immediate vicinity of the contact line from their equilibrium values (e.g. as used in the Young's equation (2.2)). He described that the deviation from equilibrium values is due to relaxation from a previous equilibrium state to a new equilibrium state in the transformation of liquid molecules from liquid-fluid interface to liquid-solid interface, and the subsequent travel through the three phase zone. Properties of liquid-fluid interface will not be the same as those of the liquid-solid interface. As a result, surface tension gradient in the neighborhood of the moving contact line and along the interface will be produced. Although this approach is very important due to the physics which are involved in its derivation and gives comparably good prediction of experimental data, the complexity of the formulation has limited its application (see for example ref. [60]).

ATTENTION: The Singapore Copyright Act applies to the use of this document. Nanyang Technological University Library

Molecular kinetics theory vs. hydrodynamic theory

In 1985, Mumley et al. [61, 62] performed experimental and theoretical investigations on the kinetics of liquid-liquid capillary rise. The displacing liquids were solutions of glycerol-water of different concentrations and the displaced liquids were pure hydrocarbons ranging from light to polymeric. Glass capillaries were treated in three different ways to produce dry, prewet and prewet-dried[6] surfaces. For all liquid pairs, values of interfacial tensions did not vary greatly, ranging from 28.2 to 33.9 $mN.m^{-1}$, but viscosity ratio of the displacing liquid to the displaced liquid varied from 0.4 to 232. The authors reported that the meniscus shape changed during the capillary rise even in the prewet capillaries. At the highest speeds near the entrance, the shape was blunter and at slower speeds it was like a spherical cap. The authors attributed the dynamic behavior in contact angle to hydrodynamic force in the macroscopic film near the interface, secondary microscopic film above it, and solid surface effects on the preceding molecular film[7]. The last effect is however attributed to surface adsorption-desorption and possible surface diffusion whenever displaced liquid molecules are moved by displacing liquid molecules with influences related to surface energy barriers and microroughness. The first and second effects which are pertaining to hydrodynamic forces act severely near the moving meniscus where radial flow and possible vortices may happen for continuity. Such circulating patterns tend to flatten the meniscus and increase the apparent (dynamic) contact angle and act as an additional energy dissipation mechanism [36]. The values of these excess forces at high capillary numbers were found to achieve 70% of the driving surface tension force [62].

[6] After cleaning process, the interior of capillaries were suction-dried by connecting it to vacuum (dry surface). Dry tubes were first filled with the wetting liquid. The wetting liquid was then displaced out. As a result of this, a thin film remained on the interior surface of the glass tube (i.e. prewet surface). For the case of prewet-dried tubes, the liquid within a prewet tube was drawn out by vacuum until the glass appeared dry. Here, a very thin molecular film of liquid would remain on the interior surface of the glass tube (i.e. prewet-dried surface).

[7] The latter is the basis of molecular kinetics theory (MKT) of dynamic contact angle.

ATTENTION: The Singapore Copyright Act applies to the use of this document. Nanyang Technological University Library

Petrov and Petrov (1991 and 1992) [63, 64] performed extensive experiments with water and aqueous glycerol solutions on a PET solid surface; velocities ranging from 0 to 3×10^{-3} cm.s^{-1}, and up to 1×10^{-3} cm.s^{-1} for more viscous liquids were obtained. They observed a region of constant contact angle, so-called plateau, during which advancing and receding contact angles remained constant independent of contact line velocity. In comparison with theory, they found that the molecular kinetic theory of Blake and Haynes [39] (equation(2.13)) gives the best trend. They also examined the hydrodynamic theory of Cox [57] (equation (2.21)), which assumes viscous effects to be the only channel of energy dissipation, and found that the hydrodynamic model predicted physically unreasonable values for its characteristic parameter, i.e. slip length L_S, smaller than atomic dimensions. They also found that the hydrodynamic theory did not give a good trend in comparison with their experimental data.

Further, Petrov and Petrov (1992) [65] proposed a new model describing the wetting kinetics on the basis of both hydrodynamic theory and molecular kinetic theory, as follows:

$$g(\theta)-g(\theta_s(u))=\mathrm{Ca}.\ln\left(\frac{L}{L_S}\right) \tag{2.22}$$

In this model, the static contact angle in the hydrodynamic approach (see ref. [57]) is considered to be dynamic, being a function of velocity, i.e. $\theta_s(u)$; and the change in its value is attributed to the molecular kinetic theory [39], as follows:

$$\theta_s(u)=\arccos\left[\cos\theta_\infty+\left(\frac{2nk_BT}{\gamma}\right)\mathrm{arsh}\left(\frac{u}{2K_W^0\lambda}\right)\right] \tag{2.23}$$

Combination of the above two equations results in three adjustable parameters, L_S, K_W^0, and λ. Comparison with experimental data showed good agreement, although the curve fitted values of L_s resulted in unreasonable small values for the slip length.

ATTENTION: The Singapore Copyright Act applies to the use of this document. Nanyang Technological University Library

In 1993, Sedev et al. [66] investigated the capillary rise of octane, dodecane, and hexadecane. Solid surfaces were mica dip-coated with a fluorocarbon polymer in three different surface conditions: dry, prewet, and soaked. They found that dynamic contact angle depends not only on the contact line velocity but also on the duration of the solid-liquid contact and on the local degree of solid surface modification (see ref. [61, 62]). Noting the existence of plateaus at low velocities, they stated that neither the hydrodynamic approach of Cox [57], nor the molecular kinetic theory of Blake [39] can describe the whole range of their data on velocity dependence of dynamic contact angle. They also found that, the quantitative agreement of the molecular kinetic theory is much better than the hydrodynamic theory.

In 1997, Ruijter et al. [67] studied relaxation of dynamic contact angle in spreading of a liquid droplet over a solid surface. They compared the predictions of molecular kinetic theory and hydrodynamic theory with experiment in which glycerol-water solutions, DBP, and squalane were used over PET and glass slides. The results showed that the molecular kinetic theory was successful in modeling this phenomenon and the characteristic parameters had physically meaningful and consistent values. The authors claimed that the nature of the liquid, i.e. its molecular volume, has influence on the site density, n, and molecular displacement length, λ. The characteristic parameter of hydrodynamic theory, slip length, was found to be in order 10^{-20} to 10^{-10} mm which is entirely nonphysical and inconsistent. Referring to this, the authors insisted on the existence of a non-hydrodynamic process in the three phase zone.

2. Experimental studies on meniscus velocity profile

In 1978, Jeje [68] studied spontaneous capillary rise in which neither Poiseuille's velocity profile approximation was adequate nor could the inertia term be neglected. Glass capillary

ATTENTION: The Singapore Copyright Act applies to the use of this document. Nanyang Technological University Library

tubes of diameters ranging 266 to 1191 μm were used in vertical and horizontal orientations and the rates of capillary penetration was determined with the aid of a high-speed camera. Comparison of experimental velocities with prediction of Washburn's equation (2.5) showed that the assumption of developed laminar flow is not consistent with the real flow at the entrance of the capillary, and specifically in the immediate wake of the liquid meniscus. He also found that in the initial stages of capillary rise the mean velocity falls with time in a logarithmic trend for the horizontal arrangement and linearly for the vertical arrangement. The duration of these flow patterns (which cause deviation from Washburn's equation) was found to be very short, and consequently they have negligible effects on the whole liquid penetration. Moreover, Jeje noted that when the tubes were partially dried out, the meniscus motion was retarded or stopped completely at some points within the capillary tube; such effect which is due to the local changes in surface tension of solid surface, had been reported previously in the work of Miller and Miller [35]. In our experiments, we also observed the same kind of behavior, but since this anomaly behavior is regarded likely as experimental errors; the data are not presented in this project (more details on the solution to this problem can be found in experimental section of this thesis).

In 2000, Siebold et al. [69] performed experiments on the capillary rise of different alkanes in glass capillaries of a radius 191±1 μm and in columns of packed powders. They found that the initial stage of capillary rise had deviation from Washburn's equation (i.e. $x^2 \sim t$ see equation (2.5)); the range of this deviation was increased by the ratio γ/η. The time duration of this deviation was found to be less than 10 ms, close to the theoretical relaxation time from inertia dominancy to viscous dominancy, i.e. $\tau = \rho r^2/4\eta$, see ref. [70]. Experiments showed that although the tested liquids were wetting liquids on glass, their contact angles were always larger than the expected zero contact angle, depending strongly on the rising velocity. In the same year, Zhmud et al. [71] also studied the different classical approaches to the

ATTENTION: The Singapore Copyright Act applies to the use of this document. Nanyang Technological University Library

solution of capillary rise problem with consideration of nonlinear dissipation and flow pattern effects near the meniscus and the capillary entrance. They performed experiments using different hydrocarbons as test liquids in hydrophobized borosilicate glass capillaries of radii 0.1, 0.15, 0.25 and 0.5 mm.

In 2003, Stange et al. [72] developed a general model for capillary rise with consideration of meniscus reorientation, dynamic contact angle, inertia effect, convective and viscous losses. In their rigorous theoretical work, they divided capillary flow into three successive phases during which, first inertia, then convective losses and finally viscous forces resist the capillary force. Based on this, they captured the time domain before which the height and time square root proportionality of Washburn's equation (2.5) did not exist. They stated that the respective transition between these flow regimes happens at time scales:

$$t_1 \sim \sqrt{\frac{\rho r^3}{\gamma}} \tag{2.24}$$

which is 0.5 ms for water in 500 µm, and

$$t_2 \sim \frac{\rho r^2}{\eta} \tag{2.25}$$

which is 1 ms for water in 500 µm.

3. Surface tension driven flow from a finite reservoir

As discussed earlier, study on the dynamics of capillary penetration was initiated by Washburn in 1921. His theoretical model assumed quasi-steady state, laminar flow from an infinite reservoir with negligible inertia effects and a constant contact angle [32]. As reviewed so far, through many years of capillary flow studies, many experiments have been

ATTENTION: The Singapore Copyright Act applies to the use of this document. Nanyang Technological University Library

conducted to examine Washburn's assumptions. However, the two latter assumptions have always been the focusing points by many researches. A basic assumption which has not been paid much attention is the size of liquid reservoir. Many practical applications, such as coating deposition, printing, and wicking in textile yarn systems, involve capillary penetration from a finite sized liquid reservoir. Thus, studying the effect of reservoir size and the subsequent change in reservoir volume and surface area in the process of capillary penetration is of practical importance.

In 1988, Marmur [73, 74] performed a theoretical study on the penetration of a small spherical drop into a capillary. He found that the height of capillary rise and the rate of penetration by a drop of finite size are higher than those for an infinite liquid reservoir. He stated that these effects stem from the increased pressure inside the drop due to its curvature (according to Laplace equation (2.1)). As a result of this pressure and for sufficiently small drops, he showed that penetration occurs in a horizontal capillary even for contact angles about 114^{o}, but the penetration volume decreases for higher values of contact angle. Further, assuming that during this process the outer surface of the tube does not wet and the liquid reservoir keeps its spherical shape, Marmur proposed the following equation:

$$(p_0 + \frac{2\gamma}{R}) + (\frac{2\gamma\cos\theta}{r} - p_0) > 0 \tag{2.26}$$

in which R is the droplet radius. With regard to this equation at equilibrium condition, $(p_0 + 2\gamma/R_\infty) + (2\gamma\cos\theta_\infty/r - p_0) = 0$, and it follows that penetration takes place when $1/R > 1/R_\infty$.

Nevertheless, later investigations pertaining to penetration from a finite reservoir did not consider the curvature and corresponding pressure effect [75, 76]. Thus, in order to elucidate this subject, more qualitative and quantitative efforts are needed [77-79].

ATTENTION: The Singapore Copyright Act applies to the use of this document. Nanyang Technological University Library

4. Capillary flow in nanochannels

Due to the large surface to volume ratio, capillary action is the dominant factor in filling of nanochannels, (see for example ref. [80] as a review on wetting phenomena in nanofluidics). In 2000, Sobolev et al. [42] employed the conventional experimental techniques using water in quartz cylindrical capillaries of radius ranging from 40 to 200 nm. The authors stated that the contact angle depends on the velocity of meniscus motion. However, at high velocities, the contact angle becomes practically rate independent, and this is because the precursor film does not have enough time to form in front of the moving meniscus on the solid surface (see ref. [36]). As a result, the meniscus meets a dry surface with the same interfacial condition and the contact angle takes a constant value (the same plateau in velocity dependence of dynamic contact angle had been previously reported in [50, 63-65]). Contact angles were also found to be larger in smaller radius capillary. In contrast to hydrodynamic theory, the molecular kinetic theory gave a good prediction of dynamic contact angle.

5. Capillary flow behavior of nanofluids

For many years, the physics involved in the shape and contact angle of a droplet on a solid surface has received considerable attention [36, 47, 81]. The physiochemical parameters controlling surface wettability have been clarified for a long time, and the physical-statistical parameters resulting in hysteresis in contact angle, like contact line pinning and dry spreading, also have been studied [36]. For nanofluids, however, there is a lack of systematic studies on the effects of nanoparticles concentration on surface tension, contact angle and wetting behavior. Despite several theoretical studies [26, 82-84], very limited experimental investigations were reported, such as Vafaei et al. [85] on the size and concentration effects of bismuth telluride nanoparticles on equilibrium contact angle of DI water-based nanofluids

ATTENTION: The Singapore Copyright Act applies to the use of this document. Nanyang Technological University Library

and Sefiane et al. [86] on the spreading behavior of aluminum – ethanol nanofluids over hydrophobic Teflon – AF coated substrates.

In addition, the general steady-state equation of contact line motion can be written as follows:

$$\nabla p = \nabla.\left(\eta_n \nabla u\right) \tag{2.27}$$

in which the surface tension stress is included in ∇p term, and η_n is the nanofluid viscosity. Based on one-dimensional simplification and assumption that the surface tension is the only driving stress, equation (2.27) can be rewritten as follows:

$$\frac{2\gamma\cos\theta}{rx} = \frac{\partial}{\partial y}\left(\eta_n \frac{\partial u_x}{\partial y}\right) \tag{2.28}$$

This equation shows that one model for the capillarity term and one model for the viscous stress term are needed. Extensive discussions on the capillarity are provided in the previous literature review. However, performing a complete dynamic simulation of nanofluids, due to a wide range of interparticle and intermolecular interactions (e.g., hydrodynamic interactions, electrostatic interactions, and other related surface and film interactions), is impossible in practice. Hence, equation (2.27) should be revised to include one or some of these effects. For example, a constitutive model, which is based on the essential physics of suspensions, should be developed for the viscous stress term (i.e. rheological model). In addition, the driver stress is not only the free energy of interface, but also the film interaction energy in the film formed in front of the apparent meniscus. A model should also be developed to capture this film effect. Both viscous and film interaction models should be simple enough to be used in flow simulations.

ATTENTION: The Singapore Copyright Act applies to the use of this document. Nanyang Technological University Library

6. Viscosity of nanofluids

The rheology of suspensions is well described by assuming the viscosity to be function of particle volume fraction (ϕ) and local shear rate ($\dot{\gamma}$) as follows:

$$\eta_n\left(\phi,\dot{\gamma}\right)\nabla^2 u. \tag{2.29}$$

However, in many experiments with nanofluids, Newtonian behavior (i.e. shear rate independency of viscosity) was observed especially for high shear rates. For this reason, the shear rate term in equation (2.29) is usually dropped, and effective viscosity is considered to be only a function of solid volume fraction. Effective and practical functions are reported for the effective viscosity as a function of ϕ, such as Kreiger's formula [87]:

$$\eta_n = \eta_l\left(1-\frac{\phi}{\phi_{\max}}\right)^{-2.5\phi_{\max}}, \tag{2.30}$$

Leighton and Acrivos' formula [88],

$$\eta_n = \eta_l\left(1+\frac{1.5\phi}{1-\dfrac{\phi}{\phi_{\max}}}\right)^{p}, \tag{2.31}$$

and Morris and Boulay's formula [89]:

$$\eta_n = \eta_l\left(1+2.5\phi\left(1-\frac{\phi}{\phi_{\max}}\right)^{-1}+0.1\phi^2\left(1-\frac{\phi}{\phi_{\max}}\right)^{-2}\right). \tag{2.32}$$

ATTENTION: The Singapore Copyright Act applies to the use of this document. Nanyang Technological University Library

where η_l is the carrier liquid viscosity, and ϕ_m is the fluidity limit which is empirically equal to 0.68 for hard spherical particles [90]. It is noted that although the above formulations have been developed for micro-particles in carrier liquids, they are also extended to nanofluids.

In fact, addition of nanoparticles will enhance viscosity drastically. Wang et al. (1999) [91] studied viscosity of Al_2O_3 (28 nm) – water and Al_2O_3 – ethylene glycol nanofluids and found increment of 86% for 5% volume concentration and increment of 38% for 3.5% volume concentration respectively.

Prasher et al. (2006) [92, 93] studied the effects of nanoparticle size, temperature and volume fraction on viscosity of alumina-based nanofluids in propylene glycol. A non-Newtonian behavior was observed for shear rates ranging from 0.7 to 100 s^{-1}. However, for larger shear rates, the viscosity remained effectively constant, namely independent of shear rate. Measurements showed that the effective viscosity is independent of particle size, but has a weak dependence of temperature. Moreover, it was observed that the viscosity changes linearly with solid volume fraction:

$$\frac{\eta_n}{\eta_l} = 1 + C_\eta \phi \tag{2.33}$$

in which C_η (enhancement coefficient) was found to be about 10.

Schmidt et al. (2008) [94] studied the effects of agglomeration and clustering of nanoparticles on the viscosity of alumina based nanofluids in decane and isoparaffinic polyalphaolefin (PAO). For nanoparticle volume fractions ranging from 0.25% to 1%, enhancement in viscosity due to clustering of nanoparticles were found. Newtonian behavior on shear rates ranging from 0.33 to 3270 s^{-1} was also observed.

ATTENTION: The Singapore Copyright Act applies to the use of this document. Nanyang Technological University Library

It is noted that although Newtonian behavior was reported in almost all recent experiments on nanofluid viscosity [95-97], the observed shear rate had been in off-range of obvious non-Newtonian behavior. It is known that the non-Newtonian behavior of shear-thinning (or shear-thickening) fluids is shear-rate range dependent. For shear rates higher or lower than this range, Newtonian behavior is always observed. Previous experiments were basically for heat transfer applications in which the shear rate is much higher than the shear rate in surface tension driven flows. Thus attention needs to be paid on viscosity of nanofluids in low shear rates, namely less than 50 s^{-1} [98].

Diffusion of nanoparticles in channel flow

Equations (2.30) to (2.32) (all precluding the shear thinning term) show that η_n is a function of solid volume fraction. Thus, this is necessary to construct a mass transport equation for spatial distribution of ϕ based on conservation of particle mass (or volume) as follows:

$$\frac{\partial \phi}{\partial t} + \frac{\partial}{\partial x}\left(u\phi\right) = -\nabla \cdot N_z \tag{2.34}$$

The second term on the left hand side of equation (2.34) shows convection along flow streamlines. On the right-hand side, particle migration flux normal to streamlines is represented by N_z which is a combination of different irreversible mechanisms of particle migration. Leighton and Acrivos (1987) [88] proposed an expression for N_z based on spatially varying interparticular interaction frequency and spatially varying effective viscosity. This expression as modified by Phillips et al. (1992) [90] with the addition of Brownian flux is as follows:

$$N_z = -D_c \nabla \phi - D_s \nabla \dot{\gamma} - N_g + N_b \tag{2.35}$$

ATTENTION: The Singapore Copyright Act applies to the use of this document. Nanyang Technological University Library

where D_c and D_s are the coefficients of diffusion due to gradients in ϕ and $\dot{\gamma}$, respectively. N_g is the settling flux which arises from the difference between particle and liquid densities. $N_b = -D_b \nabla \phi$ accounts for Brownian diffusion of the particles with D_b as the Brownian diffusion coefficient.

The empirical correlations for D_c and D_s are as follows:

$$D_c = a^2 \dot{\gamma} \left(0.43\phi + 0.65\phi^2 \frac{1}{\eta_n} \frac{d\eta_n}{d\phi} \right)$$
$$D_s = 0.43 a^2 \phi^2 \tag{2.36}$$

with equation (2.30) for η_n [90]; and

$$D_c = a^2 \dot{\gamma} \left(\tfrac{1}{3}\phi^2 \left(1 + \tfrac{1}{2} e^{8.8\phi}\right) + 0.6\phi^2 \frac{1}{\eta_n} \frac{d\eta_n}{d\phi} \right)$$
$$D_s = 0.6 a^2 \phi^2 \tag{2.37}$$

with equation (2.31) for η_n [88, 99]. In addition, the Brownian diffusion coefficient is given by the Stokes-Einstein equation as follows:

$$D_b = \frac{kT}{6\pi \eta_l a} \tag{2.38}$$

A further insight shows that the first term on the right hand side of equation (2.35) accounts for particle migration from regions of high particle concentrations to low particle concentrations, and the second term represents particle migration from regions of high shear rate to low shear rate. These two terms generally oppose each other [90]. Combination of these effects is so-called the shear-induced diffusion. Despite the extensive investigations pertaining to non-Brownian suspension flow for over a decade, there has been little attention given to particle migration in flow of Brownian suspensions. However, aspects of the

ATTENTION: The Singapore Copyright Act applies to the use of this document. Nanyang Technological University Library

rheology of Brownian suspensions are well studied at late last century [100, 101]. It is known that for monomodal dispersions, the Brownian suspension is well characterized by the Péclet number (Pe) [102]:

$$Pe = \frac{6\pi\eta_l \dot{\gamma} a^3}{kT} \tag{2.39}$$

The Péclet number is the ratio of shear-driven to Brownian (thermal) motion at the particle scale. Conceptually, the Péclet number is the time ratio of Brownian diffusion to shear induced diffusion. Small values of the Péclet number, namely less than 10^{-4}, show uniformity in distribution of solid particles. Table 2-1 shows the dominancy of Brownian diffusion when the suspension is a nanofluid. As a result, for the nanofluids, the shear induced particle migration has less effect comparing to Brownian diffusion, and nanoparticles are evenly distributed in the bulk liquid by the Brownian motion.

Table 2-1: Comparison between different diffusion coefficients for mirco- and nano-particles; $\phi = 0.01$**,** $\dot{\gamma} = 100\ \mathrm{s}^{-1}$**, and** $\eta_l = 10^{-3}$ Pa s **.**

Particle size (a)	D_c (equation (2.36))	D_s (equation (2.36))	D_b (equation (2.38))	Pe (equation (2.39))
1 µm	4e-013	4e-017	2e-013	466
1 nm	4e-019	4e-023	2e-010	5e-7

ATTENTION: The Singapore Copyright Act applies to the use of this document. Nanyang Technological University Library

7. Surface tension of nanofluids

Capillarity of nanofluids

In 2001, Aussillous and Quere [103] tried to overcome the difficulties associated with the levitation of droplets on solid surface by adding hydrophobic powders (lycopodium grains of 20 µm size covered with fluorinated silanes) to mixtures of water and glycerol. Consequently, the adhesion of the resulting fluid was dramatically reduced, and thus the very small viscous friction led to rapid displacement of droplet. This study, indeed, evaluates the significance of encapsulated solid phase in liquid phase on the hydrodynamics of capillarity of nanofluids [104]. Successful formation and stability of these liquid marbles is a new area of study [105] and a number of variables in addition to powder hydrophobicity, namely powder density, size and shape, and formation techniques are currently under investigations.

Vafaei et al. [106] (2006) studied the effect of nanoparticle size and concentration on equilibrium contact angle. DI water-based nanosuspensions of 2.5 and 10.4 nm bismuth telluride nanoparticles with concentrations of up to 0.04% vol. were used in their experiments. They found that due to the presence of nanoparticles, the equilibrium contact angle was increased significantly comparing to base liquid. For smaller particles in a same concentration, the increase in contact angle was however more significant. As the concentration increased, the contact angle was found to increase first, but then decrease for higher concentrations. The authors related this phenomenon to electrostatic interactions between charged particles and water molecules in addition to the interparticular interactions; both effects are pertaining to particles' size and concentration.

In 2008, Sefiane et al. [86] studied spreading behavior of aluminium-ethanol nanofluids on hydrophobic Teflon-AF coated substrates. To analyze the effect of particle concentration on

ATTENTION: The Singapore Copyright Act applies to the use of this document. Nanyang Technological University Library

contact line velocity, they performed experiments under constant external driving forces. Enhancement was found in contact line velocity for concentrations up to 1% by weight (0.3% by volume). In addition, although the contact line velocity decreased for higher concentrations (up to 5% by weight or 1.5% vol.), it never fell less than the value for the contact line velocity of pure glycerol. This is in direct contrary to the fact that the viscosity of liquid increases significantly when solid particles are added - the higher is the particle concentration, the higher is the viscosity. Nevertheless, this finding supports the fact that the presence of nanoparticles should have direct effect on contact line motion. Two mechanisms are reported to attributed in this behavior: first, the enhanced disjoining pressure due to the ordering of nanoparticles in the vicinity of the three-phase contact line (see [7, 26, 82]), and second, the adsorption of nanoparticles on the solid surface resulting in a lower friction at the solid surface. Moreover, the analysis of surface tension data shows independency of nanofluid surface tension on particle concentration.

Disjoining pressure

The quality of the process in many practical applications such as coagulation, lubrication and paper making is related to the stability of thin liquid films containing colloidal particles [82]. Stability of thin films is governed by interactions between surfaces confining them. When a colloidal suspension wets a solid surface, these surface forces result in a so-called disjoining pressure. This pressure stems from the interaction between phases and surfaces at the molecular level within the vicinity of the three-phase contact line. In this region, the suspension changes from a thick fluid film to a microscopic thin film at which surface forces dominate the behavior of the fluid film. The disjoining pressure of a colloidal film can be expressed as combination of three components [86]: molecular (or dispersion) $\prod_m$, electrostatic $\prod_e$, and structural $\prod_s$, as follows:

ATTENTION: The Singapore Copyright Act applies to the use of this document. Nanyang Technological University Library

$$\Pi(H) = \Pi_m(H) + \Pi_e(H) + \Pi_s(H) \tag{2.40}$$

where H is the fluid film thickness. The molecular (van der Waals) and electrostatic components have been studied and well defined in DLVO theory. Despite, the structural component has very recently attracted researchers' attention [82]. Van der Waals and electrostatic effects dominate on very small scales of order in nanometers. However, spreading occurs over larger scales and nanoparticle layering and patterning are observed even at the micron scale level. Thus layering of nanoparticles in the thin fluid film and the resulting structural disjoining pressure dominate over the short-range van der Waals and electrostatic forces [82, 84]. Within this film thickness, nanoparticles are discrete and the resultant pressure is not monotonic [82]. In literature, there are however, few attempts to model the structural disjoining pressure. One approach is to add a hard-core excluded volume contribution to the DLVO theory [107, 108]. This approach, although can capture the oscillatory nature of the structural disjoining pressure, disrupts the simplicity of the DVLO theory. Few empirical expressions are also developed for the structural disjoining pressure by curve-fitting to experimental data [109-111].

Nevertheless, in 2001, Trokhymchuk et al. [82] performed a rigorous analytical study on the structural and depletion components of the disjoining pressure. Employing Laplace transform of the radial distribution function for two large hard spheres (e.g. air bubbles, liquid droplets and nanosized colloidal particles) dispersed in a fluid of smaller hard spheres (e.g. latex particles, micellar colloidal particles and atoms and molecules of the carrier liquid), they derived film thickness and particle concentration dependence of the film interaction energy and film disjoining pressure. The structural and depletion components of the disjoining pressure are of entropic nature and origin from the difference between normal stresses acting on the two sides (inner side = film, and outer side = bulk) of the large spheres. When the film

ATTENTION: The Singapore Copyright Act applies to the use of this document. Nanyang Technological University Library

thickness is so large as tens of diameter of the confined particles in the film, the structural and depletion pressures are negligible. When the film thickness is of the order of a few layers of the confined particles, these pressures start in oscillating manner [112].

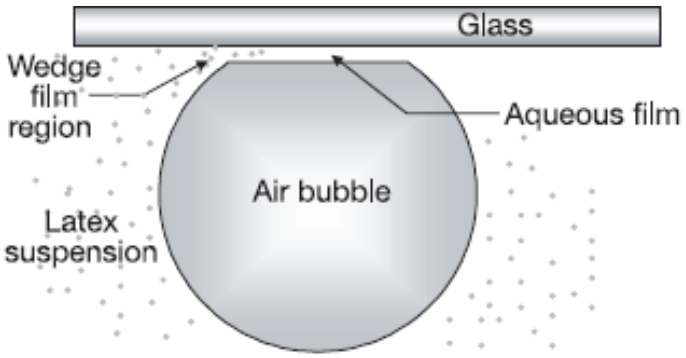

Figure 2-1: Thin film between an air bubble and suspended latex particles (Wasan and Nikolov [26]).

In their analysis, Trokhymchuk et al. divided the fluid film into two regions of thickness $0 < H < d$ and $H \geq d$ where d is the nanoparticle effective diameter. In the first region, since particles cannot enter, there is no track of the structural disjoining pressure; thus, the only affecting component of the disjoining pressure is the depletion force or bulk osmotic pressure P, and the van der Waals and electrostatic forces. In this region, as later developed by Matar et al. [84], the disjoining pressure is as follows:

$$\prod(H) = -P + \frac{A}{6\pi H^3} + 64 n_0 kT \gamma^2 e^{-\lambda H} \tag{2.41}$$

The second term and third term on the right hand side of equation (2.41) are the dispersion (molecular) and electrostatic components of the disjoining pressure respectively. The energy of interaction in this region, however, can be calculated from the following relation:

$$W(H) = \int_H^\infty \prod(h) dh \tag{2.42}$$

ATTENTION: The Singapore Copyright Act applies to the use of this document. Nanyang Technological University Library

In the second region, the film interaction energy and disjoining pressure were developed as follows:

$$W(H) = W_0 \cos(\omega H + \varphi_W) e^{-\kappa H} + W_1 e^{-\delta(H-d)} \tag{2.43}$$

$$\prod(H) = \prod_0 \cos(\omega H + \varphi_\prod) e^{-\kappa H} + \prod_1 e^{-\delta(H-d)} \tag{2.44}$$

In the above equations, functions of the variables are reported in Appendix A.

Wasan and Nikolov [26] (2003) investigated patterning of nanoparticles within the three-phase contact line, and resultant enhancement in spreading. The thin film was produced by blowing an air bubble against a smooth, horizontal hydrophilic solid surface in a monodispersed nanosuspension of 1.01 μm Latex particles in surfactant-free DI water. They found an ordered particle structure in a nearly twice the particle diameter thickness and disordered particle structure in more than three times the particle diameter thickness. Two effects resulted from this ordering. First, higher particle concentration within the film than the concentration inside the bulk fluid and an osmotic pressure develop within the film, which tries to increase the film depth. Second, since the disjoining pressure increases toward the vertex of the film, an additional driving force is created at the film tip [7].

Spreading of nanofluids driven by disjoining pressure

Chengara et al. [83] (2004) performed a parametric study on dynamics of spreading of nanofluids, contact line position and the equilibrium shape of the meniscus by focusing on the effects of particle volume fraction, particle size, and polydispersity. In their work, in addition to the conventional surface free energy, which leads to spreading of a liquid over a solid surface, the role of the structural disjoining pressure was considered; such pressure is significant in providing film energy which adds to the total free energy of the system and thus

ATTENTION: The Singapore Copyright Act applies to the use of this document. Nanyang Technological University Library

enhances spreading. Based on this, two phases were considered in the spreading of an oil drop driven by the disjoining pressure of an aqueous micellar fluid. First, due to imbalance of the three interfacial tension energies, the contact line moves and the contact angle from the aqueous solution side decreases. When the contact angle approaches ~1^{o}, a thin fluid wedge will form at proximity of the three – phase contact line, which confines patterned nanoparticles (see Figure 2-2). This results in the structural disjoining pressure, which finally helps to detach the oil drop from the solid surface. The significance of the structural component of the disjoining pressure as compared to the electrostatic and molecular components was its long-range nature as compared to the short-range nature of DLVO components of the disjoining pressure.

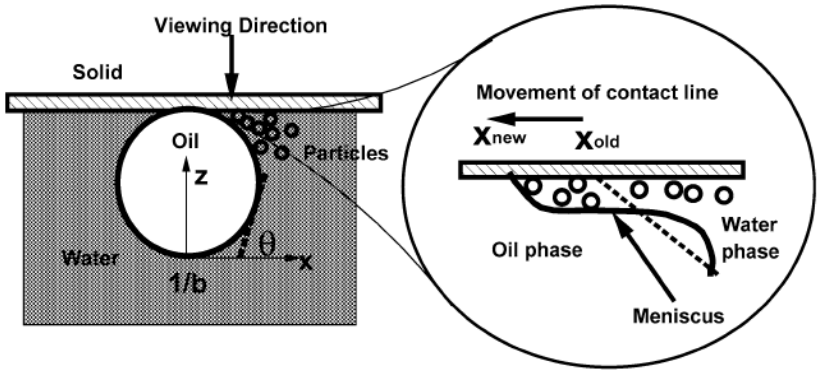

Figure 2-2: Oil drop configuration as in Ref. [83].

Based on the numerical results, Chengara et al. stated that the structural disjoining pressure changes meniscus profile near the wedge as seen in Figure 2-2. Positive structural disjoining pressure results in positive curvature when the profile is viewed from the aqueous side. Conversely, negative structural disjoining pressure results in negative curvature. The effect from the particle volume fraction was found to increase the disjoining pressure, and the higher is the volume concentration the higher is the displacement of the three-phase contact line. For the effect due to particle size on the meniscus profile at a fixed volume fraction, it

ATTENTION: The Singapore Copyright Act applies to the use of this document. Nanyang Technological University Library

was found that there is more shift for particles of smaller size. This is because for the same volume fraction, the smaller the particles, the larger the quantity can rest within the film wedge, and thus the higher is the interaction energy and the disjoining pressure. In case of polydispersity comparing to monodisprsity, it was found that polydispersed particles prevent themselves from ordering within the film thickness thus reducing the film energy and the disjoining pressure.

In 2007, following the previous theoretical efforts to model the physics involved in capillarity of nanofluids [82, 83], Matar et al. [84] studied the dynamics of spreading of nanofluids. They compared the relative importance of the disjoining pressure components by introducing dimensionless parameters that were structural component ($kT/\varepsilon^2\gamma d^2$) ranging from 0.005 to 20.2, van der Waals component ($A/6\pi\varepsilon^2\gamma d^2$) ranging from 0.02 to 66.3 and electrostatic component ($64n_0kT\gamma^2 d/\varepsilon^2\gamma$) ranging from 10^{-25} to 10^{-24}, where $\varepsilon = 0.01$ is the ratio of the characteristic film thickness to the characteristic film length. This indicates that the electrostatic component is relatively insignificant comparing to other components. In addition, for film thickness below one particle diameter, the molecular component of the disjoining pressure is dominating over the depletion component. It was also found that the spreading of nanofluids is accompanied by formation of a step in front of the macroscopic contact line as a result of structural disjoining pressure. The length of this wedge increases with particle volume fraction. However, the rate of spreading will decrease with volume fraction due to increasing viscosity. For the films of thickness less than one particle diameter, van der Waal's component of the disjoining pressure will govern the decay in the film thickness. At intermediate values of the particle concentration, lubrication effect due to attachment of solid particles on the surface will enhance spreading rate [86].

ATTENTION: The Singapore Copyright Act applies to the use of this document. Nanyang Technological University Library

Temperature dependence of nanofluids' surface tension

In 2008, Murshed et al. [113] performed experiments on temperature dependence of surface tension and interfacial tension of nanofluids. Mineral oil with 2% w/w span 80 surfactant was used. DI water-based nanofluids with TiO_2 (15 nm diameter) were also used to form droplets in the mineral oil. They found that surface tension and interfacial tension decrease almost linearly with temperature. This behavior is attributed to the Brownian motion of nanoparticles. Their experiments exhibited less than 8% decrease in surface tension of TiO_2 – DI water nanofluids for temperatures ranging from 25 to 55^{o}C. However, the reduction in interfacial tension of TiO_2 – DI water nanofluids in mineral oil was more pronounced, namely 30%, comparing to DI water – mineral oil interfacial tension.

ATTENTION: The Singapore Copyright Act applies to the use of this document. Nanyang Technological University Library

Chapter 3: Surface tension driven capillary flow in a blind channel

1. Introduction

This chapter presents an investigation into the effects of pneumatic pressure of trapped air on the dynamics of capillary filling. Controlled experiments were carried out in horizontal closed-end capillaries with diameters of 200 to 700 μm. Glycerol-DI water mixture solutions having viscosities ranging from 8 to 80 mPa s were used as the filling liquids. The pneumatic air backpressure is built up as a result of the air compressed at the closed end of the capillary. A model is presented based on the conventional theory of capillary filling (i.e. Washburn's equation [32]) with consideration of the effect of air backpressure force on the advancing meniscus. The molecular kinetics theory of Blake and De Coninck's model [44] is also incorporated in the model to account for the dependence of dynamic contact angle on wetting velocity. The model predictions agree reasonably well with the experimental data. It is observed that due to the presence of air backpressure, the smaller the capillary diameter, the longer the length that the liquid fills the capillary, regardless of the liquid viscosity. It is also shown that the increased pneumatic air backpressure reduces the equilibrium contact angle (θ^0). A relation is then proposed among liquid penetration, capillary length and radius, and contact angle. In addition, a dimensionless analysis is performed on experimental data, and the power law dependence of dimensionless meniscus position on dimensionless time is obtained [114].

ATTENTION: The Singapore Copyright Act applies to the use of this document. Nanyang Technological University Library

2. Materials and methods

General aspects, instrument characteristics, solution preparation, glass ware cleaning and drying

Mixtures of glycerol (Simga-Aldrich) and DI water in various concentrations were used in the experiments. Ratios of 1 part, 2 parts and 4 parts of Glycerol to 1 part of DI water were used in the closed-end capillary flow experiments, while ratios of 4 parts, 6 parts, 8 parts, and 10 parts to 1 part of DI water as well as pure glycerol were used in the experiments of capillary flow from a pendant droplet. Elevated glycerol parts were used in the latter experiments (in which the end of the capillary was unsealed) because the solution is more viscous when more glycerol is concentrated. These glycerol-DI water solutions were found to be of suitable for the experiments as the meniscus moved at a reasonable speed that a normal video camera (CCD camera) coupled with FTA200 software V2.0 in FTA200 instrument could capture. Properties of the glycerol-DI water mixtures such as density, surface tension, viscosity etc were obtained from the Handbook of Chemistry and Physics [115].

The FTA200 instrument uses CCD camera to capture static and dynamic video images for analysis. It is capable of measuring surface tension and static contact angle (thus indirectly, surface energy, adhesion and other surface chemistry quantities) by ‘drop shape’ analysis. Moreover, the instrument is capable of capturing and analyzing multiple frames for liquid spreading or displacement [116] (see Figure 3-1). In the present experiments, FTA200 instrument was mainly utilized for its ability to capture dynamic video images in multiple frames. The video could then be analyzed frame by frame to accurately measure liquid displacements. Time interval could vary from 0.017s (60 images per second) to 500s. In addition, the number of images could be as many as 3000 shots. The camera was adjusted in

ATTENTION: The Singapore Copyright Act applies to the use of this document. Nanyang Technological University Library

height by a stage, and a pinion and rack assembly was used to move it sideways in the process of capturing meniscus successive positions.

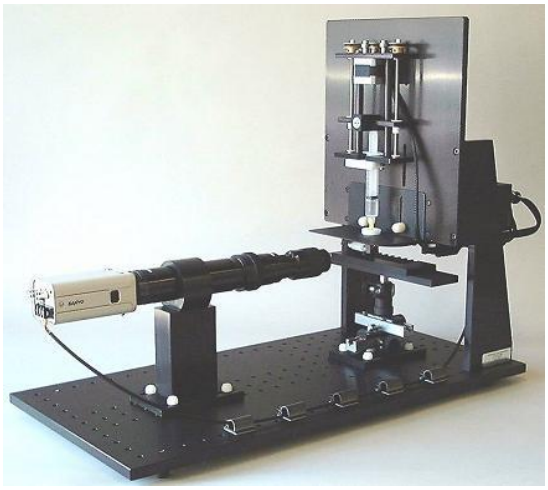

Figure 3-1: FTA200 instrument consisting of a high resolution camera, a zoom microscope, PCI frame grabber card, computer-controlled syringe pump, computer-controlled lighting and an adjustable specimen.

For the purpose of reading and analysis of meniscus displacement, MB-Ruler software was used. This software allows user to set a reference line on a known distance in the image (i.e. calibration), and then to measure the actual distance between any two points (see Figure 3-2).

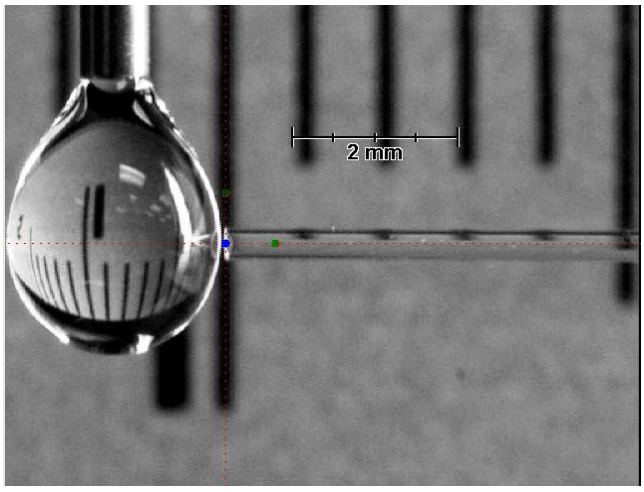

Figure 3-2: On screen MB-Ruler with reference line calibtaed with the real ruler at the back of the capillary tube.

Aqueous glycerol solutions were prepared and mixed using an ultrasonic mixer to achieve a better mixing and stored in pre-cleaned glass containers to prevent any possible

ATTENTION: The Singapore Copyright Act applies to the use of this document. Nanyang Technological University Library

contamination. Borosilicate glass capillaries with diameters varying 200 to 700 μm were purchased from VitroCom, Inc (New Jersey, USA). These capillaries as well as all glassware used in the preparation of the glycerol-DI water mixtures were washed thoroughly with detergent, HCL, and NaOH, followed by rinsing with DI water. The successive steps of cleaning process are as follows (the cleaning process is similar to that of refs. [41, 71]):

1. Glass ware and needles were first cleaned with tapped water and detergent. They were then soaked in a more polar solvent, acetone, for 10 minutes; followed by several times rinsing with DI water. For capillary tubes, syringes were used to flush the DI water within the capillary.

2. Next, 1 N Sodium Hydroxide solution (Simga-Aldrich) was used to soak glass wares for another 10 minutes. Afterwards, they were flushed vigorously with DI water.

3. They were then soaked in 1 N Hydrochloric Acid solution (Simga-Aldrich) for 10 minutes, followed by final rinsing with DI water for several times in order to prevent any residue from base and acid.

Nevertheless, the drying process of the capillaries showed some difficulties. At this spot, four different techniques were applied:

1. Using hair dryer (which was successful for 700 μm capillary),
2. Blowing with dehumidified air for more than 8 hours,
3. Heating in air circulated oven at 200^{o}C for several hours,
4. Blowing with air gun.

Two problems were encountered in our experiments: one is the liquid coating on the outer capillary surface; and the other is the jagged motion of liquid meniscus especially when approaching to the asymptotic displacement. The first problem is associated with the

ATTENTION: The Singapore Copyright Act applies to the use of this document. Nanyang Technological University Library

hydrophilic nature of glass capillaries. During experiments, we found that when liquids were in contact with a capillary tube, liquid menisci were formed on both the interior and outer capillary surfaces, resulting in an effect on the flow at the capillary entrance [72, 117]. This problem was overcome by applying a layer of wax to the outer surface of the capillary to make the surface hydrophobic [118]. The second problem is attributed to the DI water residue in the capillaries (see Figure 3-3) because it was used to flush the capillaries prior to experiment. To remove these water spots, two drying techniques were tried by: (i) using a hair drier, and (ii) heating in air circulated oven at 200^{o}C. However, some water residues were remained inside small capillaries. The presence of these small water residues caused jerky behavior of meniscus movement (due to local changes in surface wetting properties), and resulted in inconsistent records. Although this problem was less severe for 500 µm capillaries and did not exist for 700 µm capillaries, to maintain the same surface conditions in all of our experiments, we found that it was more accurate to use dry capillaries directly from the sealed vial without any washing. For each experimental condition, three parallel measurements were conducted, and an average was taken to represent the experimental data.

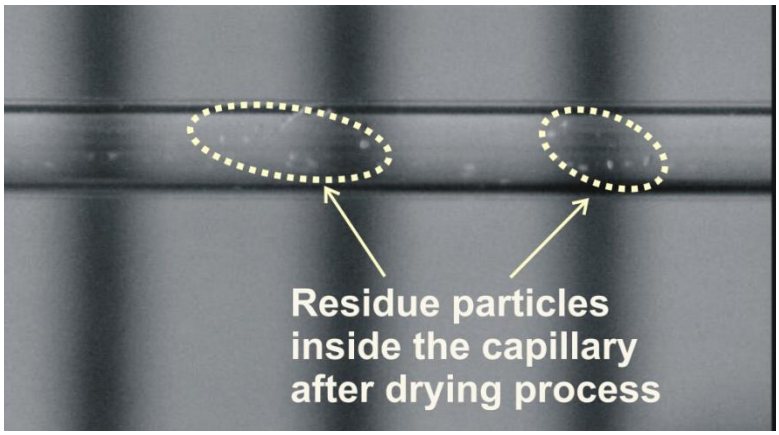

Figure 3-3: Residue particles remained inside the 500 µm capillary after drying process.

The general precautions to be taken during the experiments were as follows:

ATTENTION: The Singapore Copyright Act applies to the use of this document. Nanyang Technological University Library

1. In order to prevent hydrostatic pressure (gravity effects), it was important to align the capillary tubes horizontally. For this, a holder with three supporters was used, and the capillaries were placed in contact with all the three contact points on the holder.
2. Any vibration should also be kept to a minimal so that the flow would not be affected. This was more serious for the case of capillary flow from a pendant droplet, because vibration caused the droplet to collapse.
3. The camera should be firmly secured to its translating stage so as not to produce any elusion error due to tilting.

Moreover, there were some intrinsic errors in the experiments which should have been minimized:

1. Errors in preparation of the test liquids. An exact concentration was rare to be obtained, because when adding one pure liquid to other pure liquid, small amount of each would remain inside preparing containers.
2. Contamination of test liquids could cause changes in surface tension and viscosity. In addition, impurities inside the capillary tubes (e.g. the tiny liquid particles inside the capillary as shown in Figure 3-3) caused unrealistic experimental results.
3. The adjustment of MB-Ruler to the real ruler behind the capillary was a source of eye elusion in displacement readings.

Experimental investigation on surface tension driven capillary flow in a blind channel

A beaker with an inlet arm (see Figure 3-4) was filled with the displacing liquid whose level in the beaker was maintained the same as the capillary centerline to ensure that the flow was solely driven by surface tension and not by gravity-induced hydrostatic effect.

ATTENTION: The Singapore Copyright Act applies to the use of this document. Nanyang Technological University Library

Using the translating stages, the beaker was brought close to the capillary entrance. Once the convex liquid face touched the capillary tube, surface tension would cause the liquid to flow through the capillary. The camera which was mounted on a translating stage would follow the liquid meniscus and capture its spontaneous positions frame by frame. The recording would only be stopped after the liquid came to rest completely.

The main feature of the experiment is to seal the capillary exit with silicon glue to assume a closed-end tube. The sealing should prevent any possible leakage of air from the capillary [114].

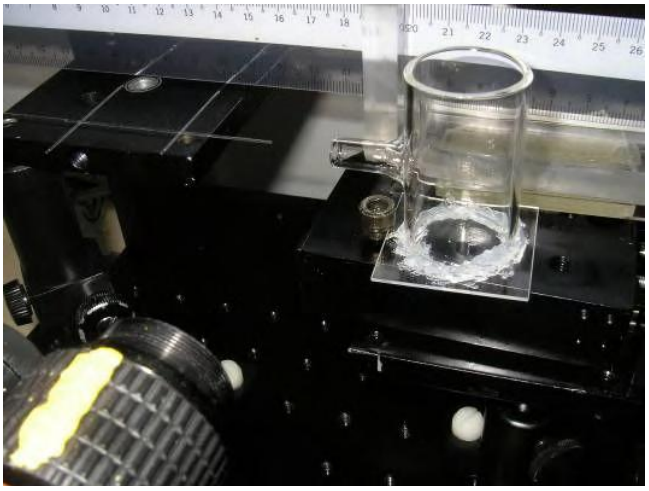

Figure 3-4: Beaker with inlet arm, ruler, and capillary tube and CCD camera (from ref. [119]).

At this spot, capillaries with diameter ranging 300 to 700 μm having the same length equal to 10 cm were used. Aqueous glycerol solutions with concentration ranging 50% to 80% were also used. It was found that the smaller was the diameter of a capillary the longer was the total meniscus displacement. Nevertheless, the total displacements in all the experiments were less than 1 mm (maximum ~ 0.7 mm for 300 μm). This justifies that the presence of air back pressure causes strong hindrance in meniscus movement, because otherwise, if the end of the capillary was open, the liquid would travel the total length of the capillary. As a result, in order to investigate meniscus dynamics in longer travels inside the capillary, a new batch

ATTENTION: The Singapore Copyright Act applies to the use of this document. Nanyang Technological University Library

of experiment were performed with 200 µm capillary and attachment of a syringe, thus providing more volume of air to be compressed at the back. The equivalent length of the capillary should then be calculated dividing the total volume of the syringe and capillary by the cross section area of the capillary. It was important that no air could escape out of the syringe or the part where the capillary was attached to the needle (see Figure 3-5). For this design, it was found that the meniscus could travel the total length of the capillary.

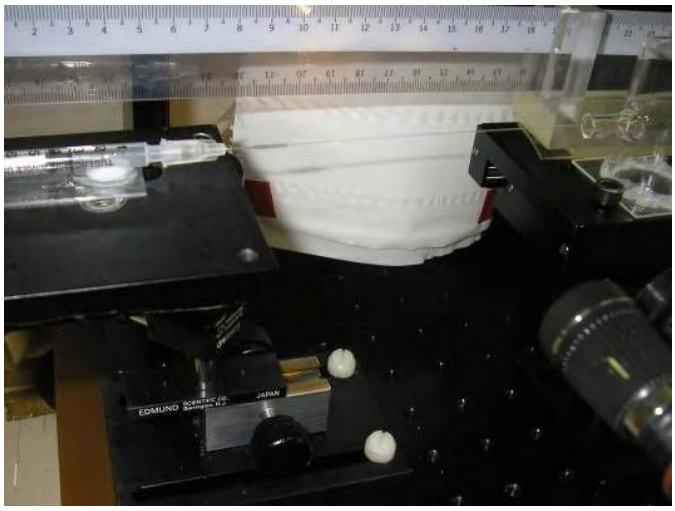

Figure 3-5: Attachment of syringe to the back of the capillary to stimulate longer capillary (from ref. [119]).

Experimental data of these experiments are first published in [119, 120].

3. Theoretical investigation

The complete form of the Navier-Stokes momentum conservation formulation (including the surface tension stress) of an incompressible Newtonian liquid is as follows:

$$\rho\left(\frac{\partial u}{\partial t}+u.\nabla u\right)=-\nabla p+\eta\nabla^2 u+\gamma\kappa\delta_s\hat{n}\,, \tag{3.1}$$

ATTENTION: The Singapore Copyright Act applies to the use of this document. Nanyang Technological University Library

where κ $(=\nabla_s.\hat{n})$ [m^{-1}] is the interface radius of curvature, δ_s [m^{-1}] is the Dirac delta function centered on the interface and $\hat{n}$ is the unit normal to the interface. Here, applying the Dirac delta function, surface tension is transformed into a volumic force, [121].

Inserting the following nondimensional groups:

$$\tilde{u}=\frac{u}{U} \quad \tilde{x}=\frac{x}{D} \quad \tilde{t}=\frac{t}{\rho D^2/\eta} \quad \tilde{p}=\frac{p}{\eta U/D} \quad \tilde{\gamma}=\frac{\gamma}{\eta U} \quad \tilde{\kappa}=D\times\kappa \quad \tilde{\delta}=D\times\delta,$$

in equation(3.1), where U is the mean velocity of the flow and D is the tube diameter, this equation simplifies to a more comprehensible nondimensional form:

$$\frac{\partial\tilde{u}}{\partial\tilde{t}}+\mathrm{Re}\left(\tilde{u}.\tilde{\nabla}\tilde{u}\right)=-\tilde{\nabla}\tilde{p}+\tilde{\nabla}^2\tilde{u}+\tilde{\gamma}\tilde{\kappa}\tilde{\delta}_s\hat{n}, \tag{3.2}$$

where $\tilde{\nabla}=D\times\nabla$.

According to equation (3.2), the main forces that act on liquid column moving in horizontal capillary tube with air enclosed at the back (see Figure 3-6) are: surface tension force (F_{ST}), air back pressure resistance (F_{AB}), and viscous drag (F_V), which are balanced by inertia effects. From Figure 3-6, it is obvious that the test liquid level in the beaker is set to the tube centerline in order to avoid hydrostatic pressure.

ATTENTION: The Singapore Copyright Act applies to the use of this document. Nanyang Technological University Library

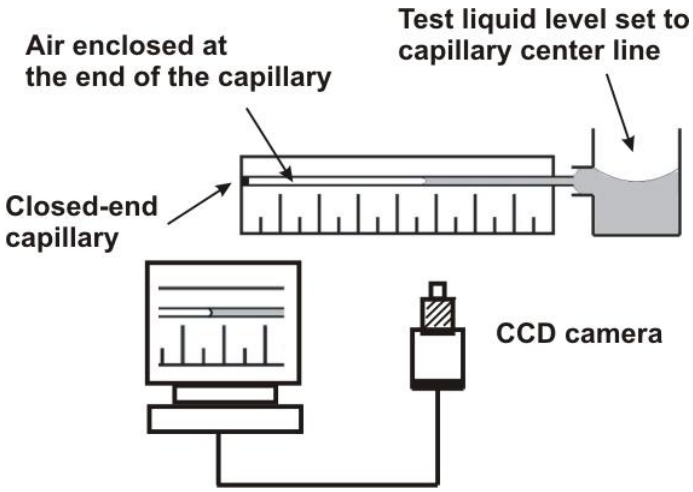

Figure 3-6: Schematic of closed-end capillary flow

Referring to Washburn's assumptions (equation (2.5)), the inertia effects ($\partial\tilde{u}/\partial\tilde{t} + \mathrm{Re}\left(\tilde{u}.\tilde{\nabla}\tilde{u}\right)$) are only significant at initial stages of fluid rise and may have further importance for capillaries of large radius. This statement was scrutinized in later experimental and theoretical studies [33, 37, 41, 42, 52, 58, 61, 62, 69], and found to be reasonable for the duration of real experiments. However, it was shown that the importance of inertia effects at initial stages of capillary flow is more pronounced for liquids of very low viscosity, e.g. water and ethanol, [68, 71]. Ichikawa and Satoda [122], Quere [70], Hamraoui and Nylander [43] and Stange [72] stated that the transition time from inertia stress dominancy ($\partial\tilde{u}/\partial\tilde{t} + \mathrm{Re}\left(\tilde{u}.\tilde{\nabla}\tilde{u}\right)$) to viscous stress dominancy ($\tilde{\nabla}^2\tilde{u}$) is equal to $\tau_1 = \rho r^2/4\eta$. This time scale which gives a characteristic time of transition to fully developed flow (i.e. the time necessary for viscous boundary layer to diffuse on a length of order the radius of the tube) can be obtained by equating characteristic inertia force to characteristic viscose force:

$$\left.\begin{array}{ll} \text{inertia force} & \pi r^2 \rho \dfrac{d\left(x\dot{x}\right)}{dt} \rightarrow 2\pi r^2 \rho \dfrac{D^2}{\tau^2} \\ \text{viscous force} & 8\pi\eta x\dot{x} \rightarrow 8\pi\eta \dfrac{D^2}{\tau} \end{array}\right\} \xrightarrow{2\pi r^2 \rho D^2/\tau^2 = 8\pi\eta D^2/\tau} \tau = \frac{\rho r^2}{4\eta}$$

ATTENTION: The Singapore Copyright Act applies to the use of this document. Nanyang Technological University Library

It is noted that the viscous force in the above equation is written for a laminar flow. As will be discussed later, for very low Reynolds number capillary-driven flows, this assumption is completely reasonable.

For the range of the capillary radii as well as liquid viscosities used in the present project, the modesty of inertia term in equation (3.2) comparing to viscous force and surface tension force is justified in Table 3-1. According to Table 3-1, the maximum Reynolds number in our experiments ($\rho U_{max} D/\eta$) is far less than the transition Reynolds to turbulence. This very low Reynolds number is due to the existence of an air back pressure in front of the moving meniscus, which resists meniscus motion and reduces its velocity, resulting in meniscus inertia effects to be negligible comparing to viscous effects. Moreover, the ratio of inertia force to surface tension force (Weber number $\rho U_{max}^2 D/\gamma$) is also very small. This supplementary evidence supports that the inertia force is also insignificant comparing to surface tension force. Further evidence is the transition time of inertia dominant flow to viscous dominant flow. Here, it is obvious that this time scale is completely negligible comparing to the duration of our experiments (> 1 s).

Table 3-1: Reynolds (Re), Weber (We), and capillary (Ca) numbers and viscous transition time (τ) for typical water, ethnol, the lowest and highest viscous liquids used in the experiments, and pure glycerol, U_{max}=1 cm.s^{-1}.

Liquid concentration	Radius $[\mu m]$	Re_{max} $(\rho U_{max} D/\eta)$	We_{max} $(\rho U_{max}^2 D/\gamma)$	$\tau = \rho r^2/4\eta$ $[ms]$
water	350	7	9.72×10^{-4}	30
ethanol	350	4	2.51×10^{-3}	20
1:1 Glycerol/water	150	< 1	5.11×10^{-4}	< 1
1:1 Glycerol/water	350	< 1	1.19×10^{-3}	4
4:1 Glycerol/water	150	~ 0.1	5.54×10^{-4}	< 0.1

ATTENTION: The Singapore Copyright Act applies to the use of this document. Nanyang Technological University Library

4:1 Glycerol/water	350	< 0.1	1.29×10^{-3}	< 1
Glycerol	350	~ 0.01	1.41×10^{-3}	< 0.1

Considering the above discussions, equation (3.2) simplifies to the following equation:

$$\underbrace{\frac{\partial \tilde{u}}{\partial \tilde{t}}}_{\sim 0} + \underbrace{\mathrm{Re}\left(\tilde{u}.\tilde{\nabla}\tilde{u}\right)}_{\sim 0} = -\tilde{\nabla}\tilde{p} + \tilde{\nabla}^2\tilde{u} + \tilde{\gamma}\tilde{\kappa}\tilde{\delta}_s\hat{n}\,,$$

$$\tilde{\gamma}\tilde{\kappa}\tilde{\delta}_s\hat{n} = \tilde{\nabla}\tilde{p} - \tilde{\nabla}^2\tilde{u}$$

and as a result, back to the dimensional form, it follows that:

$$\gamma\kappa\delta_s\hat{n} = \nabla p - \eta\nabla^2 u \tag{3.3}$$

Generally, using Laplace equation(2.1), the surface tension stress ($\gamma\kappa$) in equation (3.3) is included in the ∇p term (i.e. $\nabla p_c = \left(2\gamma r/\cos\theta\right)/x$ in which $2r/\cos\theta$ is the radius of curvature of the hemispherical meniscus cap, and the subscript *c* denotes the capillary pressure). This approach simplifies equation (3.3) in the way that a static contact angle assumption during the meniscus motion will lead to a constant pressure gradient along the liquid column. As a result of a constant pressure gradient, theoretically, application of Poiseuille's velocity profile for the viscous laminar flow inside the capillary tube is confirmed. However, plenty of experimental studies certified the existence of Poiseuille's velocity profile even in the case of a dynamic behavior in contact angle [37, 41, 43, 45, 58, 61, 62, 68-72, 122]. This is because the surface tension force (as a surface force) is located just at the liquid-air interface, and it is not a real bulk force (pay attention to the use of Dirac delta function (δ_s) in equation(3.3)). In this project, similar to previous investigations and considering the very low Reynolds number as well as very small transition time to fully

ATTENTION: The Singapore Copyright Act applies to the use of this document. Nanyang Technological University Library

developed laminar flow, it is assumed that the quadratic velocity profile of Poiseuille ($u/U = 2(1-a^2/r^2)$, $0 < a < r$) exists in the liquid column. As a result of this velocity profile, the viscous drag force can be obtained as follows:

$$F_{\mathrm{V}} = 8\pi\eta x\dot{x} \tag{3.4}$$

The difference between air back pressure (p_a) and ambient pressure (p_{atm}) at the two ends of the liquid column, causes additional resistance to the flow. The resisting force due to this pressure difference is as follows:

$$F_{\mathrm{AB}} = \left[p_{\mathrm{air}} - p_{\mathrm{atm}}\right]\pi r^2 \tag{3.5}$$

The driving force is the surface tension force (F_{ST}) due to the meniscus curvature according to Laplace equation (2.1). This force is a function of contact angle and radius of curvature and is balance by F_{V} and F_{AB}. In small cylindrical tubes the meniscus curve does not depart from a spherical shape. This statement is more justified for the small Weber and capillary numbers in our experiment (see Table 3-2). As stated before, the Weber number indicates the relative magnitudes of inertial and surface tension forces, and capillary number those of viscous and surface tension forces. Small values of these two dimensionless groups designate that inertia and viscous effects do not have any influence on the meniscus curvature; and as a result meniscus cap will retain its spherical curve [7]. Hence, the radius of curvature for the hemispherical meniscus in the capillary tube is $\kappa = \left(1/R_1 + 1/R_2\right) = 2\cos\theta/r$.

ATTENTION: The Singapore Copyright Act applies to the use of this document. Nanyang Technological University Library

Table 3-2: We and Ca numbers for liquid concentrations used in the experiments, the capillary radius is 350 μm.

Liquid concentration	We_{max} $\left(\rho U_{max}^2 D/\gamma\right)$	Ca_{max} $\left(\eta U_{max}/\gamma\right)$
1:1 glycerol/water	1.19×10^{-3}	1.25×10^{-3}
2:1 glycerol/water	1.24×10^{-3}	4.12×10^{-3}
4:1 glycerol/water	1.29×10^{-3}	1.21×10^{-2}

As stated before, regarding the capillary pressure relation as the pressure drop across the interface ($\Delta p_c = \gamma\left(1/R_1 + 1/R_2\right)$, Laplace equation (2.1)), the surface tension stress (left hand side of equation(3.3)) is usually included in the ∇p term such as $\nabla p_c = \gamma\kappa\delta_s\hat{n}$, where the subscript *c* denotes the capillary pressure. Hence [123]:

$$\nabla p_c = \frac{\left(\frac{2\gamma\cos\theta}{r}\right)}{x}$$

and the resulting surface tension force is equal to:

$$F_{ST} = 2\pi r\gamma\cos\theta \tag{3.6}$$

Balancing the viscous drag, air back pressure resistance and surface tension force in equations (3.4), (3.5) and (3.6) respectively, the final equation of capillary motion can be obtained as follows (see Figure 3-7):

$$2\pi r\gamma\cos\theta = \left[p_{air} - p_{atm}\right]\pi r^2 + 8\pi\eta x\dot{x} \tag{3.7}$$

ATTENTION: The Singapore Copyright Act applies to the use of this document. Nanyang Technological University Library

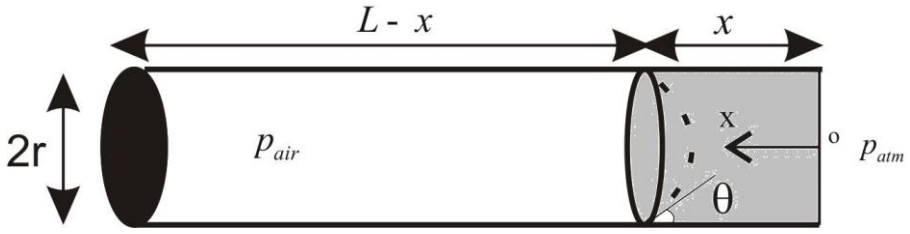

Figure 3-7: Schematic of surface tension driven flow in a closed-end capillary.

When one end of an empty capillary tube is introduced to a liquid reservoir, the resulting unbalanced surface tension force causes the liquid to move in subsequently at a rate established by the magnitude of the surface tension force. Here, with refer to equation (3.7) the main variable parameters of the dynamics of capillary filling are the contact angle θ and the liquid column length x.

Dynamic contact angle

It has been previously shown that the local contact angle between the liquid meniscus and the capillary surface becomes dynamic ($\theta = \theta_d$) when the liquid front is in movement (see Figure 3-8). Several attempts have been made in literature to interpret this dynamic behavior of the local contact angle [36, 39, 55, 57, 59, 65]. These various models deem the driving out-of-balance surface tension force is balanced by various energy dissipation modes, thus differ in their respective conceptual framework and identification of the effective channel of energy dissipation. Roughly, most of the models may be classified as emphasizing hydrodynamic or molecular kinetic aspects [33]. In the hydrodynamic approach dissipation is due to viscous effects within the liquid and thus the role of solid-liquid molecular interactions are discounted, whereas in the molecular kinetic approach the properties of the solid-liquid molecular interactions are accommodated [33]. Nevertheless, the molecular kinetic theory (MKT) is the only available theoretical model that provides comparatively good predictions for experimental results and has physically reasonable values of its characteristic parameters

ATTENTION: The Singapore Copyright Act applies to the use of this document. Nanyang Technological University Library

[33, 63, 64, 66, 67]. Simply, MKT states that this dynamic behavior in contact angle (or meniscus shape) is due to frictional dissipation at the moving wetting front (the immediate vicinity of the moving contact line) in the process of attachment or detachment of fluid molecules to or from the solid surface. In fact the wetting front advances the solid substrate molecular layer by molecular layer and the dynamics of wetting significantly depends on the coefficient of friction of this film on the solid surface.

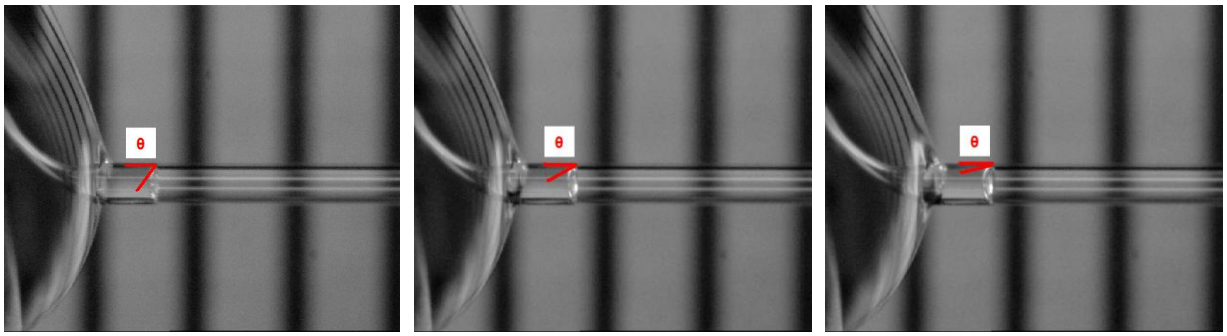

Figure 3-8: Variation of contact angle during capillary penetration. Capillary diameter is 300 µm. The distance between ruler lines behind the capillary tube is 1 mm.

According to MKT, the equation of wetting line velocity is:

$$\dot{x} = 2K_W^0 \lambda \sinh\left[\left(\frac{\gamma}{2nk_BT}\right).\left(\cos\theta_\infty - \cos\theta_d\right)\right], \tag{3.8}$$

in which the dynamic contact angle (θ_d) is conceptualized as a function of contact line velocity with effects from the distance between adsorption sites on the solid surface (λ), and the equilibrium frequency of displacement of a molecule between two adjacent adsorption sites occurring within the three-phase zone $\left(K_W^0\right)$. According to the definition of motion in MKT [39], the molecular displacement from one site in the three phase zone to the other site is introduced on the basis of the theory of absolute reaction rates. The frequency of this displacement in positive and negative directions is:

ATTENTION: The Singapore Copyright Act applies to the use of this document. Nanyang Technological University Library

$$K^{\pm} = \left(\frac{k_B T}{h}\right) \exp\left(\frac{-\Delta g_W^*}{n k_B T}\right)$$

where Δg_W^* is the specific activation free energy of wetting process (or the specific energy barrier). At equilibrium, the two frequencies of displacement are equal to each other ($K^+ = K^- = K_W^0$), and:

$$K_W^0 = \left(\frac{k_B T}{h}\right) \exp\left(\frac{-\Delta g_W^*}{n k_B T}\right) \tag{3.9}$$

When the contact line is in forward motion, the irreversible work at the solid-liquid interface due to the unbalanced surface tension force (per unit displacement of unit length of the contact line), i.e. $\gamma\left(\cos\theta_\infty - \cos\theta_d\right)$, lowers the energy barriers in forward (superscript +) and raises the energy barriers in backward (superscript -) directions, and results in net movement in forward direction with the net frequency:

$$K_{\text{net}} = \left(\frac{k_B T}{h}\right)\left[\exp\left(\frac{\frac{\gamma\left(\cos\theta_\infty - \cos\theta_d\right)}{2} - \Delta g_W^*}{n k_B T}\right) - \exp\left(\frac{\frac{-\gamma\left(\cos\theta_\infty - \cos\theta_d\right)}{2} - \Delta g_W^*}{n k_B T}\right)\right]$$

$$\Rightarrow K_{\text{net}} = K_W^0\left[\exp\left(\frac{\gamma\left(\cos\theta_\infty - \cos\theta_d\right)}{2 n k_B T}\right) - \exp\left(\frac{-\gamma\left(\cos\theta_\infty - \cos\theta_d\right)}{2 n k_B T}\right)\right]$$

$$\Rightarrow K_{\text{net}} = 2K_W^0 \sinh\left(\frac{\gamma\left(\cos\theta_\infty - \cos\theta_d\right)}{2 n k_B T}\right)$$

Finally the velocity of the three phase contact line is $u = K_{\text{net}}\lambda$, see equation (3.8).

Here, n is the number of adsorption sites per unit area of the solid surface, and thus for a uniformly distributed sites, $n = \lambda^{-2}$ (see Figure 3-9).

ATTENTION: The Singapore Copyright Act applies to the use of this document. Nanyang Technological University Library

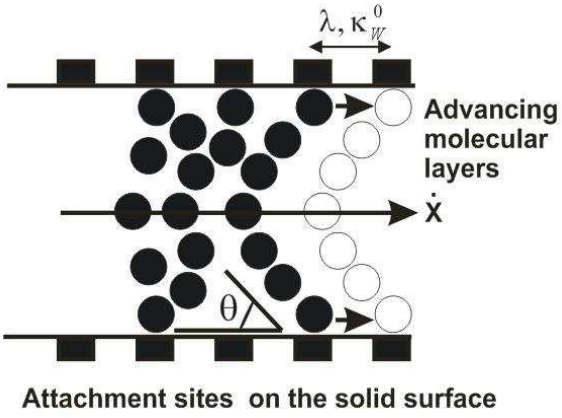

Figure 3-9: Schematic of MKT characteristic parameters.

When θ_d is close to θ_∞, for which $\gamma(\cos\theta_\infty - \cos\theta_d) << 2k_BT/\lambda^2$, equation (3.8) simplifies to a linear from:

$$\dot{x} = K_W^0 \gamma \frac{(\cos\theta_\infty - \cos\theta_d)\lambda^3}{k_B T} \tag{3.10}$$

At this point, it is possible to define a coefficient of wetting line friction, ζ, (with the same units as the bulk dynamic viscosity $[Pa.s]$):

$$\zeta = \frac{k_B T}{K_W^0 \lambda^3} \tag{3.11}$$

Combining equations (3.10) and (3.11), the explicit form of wetting line energy dissipation due to this fictitious friction is obtained:

$$\gamma(\cos\theta_\infty - \cos\theta_d) = \zeta \dot{x} \tag{3.12}$$

Following this equation and as discussed earlier, it is obvious that $\gamma(\cos\theta_\infty - \cos\theta_d)$ is the driving force and $\zeta\dot{x}$ is the frictional drag at the three phase contact line.

ATTENTION: The Singapore Copyright Act applies to the use of this document. Nanyang Technological University Library

Further, Blake and De Coninck [44] assumed that the activation free energy of wetting have two contributions due to molecular surface interaction (solid-liquid) and molecular viscous interactions (liquid-liquid):

$$\Delta g_W^* = \Delta g_S^* + \Delta g_V^* \tag{3.13}$$

This equation is justified by the fact that the molecules within the three phase zone are hindered by both of the interactions. Then on the basis of absolute reaction rates theory, Blake and De Coninck introduced the following frequency for the surface interaction (see equation (3.9)):

$$K_S^0 = \frac{k_B T}{h} \exp\left(\frac{-\Delta g_s^*}{n k_B T}\right) \tag{3.14}$$

According to Eyring theory [124] (which relays the molecular viscous interactions within a liquid to rated reactions), viscosity of the liquid is related to Δg_V^* as follows:

$$\eta = \frac{h}{\upsilon} \exp\left(\frac{\Delta g_V^*}{n k_B T}\right) \tag{3.15}$$

where υ is the volume of the unit of flow (for liquids it is equal to molecular volume). Combining equations (3.8), (3.9), (3.13) and (3.15), Blake and De Coninck rewrite the equation of contact line velocity as follows:

$$\dot{x} = \frac{2K_S^0 h\lambda}{\eta\upsilon} \sinh\left[\frac{\gamma}{2nk_B T}\left(\cos\theta_\infty - \cos\theta_d\right)\right] \tag{3.16}$$

This equation has the advantage that the different interactions due to viscosity and surface effects are isolated.

ATTENTION: The Singapore Copyright Act applies to the use of this document. Nanyang Technological University Library

As discussed earlier, Δg_S^* is the surface contribution in the activation free energy of wetting process per unit area (i.e. the energy barrier in successive adsorption and desorption of liquid molecules on solid surface). According to this definition, Blake and De Coninck applied a qualitative 1:1 relationship between the reversible work of adhesion ($W_a^0 = \gamma\left(1+\cos\theta_\infty\right)$) and Δg_S^*, i.e. $\Delta g_S^* = W_a^0$:

$$\Delta g_S^* = \gamma\left(1+\cos\theta_\infty\right) \tag{3.17}$$

and consequently (see equation (3.14)):

$$K_S^0 = \frac{k_B T}{h}\exp\left(\frac{-\gamma\left(1+\cos\theta_\infty\right)}{nk_B T}\right) \tag{3.18}$$

Combining equations (3.16) and (3.18), the modified equation of contact line motion can be obtained as follows:

$$\dot{x} = \frac{2k_B T\lambda}{\eta\upsilon}\exp\left(\frac{-\gamma\left(1+\cos\theta_\infty\right)}{nk_B T}\right)\sinh\left[\frac{\gamma}{2nk_B T}\left(\cos\theta_\infty - \cos\theta_d\right)\right] \tag{3.19}$$

and for small argument of $\sinh$ (as used in equation (3.8) to (3.10)), this equation simplifies to:

$$\dot{x} = \frac{\lambda}{n\eta\upsilon}\exp\left(\frac{-\gamma\left(1+\cos\theta_\infty\right)}{nk_B T}\right)\gamma\left(\cos\theta_\infty - \cos\theta_d\right) \tag{3.20}$$

Despite the very effective and simple description of the wetting process, and good predictions of experimental results, MKT has some limitations:

1. There is no definitive way of calculating the characteristic parameters of MKT as they are completely notional [40] and values of λ, n, K_W^0, and ζ for a given solid-liquid

ATTENTION: The Singapore Copyright Act applies to the use of this document. Nanyang Technological University Library

system should be treated as adjustable parameters and obtained from experiments by curve-fitting procedures.

2. The assumption of a uniform distribution of adsorption sites, i.e. $\lambda = 1/\sqrt{n}$.
3. Applying a 1:1 relation between the surface contribution of activation free energy of wetting and reversible work of adhesion, although rational in definition, is rather notional. However, recent investigations have justified this approximation [47-51].
4. Negligence of other additional channels of energy dissipation such as substrate deformation [44] or more possible and sensible hydrodynamic effects at the wedge of the meniscus. As discussed earlier, hydrodynamic approaches, which only consider the dissipation due to hydrodynamic effects and ignore the effects on molecular scale, show abatement in describing experimental results, and predict very small values of their characteristic length (slip length L_s) in ranges below molecular diameter in the curve-fitting procedure. Although, combined hydrodynamic/molecular approaches are developed which can accommodate the slip length problem [65], but the resulting equilibrium frequency is unreasonably very small. Definitely, MKT is the only available theoretical model that provides comparatively good predictions for experimental results and has physically reasonable values of its characteristic parameters. As stated before, in the present project, MKT is also used.
5. For a mixture of different liquids, like glycerol + water in this project, the values of υ is equal to the molecular volume of the liquid which is dominant at the solid surface and is not known a priori.

Considering what have stated in the fifth remark, while the value of λ depends on the spacing of adsorption sites on the solid surface, it is influenced by the size of liquid molecules adjacent to the solid surface too [40]; thus a first insight gives the approximation $\lambda^3 \cong \upsilon$. This is justified for the values of λ being almost between molecular diameter of

ATTENTION: The Singapore Copyright Act applies to the use of this document. Nanyang Technological University Library

glycerol (~ 0.6 nm) and water (~ 0.38 nm) [125] (see tables 4 and 5). This approximation results in a simpler form of equation (3.20):

$$\dot{x} = \frac{\gamma\left(\cos\theta_{\infty} - \cos\theta_{d}\right)}{\eta} \exp\left(\frac{-\gamma\lambda^{2}\left(1+\cos\theta_{\infty}\right)}{k_{B}T}\right) \tag{3.21}$$

Comparing this equation with equation (3.10) and (3.11) gives the following simple relation for ratio of the coefficient of friction at the contact line to the bulk viscosity:

$$\frac{\zeta}{\eta} = \exp\left(\frac{\gamma\lambda^{2}\left(1+\cos\theta_{\infty}\right)}{k_{B}T}\right) \tag{3.22}$$

In this project, ζ will be found as an adjustable parameter by curve-fitting to experimental results. Then, λ will be calculated from equation (3.22). Finally, K_{W}^{0} will be determined from equation (3.11).

Air backpressure

As air is confined by the closed-end of the capillary, it is compressed by the liquid column advancing in the capillary, resulting in a higher air pressure than the ambient pressure. This pressure difference at two ends of the liquid column exerts a net drag force ($=\left[P_{\text{air}} - P_{\text{atm}}\right]\pi r^{2}$) on the meniscus. Applying invariant product of pressure and volume (i.e., the ideal gas relation), this pressure difference can also be expressed as:

$$\left[P_{\text{air}} - P_{\text{atm}}\right] = P_{\text{atm}}\left(\frac{x}{L-x}\right). \tag{3.23}$$

Finally, replacing the contact angle θ by the dynamic contact angle θ_{d} in equation (3.7) and inserting equation (3.12) and equation (3.23), equation (3.7) which describes surface tension driven flow in a closed-end capillary can be rewritten as:

ATTENTION: The Singapore Copyright Act applies to the use of this document. Nanyang Technological University Library

$$2\pi r\gamma\left(\cos\theta^0-\frac{\zeta\dot{x}}{\gamma}\right)=8\pi\eta x\dot{x}+P_{\text{atm}}\left(\frac{x}{L-x}\right)\pi r^2. \tag{3.24}$$

Equation (3.24) cannot be solved analytically, and direct numerical integration should be used to compute the meniscus position (x).

Our experiments showed that the penetration length was always much smaller (in order of one hundredth) than the capillary length, i.e. $x/l \approx 0.01$. This small ratio is also applicable to the cases where a syringe was attached to the end of the capillary (see Sec. Results and Discussion). Thus, it is possible to rewrite equation (3.23) in a linear form as follows:

$$P_{\text{atm}}\left(\frac{x}{L-x}\right)\cong P_{\text{atm}}\left(\frac{x}{L}\right). \tag{3.25}$$

This is however in analogy to open-end vertical capillary flow with the gravity term (ρgH) being a linear function of capillary penetration height (H).

During the capillary flow, surface tension force is balanced by inertia, viscous drag, and air backpressure forces. However, since in surface tension driven capillary flows the Reynolds number and Weber number are very low (i.e., Re < 1 and We << 1), it is a reasonable assumption to neglect inertia effects. In addition, in our experiments, it was found that velocity of penetration decreases rapidly and length of penetration is very small; thus, viscous drag force is also very small and can be ignored. As a result, it is possible to write the equation of meniscus motion as the balance of surface tension force and air backpressure force, as follows:

$$P_{\text{atm}}\left(\frac{x}{L}\right)\pi r^2\propto 2\pi r\gamma\cos\theta_d. \tag{3.26}$$

ATTENTION: The Singapore Copyright Act applies to the use of this document. Nanyang Technological University Library

Equation (3.26) brings about a relation among the liquid penetration, capillary length and radius, and contact angle of any two experiments (i and j) as follows:

$$\frac{x_i}{x_j} \propto \left(\frac{r_j}{r_i}\right)\left(\frac{L_i}{L_j}\right)\left(\frac{\cos\theta_{D,i}}{\cos\theta_{D,j}}\right). \tag{3.27}$$

Equation (3.27) is readily verified by our experimental data. This equation also shows the significant role played by capillary radius and length in such closed-end capillary flow experiments. Moreover, modification of the capillary surface can alter liquid penetration.

In addition, equation (3.24) shows that it is possible to obtain a relation between maximum liquid displacement (x^{∞}) and equilibrium contact angle (θ^0) by applying $\dot{x} = \ddot{x} = 0$ (i.e. stagnation point) as follows:

$$P_{\text{atm}} \frac{x^{\infty}}{L - x^{\infty}} = \frac{2\gamma\cos\theta^0}{r} \tag{3.28}$$

where $2\gamma\cos\theta^0/r$ represents the pressure drop across liquid-air interface (Laplace's equation) and $P_{\text{atm}}\left(x^{\infty}/L - x^{\infty}\right)$ denotes the air backpressure (gauge) at final position. This equation confirms that the air backpressure has effects on the equilibrium contact angle (θ^0), and thus on dynamic contact angle (θ_{d}) (see equation (3.8)).

4. Results and discussion

Since the trapped air is compressed during the process of the closed-end capillary flow, the advancing meniscus is subjected to varying pneumatic backpressure which exerts a drag force ($=\left[P_{\text{air}} - P_{\text{atm}}\right]\pi r^2$) on the meniscus, slows down and eventually halts its motion. Figure 3-10 shows the displacement of capillary filling of 1:1 glycerol-DI water mixture in capillary

ATTENTION: The Singapore Copyright Act applies to the use of this document. Nanyang Technological University Library

diameters ranging 300 to 700 μm. The total displacement in 300 μm, 500 μm and 700 μm capillaries are about 0.7 mm, 0.2 mm and 0.1 mm, respectively while the total length of the capillary tube is 100 mm. It is obvious that the total distance travelled by the meniscus in a smaller diameter capillary is longer. This is because the drag force from the pneumatic pressure of trapped air is proportional to r^2, and thus reduces more rapidly with decreasing capillary diameter than the driving surface tension force which is proportional to r (see equation (3.7)). It is also seen that the total liquid penetration length is significantly longer with decreasing capillary diameter. This behavior was previously shown by equation (3.27). If we take the data of capillary filling of 1:1 glycerol-DI water mixture in 300 μm capillary diameter as $x^{\infty} = 0.7$ mm, $L = 10$ cm, and $\theta^0 = 41$, using equation (3.27) we can obtain the capillary penetration for the same mixture in 500 μm and 700 μm capillaries as 0.2 mm and 0.12 mm respectively. These values are quite close to our experimental data. This indicates the correctness of our theoretical model.

The similar trend is obviously observed in Figure 3-11 (for 2:1 glycerol-DI water mixture) and Figure 3-12 (for 4:1 glycerol-DI water mixture). A comparison among figures 12 to 14 shows that the viscosity of the liquid does not affect the maximum displacement, but a more viscous liquid has a lower filling velocity and thus takes a longer time to reach the maximum displacement. Furthermore, the pressure rise is also higher in a smaller size capillary diameter. For example, the pressure rise in 300 μm capillary is roughly 700 Pa, while the pressure rise for 500 μm and 700 μm capillaries is 200 Pa and 100 Pa respectively (see Table 3-3). Figures 12 to 14 also show that the theoretical predictions agree reasonably well with the experimental data. In addition, the insets in figures 12 to 14 allow us to view more clearly the initial stages of capillary penetration.

ATTENTION: The Singapore Copyright Act applies to the use of this document. Nanyang Technological University Library

In order to provide larger air volumes at the closed end of the capillary, experiments were performed in 200 μm capillaries with extended volumes by attaching syringes having volumes of 0.1 and 0.4 ml to the one-end of capillaries, and the results of capillary filling are shown in Figure 3-13. It should be pointed out that in the numerical calculations using equation (3.24), the attached volume should be converted to an equivalent length of a cylinder with the same diameter as the capillary tube. Thus, the effective total length L in the calculations is the summation of the capillary tube length and the equivalent length of the attached syringe. For a larger attached volume (AV), the total displacement was observed to be longer. For an attached volume of 0.1 ml, the liquid displaces roughly about 60 mm, and the liquid could completely fill the entire capillary tube (length 100 mm) with attached 0.4 ml volume. This demonstrates that the penetration length of capillary filling can be readily controlled by the entrapped air volume. From a practical point of view, these findings are useful because during the filling process it allows us to adjust the syringe plunge to change the air backpressure externally, and thus to control the meniscus position and velocity in the capillary tube. This is applicable in capillary pumping applications where air pressure is used to manipulate liquid transport [14]. In addition, it can be considered for the application of utilizing surface tension driven flow for sample loading where the liquid moves so fast at the initial stage that it is difficult to control the amount of liquid which is needed. Employing an air backpressure can certainly reduce the liquid transport velocity and thus can achieve a better control of the process.

The pressure rise in 200 μm capillary with attachment of syringe is higher than other capillary sizes, and its value is roughly equal to 1 kPa. Figure 3-13 shows a reasonable agreement between the experimental data and the theoretical calculations. The partial discrepancy between the experimental results and the theoretical calculations at the length of 100 mm is due to meniscus arrival to the point of capillary-syringe attachment where the surface tension

ATTENTION: The Singapore Copyright Act applies to the use of this document. Nanyang Technological University Library

driven flow suddenly stops. Again, equation (3.27) can be used to predict the penetration length of capillary filling in the presence of extended volume by using attached syringes. For example, based on the data of capillary filling of 1:1 glycerol-DI water mixture in 300 μm capillary diameter, equation (3.27) can estimate the capillary penetration for the same mixture in 200 μm and with attachment volume of 0.1 ml as 42 mm. This value is also satisfactorily close to our experimental data.

From theory, this can be inferred that pneumatic air backpressure also reduces K_{W}^{0}. Although the desorption process of air molecules from adsorption sites on solid surface before each subsequent adsorption of liquid molecules to the same adsorption sites is ignored in the derivation of MKT theory (equation (3.8)), this effect is significant in the presence of air backpressure. An increase in the pneumatic pressure will slow down the desorption process, and consequently reduce the rate of adsorption process. Furthermore, this effect can be verified from the expression of K_{W}^{0} (equation (3.9)) as a function of the specific activation free energy of wetting $\Delta g_{\mathrm{W}}^{*}$ which is regarded as an energy barrier of wetting processes [39]. This equation shows that the growing resistance from the air molecules in front of the liquid molecules owing to the air backpressure will increase the activation energy ($\Delta g_{\mathrm{W}}^{*}$), and thus decrease the value of K_{W}^{0} comparing to the conventional open-end capillary flows.

In the same manner, at the equilibrium point the accrued air backpressure ($\left[P_{\text{air at equilibrium}} - P_{\text{atm}}\right] > 0$) reduces the equilibrium contact angle θ^{0}. This effect which was described by equation (3.28) can also be easily seen from Laplace's equation $P_{\mathrm{C}} = P_{\text{air at equilibrium}} - P_{\text{atm}} = 2\gamma/R$, where P_{C} is the capillary pressure and R ($= r/\cos\theta^{0}$) is the radius of curvature. As a result, the higher the equilibrium air backpressure, the lower is θ^{0} (see Figure 3-14). In order to eliminate uncertainties in experimentally determined θ^{0}, one

ATTENTION: The Singapore Copyright Act applies to the use of this document. Nanyang Technological University Library

way is to calculate it from experiments of capillary rising [36, 40]. This approach is adopted here too. Thus, the corresponding values of θ^0 (as appeared in tables 4 and 5 and figure 16) were obtained by adjusting the stagnation point of equation (3.24) (at which $\dot{x} = \ddot{x} = 0$) to the maximum displacement of the liquid column in each experiment. The values of $P_{\text{air at equilibrium}}$ were obtained directly from the numerical calculations of equation (3.24).

To form a relationship among important physical factors influencing flows in a closed-end capillary, a dimensionless analysis is performed. Rewriting equation (3.24) with addition of the inertia term in a dimensionless form by introducing $x^* = x/r$ and $t^* = t/\tau$, we can obtain:

$$\mathrm{Re}\left(x^*\ddot{x}^* + \dot{x}^{*2}\right) = 4Ca\left[(\cos\theta^0 - \frac{\zeta}{\eta}\dot{x}^*) - 4x^*\dot{x}^* - \frac{P_{\text{atm}}}{2\gamma/r}\frac{x^*}{L/r - x^*}\right]. \qquad (3.29)$$

Here, $\tau = \eta/(\gamma/r)$ can be interpreted as a time scale for capillary rise, and it is proportional to viscous effect and inversely proportional to capillarity effect. $\mathrm{Re} = 2\rho\dot{x}r/\eta$ and $Ca = \eta\dot{x}/\gamma$ are the Reynolds number and Capillary number, respectively. $P_{\text{atm}}/(2\gamma/r)$ is the ratio of the ambient pressure to capillary pressure ($P_C = 2\gamma/r$) of a completely wetting liquid and ζ/η is the ratio of the coefficient of wetting line friction to the bulk dynamic viscosity. An insight to the results of liquid column displacements of figures 12 to 14 implies that $L(=100\,mm) >> x$ (or $L/r >> x^*$). Thus it is possible to rewrite the nonlinear term $x^*/(L/r - x^*)$ in a linear form $x^*/(L/r)$, suggesting that the presence of air backpressure does not add to the nonlinearity of the underlying physics involved in such flows. In analogy to the well-known Washburn equation, such flow characteristic can exhibit a power-law dependency of meniscus position on time, namely $x^* = \beta \times (t^*)^{\alpha}$ with β being a constant depending on liquid properties. According to Washburn's equation, meniscus position is a

ATTENTION: The Singapore Copyright Act applies to the use of this document. Nanyang Technological University Library

function of time with an exponential component of α = 0.5. However, both Table 3-5 and Figure 3-15 show that the values of α in closed-end capillary flows are lower than 0.5, and are dependent on the solid-liquid interface properties (ζ/η). It is noted that the equation used in plotting Figure 3-15 is $\log x^* = \log\beta + \alpha \log t^*$, where α is the slope of line. Figure 3-15 further validates our previous finding that capillary liquid transport in closed-end capillary tubes is mostly influenced by the capillary diameter.

ATTENTION: The Singapore Copyright Act applies to the use of this document. Nanyang Technological University Library

Table 3-3: Physical properties and dynamic parameters of the flow in 300 to 700 µm capillaries.

Liquid mixture concentration	**Capillary diameter**	θ^0	$\lambda\,[nm]$	K_W^0	$\zeta\,[Pa.s]$	$P_{\text{air at equilibrium}}/P_{\text{atm}}$
80% glycerol-DI water	300	38	0.41	6.00×10^6	10	1.0069
67% glycerol-DI water	300	42	0.44	5.80×10^6	8	1.0065
50% glycerol-DI water	300	41	0.47	7.85×10^6	5	1.0066
80% glycerol-DI water	500	68	0.53	7.00×10^5	40	1.0019
67% glycerol-DI water	500	69	0.54	1.30×10^6	20	1.0019
50% glycerol-DI water	500	68	0.54	4.30×10^6	6	1.0020
80% glycerol-DI water	700	70	0.56	2.90×10^5	80	1.0013
67% glycerol-DI water	700	73	0.57	7.30×10^5	30	1.0011
50% glycerol-DI water	700	73	0.58	2.10×10^6	10	1.001

ATTENTION: The Singapore Copyright Act applies to the use of this document. Nanyang Technological University Library

Table 3-4: Physical properties and dynamic parameters of flow in 200 μm capillaries.

Liquid mixture concentration	**Attached volume [ml]**	θ^0	$\lambda\,[nm]$	K_W^0	$\zeta\,[Pa.s]$	$P_{\text{air at equilibrium}}/P_{\text{atm}}$
80% glycerol-DI water	0.1	25	0.39	6.60×10^6	10	1.0117
50% glycerol-DI water	0.1	24	0.38	8.90×10^6	8	1.0121
80% glycerol-DI water	0.4	25	0.41	3.90×10^6	15	1.0118
50% glycerol-DI water	0.4	24	0.42	2.40×10^6	22	1.0120

Table 3-5: The values of dimensionless groups

Percentage of the mixture	**Diameter (μm)**	α	$P_{\text{atm}}/(2\gamma/r)$	ζ/η
80%	300	0.21	113.6	125
67%	300	0.21	111.9	289.59
50%	300	0.31	111.9	598.87
80%	500	0.32	189.4	500
67%	500	0.19	186. 6	723.98
50%	500	0.33	186. 6	718.65
80%	700	0.31	265.1	1000
67%	700	0.42	261.2	1085.9
50%	700	0.41	261.2	1197.7

ATTENTION: The Singapore Copyright Act applies to the use of this document. Nanyang Technological University Library

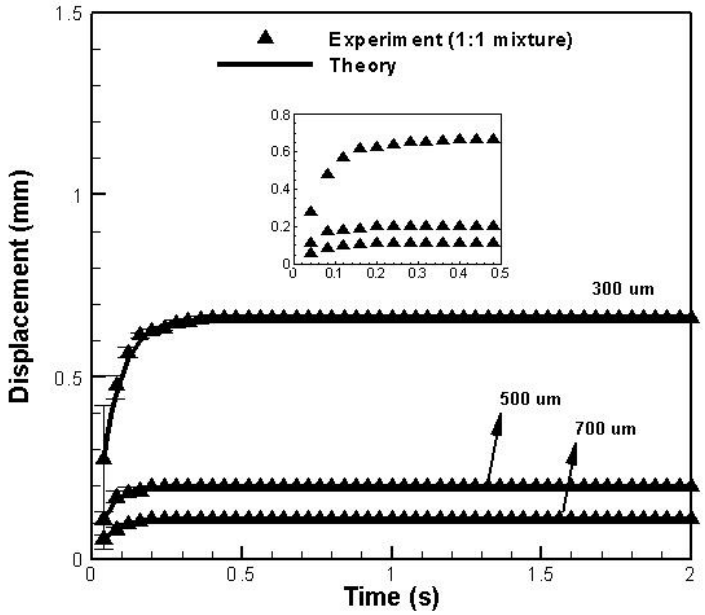

Figure 3-10: Comparison of experiment with theory for 1:1 Glycerol – DI water mixture and 300, 500, and 700 µm capillary tubes, inset shows initial stages of penetration.

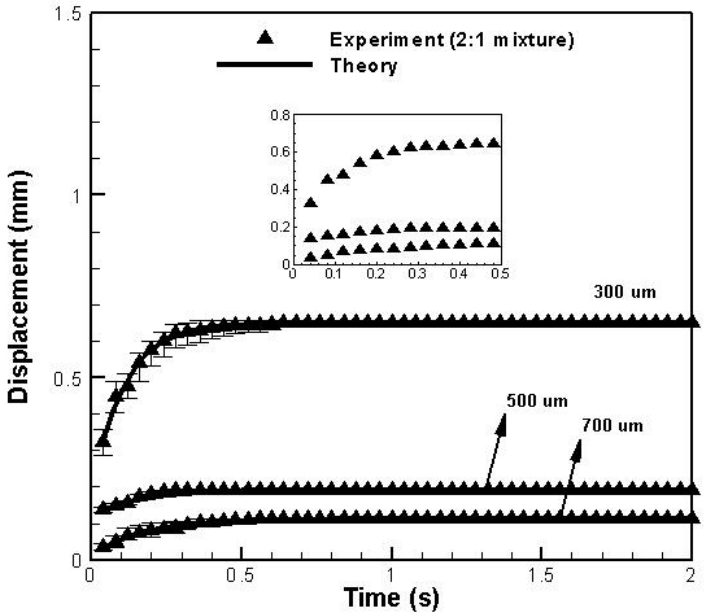

Figure 3-11: Comparison of experiment with theory for 2:1 Glycerol – DI water mixture and 300, 500, and 700 µm capillary tubes, inset shows initial stages of penetration.

ATTENTION: The Singapore Copyright Act applies to the use of this document. Nanyang Technological University Library

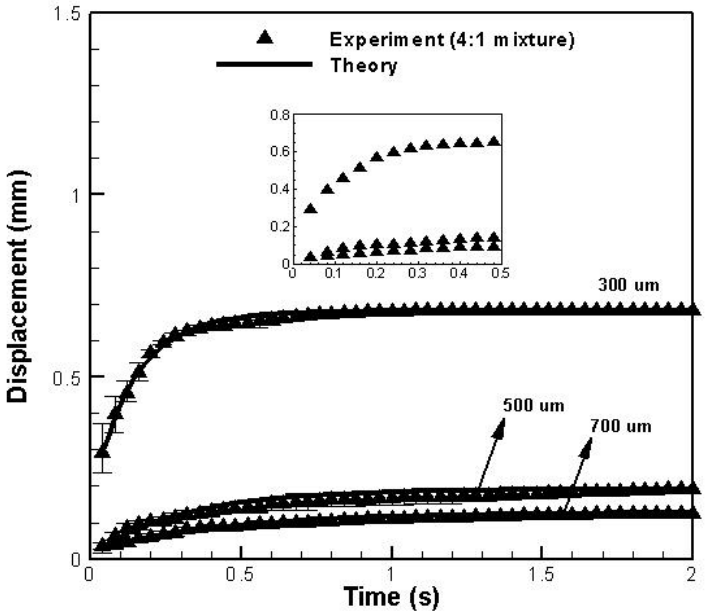

Figure 3-12: Comparison of experiment with theory for 4:1 Glycerol – DI water mixture and 300, 500, and 700 µm capillary tubes, inset shows initial stages of penetration.

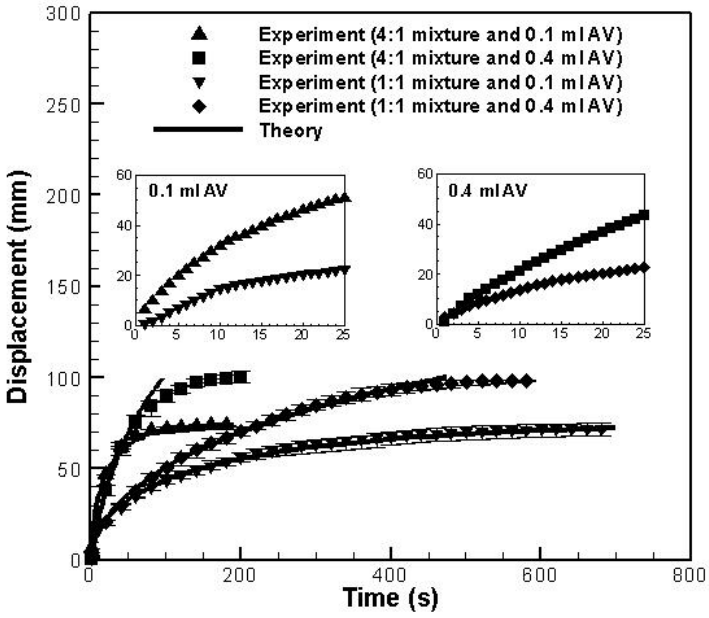

Figure 3-13: Comparison of experimental data with numerical calculations for 2:1 glycerol-DI water mixture and 300, 500 and 700 µm capillary tubes.

ATTENTION: The Singapore Copyright Act applies to the use of this document. Nanyang Technological University Library

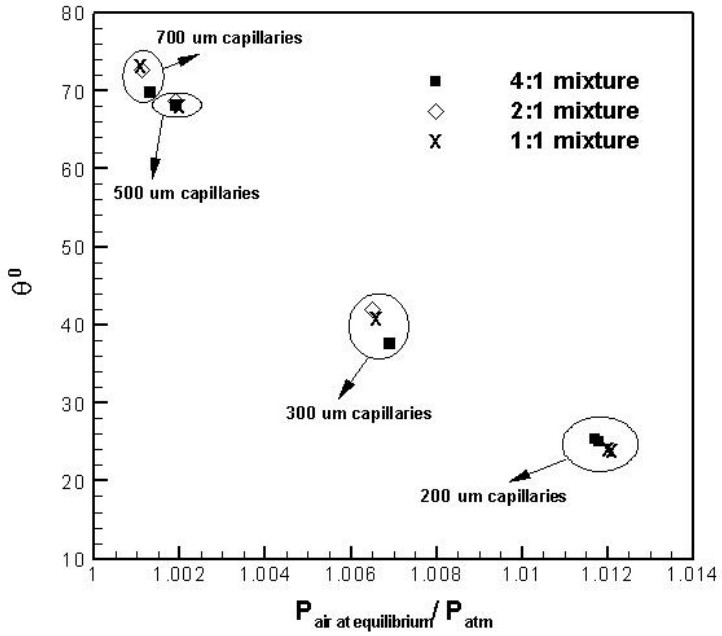

Figure 3-14: Equilibrium contact angle plotted versus ratio of equilibrium air back pressure to atmospheric pressure.

ATTENTION: The Singapore Copyright Act applies to the use of this document. Nanyang Technological University Library

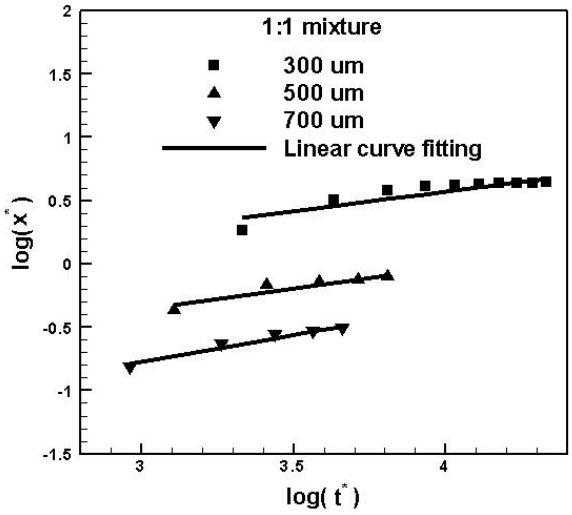

(a)

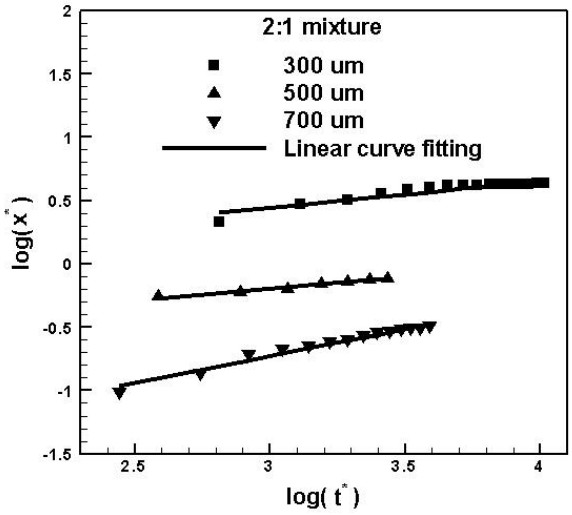

(b)

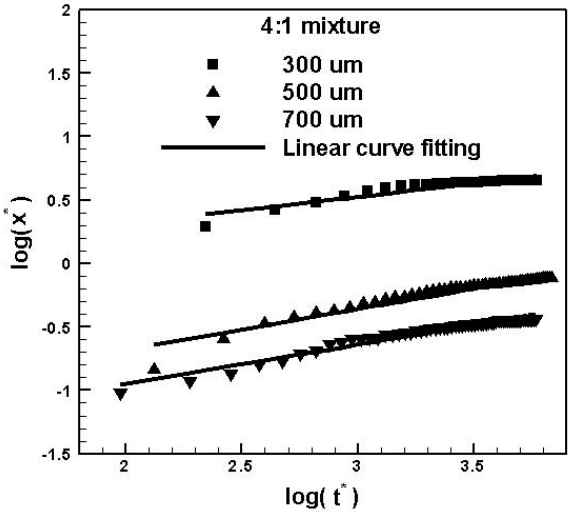

(c)

Figure 3-15: Logarithm of dimensionless meniscus position plotted versus logarithm of dimensionless time, (a) 1:1 mixture, (b) 2:1 mixture, and (c) 4:1 mixture.

ATTENTION: The Singapore Copyright Act applies to the use of this document. Nanyang Technological University Library

Chapter 4: Surface tension driven capillary flow from a pendant droplet

1. Introduction

In this chapter, we report on the first experimental study on the surface tension driven capillary flow from a pendant droplet into a horizontal glass capillary. It is aimed to examine the effect of finite sized liquid reservoir on the dynamic behavior of such capillary flow in comparison with the surface tension driven capillary flow from an infinite reservoir. In the theoretical analysis, we apply the concept of Gibb's free energy of surface to derive the contribution of the finite sized reservoir in the total surface tension force. Three models are proposed to describe the pendant droplet shape.

2. Experimental investigation

General aspects of these experiments are stated in Sec. Materials and methods. In this section, I only focus on the specific aspects of experiments with pendant droplet as the reservoir. In the experiments of capillary flow from a finite sized reservoir, gauge 21 size dispenser needle tips with an inner diameter of 0.51 mm and outer diameter of 0.81 mm purchased from EFD Inc. were used to form liquid pendant droplets. The liquid droplet volume was maintained around 10 ± 0.4 µl (as the largest possible drop volume obtained by trial and error) by setting appropriate time and speed of pumping in all of the experiments. The capillaries (resting horizontally on the holder) were aligned exactly to the center of the pendant droplet (see Figure 4-1). Otherwise, the droplets would fall off before the liquid could completely flow

ATTENTION: The Singapore Copyright Act applies to the use of this document. Nanyang Technological University Library

into the capillary. It was noticed that if the droplet volume was too large, the liquid droplet might engulf the capillary from the outside which could be a serious problem for small capillaries such as 300 μm. Thus not all of the liquid would go through the capillary. An experiment was considered successful if all of the liquid mass had flowed into the capillary and none remained outside. This set up a basis for conducting experiments. Air bubbles and impurities inside the syringe could affect the droplet shape and led to difficulties in obtaining accurate results.

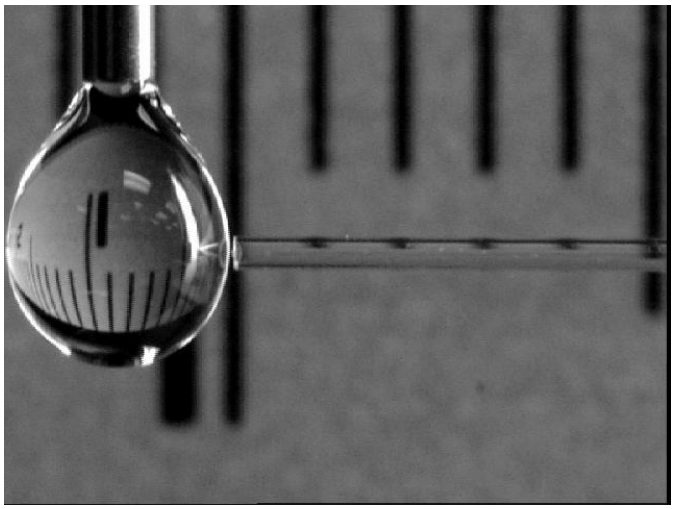

Figure 4-1: Capillary centered to the liquid droplet.

Moreover, since the glass tube is hydrophilic, some amount of residue could remain on the outer surface of the capillary tube, as shown in Figure 4-2. This usually occurred towards the end of the experiment when the droplet volume became very small and elongated between the needle tip and the capillary entrance.

ATTENTION: The Singapore Copyright Act applies to the use of this document. Nanyang Technological University Library

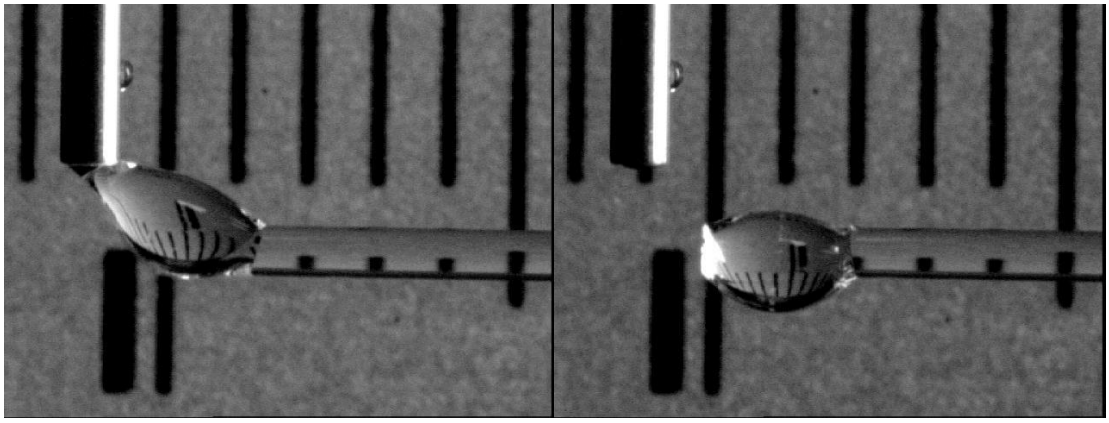

Figure 4-2: Elongated droplet before forming a residue on the outer surface of the capillary tube (left); droplet residue on the outer surface of the capillary tube (right).

To prevent the liquid from sticking to the outside of the capillary, wax was carefully applied around the outer surface of the capillary entrance to create a hydrophobic surface. This method was effective and allowed all of the liquid to enter the capillary eventually. A typical satisfactory experimental test is shown in Figure 4-3.

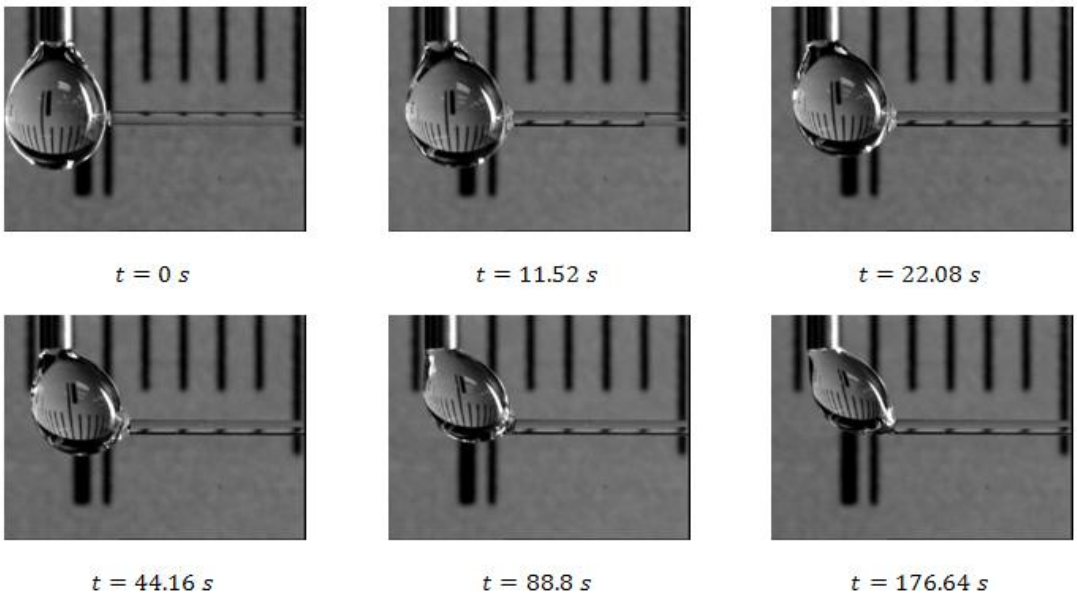

Figure 4-3: Change in droplet surface area and volume during capillary action.

As the capillaries were open-end in these experiments, meniscus motion was very fast to be captured by CCD camera. Thus glycerol-DI water solutions of higher viscosity ranging 80 to

ATTENTION: The Singapore Copyright Act applies to the use of this document. Nanyang Technological University Library

450 mPa.s as well as pure glycerol were used. In addition, capillary diameters 300 to 700 µm were used in the experiments. The quality of the droplet shape which had significant influence on experimental results was perturbed by various effects:

1. Vibrations
2. Verticality of the needle. The symmetry of the droplet could be affected if the needle was not completely vertical, thus leading to liquid droplet engulfing outer surface of the tube or liquid droplet falling off before being thoroughly sucked inside the capillary.
3. Impurities, fibers from cleaning materials and air bubbles could essentially affect the quality of the droplet.

Experimental data of these experiments are first published in [126].

3. Theoretical modeling

It is known that a pressure difference exists across any curved interface which is proportional to the interface curvature and is higher in the concave side than in the convex side (e.g. the pressure inside a liquid drop in higher than its surrounding pressure). Thus, manipulating this pressure difference (which is also present at the interface of a liquid pendent droplet) it is possible to produce liquid flow inside a capillary tube (see Figure 4-4).

ATTENTION: The Singapore Copyright Act applies to the use of this document. Nanyang Technological University Library

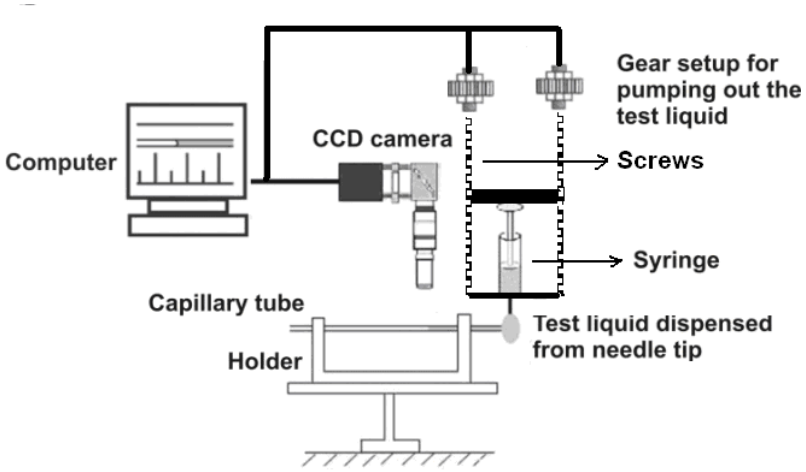

Figure 4-4: Schematic of the setup in droplet-driven capillary flow.

Comparing schematic setup of Figure 4-4 to that of Figure 3-6, it is obvious that the pendent droplet is acting as a reservoir. In this section, the main aim is to model the behavior of this droplet reservoir so as to obtain its significance on the dynamics of meniscus motion.

As seen in Figure 4-5, during liquid penetration, the reduction in droplet volume causes a subsequent reduction in droplet mean radius $\bar{R} = \sqrt[3]{V}$. Consequently, the droplet curvature ($\kappa \propto 1/\bar{R}$) increases. Then, according to the Laplace equation (which relates the pressure drop across liquid interface to its radius of curvature):

$$\Delta p_c = \gamma\kappa,$$

an increasing force is generated on the moving meniscus. This extra force, which does not exist in an infinite reservoir surface tension driven flow, results in meniscus further displacement at a higher rate.

ATTENTION: The Singapore Copyright Act applies to the use of this document. Nanyang Technological University Library

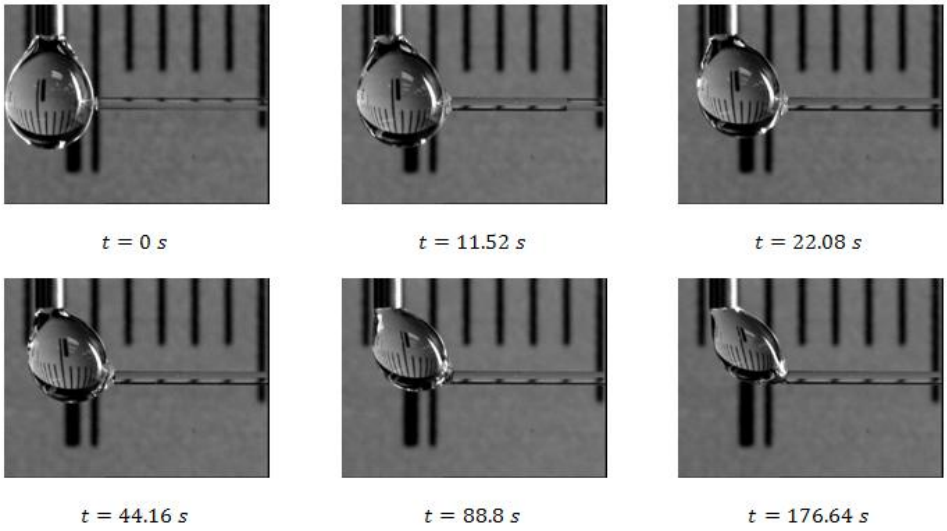

Figure 4-5: liquid pumped out from syringe and dispensed from needle tip; capillary tube aligned to the center of droplet; change in droplet volume and surface area during capillary action.

According to the general relation between a force and its associated potential energy [127], surface tension force can be derived from the Gibb's free energy of surface ($G = \sum \gamma_i A_i$) in an isothermal, isobaric thermodynamic system, where γ_i is the interfacial tension of any interface of area A_i within the system. That is $F_\gamma = -dG/dx$ in which F_γ is the total surface tension force of the system, and x represents the general coordinate along the direction of meniscus motion.

With regard to Figure 4-6, in the present study, there are two liquid-air interfaces: the interface at the liquid pendant droplet ($A_{la,1}$) and the interface at the meniscus concave side ($A_{la,2}$). Further, there is one solid-liquid interface ($A_{sl} = 2\pi rx$) and one solid-air interface ($A_{sa} = 2\pi r(L - x)$). Thus the total Gibb's free energy of system after some simplifications is as follows:

$$G = \gamma A_{la,1} - 2\pi rx(\gamma_{sa} - \gamma_{sl}) + \left[\gamma A_{la,2} + 2\pi r\gamma_{sl} L\right]. \tag{4.1}$$

ATTENTION: The Singapore Copyright Act applies to the use of this document. Nanyang Technological University Library

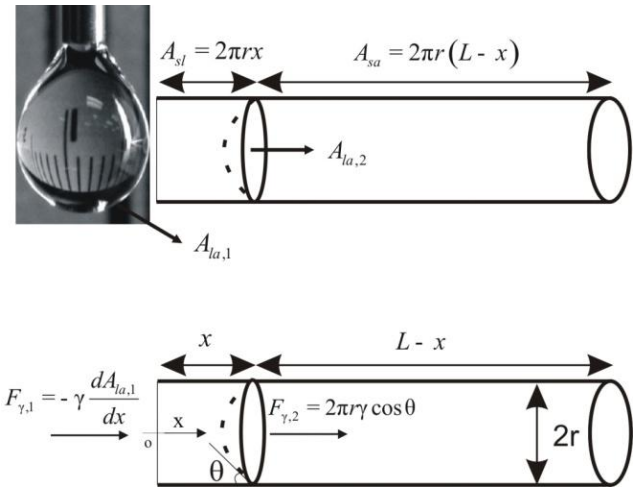

Figure 4-6: Schematic of the interfaces and the two surface tension forces.

Inserting Young's equation ($\gamma\cos\theta = \gamma_{sa} - \gamma_{sl}$) into equation (4.1) and performing derivation with respect to *x*, the following expression for the total surface tension force is obtained [128]:

$$F_{\gamma} = -\gamma.\left(\frac{dA_{sa}}{dx}\cos\theta + \frac{dA_{la,1}}{dx}\right) = -\gamma.\left(-2\pi r\cos\theta + \frac{dA_{la,1}}{dx}\right). \qquad (4.2)$$

Here F_{γ} is total driving surface tension force. From equation (4.2) it is obvious that F_{γ} is a combination of two capillary forces: $F_{\gamma,1} = -\gamma\left(dA_1/dx\right)$ due to change in pendent droplet outer surface, and $F_{\gamma,2} = 2\pi r\gamma\cos\theta$ due to conventional capillary force within the capillary tube. It is noted that in the derivation of equation (4.2), the variation of liquid-air interface is assumed negligible ($dA_{la,1}/dx \cong 0$). The other assumption which is blurred in the derivation of equation (4.2) is that the meniscus is approximated as a spherical cap. As discussed in the previous chapter, this usually requires that the Weber, and Capillary numbers to be small, namely $We = \rho rU^2/\gamma << 1$, and $Ca = \eta U/\gamma << 1$, [127]. For the range of capillary radii as well as glycerol-DI water mixtures used in our experiments, these conditions are satisfied (see Table 4-1). In addition, Reynolds numbers and transition times to viscous dominant flow

ATTENTION: The Singapore Copyright Act applies to the use of this document. Nanyang Technological University Library

are also very small, which certifies that the flow is laminar and inertia effects are negligible (see Table 4-1). Further inspection in our experimental data shows that the inertia force is lower than the two other existing forces (surface tension force and viscous force) to the order of 10^{-4}.

Table 4-1: We and Ca numbers for liquid concentrations used in the experiments, the capillary radius is 350 µm.

Liquid concentration	**Re_{max}** $\left(\rho U_{max} D/\eta\right)$	**We_{max}** $\left(\rho U_{max}^2 D/\gamma\right)$	**Ca_{max}** $\left(\eta U_{max}/\gamma\right)$	$\tau = \rho r^2/4\eta$ $[ms]$
4:1 glycerol/water	~ 0.1	1.29×10^{-3}	1.21×10^{-2}	~ 0.5
6:1 glycerol/water	< 0.1	1.33×10^{-3}	2.55×10^{-2}	< 0.5
8:1 glycerol/water	< 0.1	1.35×10^{-3}	5.06×10^{-2}	< 0.5
10:1 glycerol/water	~ 0.01	1.36×10^{-3}	7.09×10^{-2}	~ 0.1
Pure glycerol	~ 0.01	1.41×10^{-3}	1.25×10^{-1}	< 0.1

Thus, based on a one dimensional simplification, it is possible to write the equation of meniscus motion as the balance of surface tension force and viscous drag force, as follows:

$$\dot{x} = \frac{-\gamma\left[\frac{dA_{la,1}}{dx} - 2\pi r\cos\theta\right]}{8\pi\eta x}, \tag{4.3}$$

and as a result:

$$\int_{x_0}^{x} x dx = \int_{t_0}^{t}\left[\frac{-\gamma\left[\frac{dA_1}{dx} - 2\pi r\cos\theta\right]}{8\pi\eta}\right]dt$$

$$x^2 - x_0^2 = \frac{2\pi r\gamma\cos\theta}{4\pi\eta}\left(t - t_0\right) + \frac{\gamma}{4\pi\eta}\int_{t_0}^{t}\left[-\frac{dA_1}{dx}\right]dt$$

ATTENTION: The Singapore Copyright Act applies to the use of this document. Nanyang Technological University Library

$$x = \frac{1}{\sqrt{4\pi\eta}} \sqrt{2\pi r\gamma \cos\theta \left(t - t_0\right) + \gamma \int_{t_0}^{t} \left[-\frac{dA_1}{dx} \right] dt + x_0^2} \tag{4.4}$$

where $\left(x_0, t_0\right)$, i.e. the starting position and time of penetration, are obtained from experimental data.

Pendant droplet geometry

The second term in the right hand side of equation (4.4) (under the integral) is due to droplet surface area change during the capillary action. It is obvious that in the case of an infinite reservoir, the change in reservoir surface area is negligible and this term drops, so that equation (4.4) becomes Washburn equation. Thus, it is necessary to represent the pendant droplet shape with an appropriate model which can give a satisfactory prediction of meniscus displacement. Here, three models are proposed:

Spherical model

In the spherical model, it is assumed that the pendant droplet retains a spherical geometry with a varying radius $R\left(t\right)$ during the capillary flow (see Figure 4-7). Thus, the surface area of the pendant droplet is $A_{la,1} = 4\pi R\left(t\right)^2$, and its derivative with respect to *x* gives:

$$\frac{dA_{la,1}}{dx} = 8\pi R\left(t\right).\frac{dR\left(t\right)}{dx}. \tag{4.5}$$

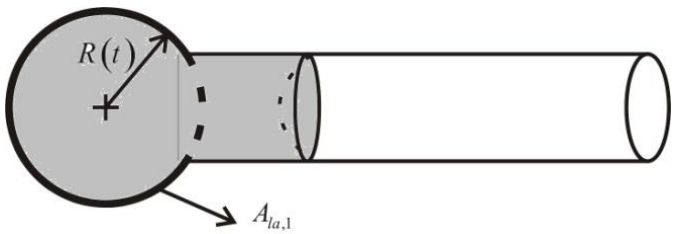

Figure 4-7: Capillary flow from a spherical pendant droplet.

ATTENTION: The Singapore Copyright Act applies to the use of this document. Nanyang Technological University Library

The mass conservation suggests that the volume of the spherical droplet at time t ($V(t)=\frac{4}{3}\pi R(t)^3$) equals the initial volume of the spherical droplet ($V_0=\frac{4}{3}\pi R_0^3$) subtracts the volume of liquid that has entered the capillary, namely $\frac{4}{3}\pi R(t)^3=\frac{4}{3}\pi R_0^3-\pi r^2 x$. Accordingly, the relations for $R(t)$ and $dR(t)/dx$ can be obtained as follows:

$$R(t)=\sqrt[3]{R_0^3-\tfrac{3}{4}r^2x}, \tag{4.6}$$

$$\frac{dR(t)}{dx}=-\frac{r^2}{4R(t)^2}. \tag{4.7}$$

Substitution of equations (4.5), (4.6) and (4.7) in equation (4.4) gives the equation of meniscus motion in capillary flow from a spherical pendant droplet as follows:

$$x=\frac{1}{\sqrt{4\pi\eta}}\sqrt{2\pi r\gamma\cos\theta\left(t-t_0\right)+\int_{t_0}^{t}\left[2\pi\gamma\frac{r^2}{\sqrt[3]{R_0^3-\frac{3}{4}r^2x}}\right]dt+x_0^2}. \tag{4.8}$$

Spheroidal model

In the spheroidal model, both polar radius $a(t)$ and equatorial radius $b(t)$ which describe a spheroidal shape for the droplet are varying during the capillary motion (see Figure 4-8). However the eccentricity $e=\sin\left(\cos^{-1}b/a\right)$ (or the ratio(b/a)) is assumed to remain constant in the entire process. The surface area of a spheroid and its derivative with respect to *x* are as follows:

$$A_{la,1}=2\pi\left[1+\frac{\cos^{-1}\dfrac{b}{a}}{\dfrac{b}{a}\sqrt{1-\left(\dfrac{b}{a}\right)^2}}\right]b(t)^2, \tag{4.9}$$

ATTENTION: The Singapore Copyright Act applies to the use of this document. Nanyang Technological University Library

$$\frac{dA_{la,1}}{dx} = 4\pi\left[1+\frac{\cos^{-1}\frac{b}{a}}{\frac{b}{a}\sqrt{1-\left(\frac{b}{a}\right)^2}}\right]b(t).\left[\frac{db(t)}{dx}\right]. \tag{4.10}$$

According to the mass conservation, the volume of the spheroidal droplet at time t ($V(t)=\frac{4}{3}\pi(b/a)^{-1}b(t)^3$) is equal to the initial volume (V_0) subtracts the volume of liquid that has entered the capillary, namely $\frac{4}{3}\pi(b/a)^{-1}b(t)^3 = V_0 - \pi r^2 x$. As a result, the relations for $b(t)$ and $db(t)/dx$ can be obtained as follows:

$$b(t) = \sqrt[3]{\frac{V_0-\pi r^2 x}{\frac{4}{3}\pi(b/a)^{-1}}}, \tag{4.11}$$

$$\frac{db(t)}{dx} = -\frac{(b/a)r^2}{4b(t)^2}. \tag{4.12}$$

Accordingly, substitution of equations (4.10), (4.11) and (4.12) in equation (4.4) results in the following equation of meniscus motion in capillary flow from a spheroidal pendant droplet:

$$x = \frac{1}{\sqrt{4\pi\eta}}\sqrt{2\pi r\gamma\cos\theta(t-t_0)+\int_{t_0}^{t}\left[\gamma\pi\left[1+\frac{\cos^{-1}\frac{b}{a}}{\frac{b}{a}\sqrt{1-\left(\frac{b}{a}\right)^2}}\right]\frac{\frac{b}{a}r^2}{\sqrt[3]{\frac{V_0-\pi r^2 x}{\frac{4}{3}\pi(b/a)^{-1}}}}\right]dt + x_0^2}. \tag{4.13}$$

Comparing equation (4.13) with equation (4.8), it is obvious that for $a(t)=b(t)=R(t)$ the two equations are completely identical.

According to experimental observations, initially the ratio of b/a to be used in equation (4.13) is about 0.76 for all of our test liquids. However during liquid flow into the capillary, this ratio reduces gradually due to the elongation of pendant droplet between needle tip and

ATTENTION: The Singapore Copyright Act applies to the use of this document. Nanyang Technological University Library

capillary entrance, (see Figure 4-5 and Figure 4-8). This elongation proceeds until the liquid rather completely enters into the capillary. It is assumed that the ratio of b/a at this final point is very close to zero. Thus, an average value of 0.38 (=0.76/2) is approximated for b/a in the numerical calculations of equation (4.13).

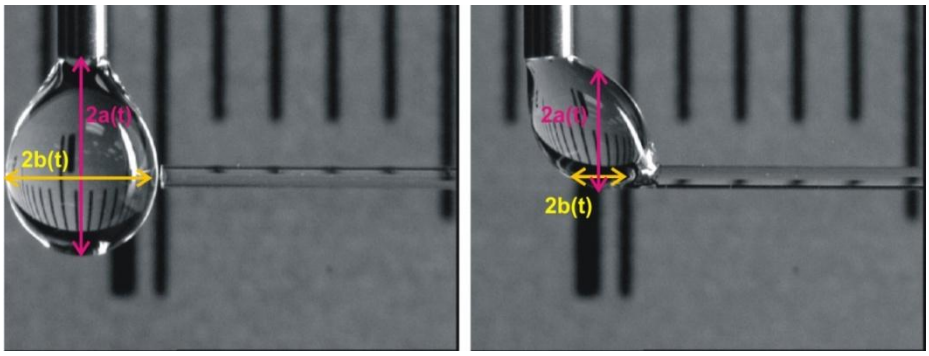

Figure 4-8: Capillary flow from a spheroidal pendent droplet. Elongation of the pendant droplet during capillary flow reduces the value of b/a; b/a = 0.76 at time t = 0 (left) and reduction in b/a during the process (right).

Egg-shaped model

In this model, a semi-empirical approach is used to predict the meniscus displacement. Here, it is assumed that the pendant droplet preserves an egg-shaped geometry in which the relation between surface area and volume is:

$$A_{la,1} = kV^{2/3} \tag{4.14}$$

where k is a varying dimensionless parameter, and is obtained from experimental data. The derivation of $A_{la,1}$ with respect to x to be used in equation (4.4) is as follows:

$$\frac{dA_{la,1}}{dx} = V^{2/3}\frac{dk}{dx} + \tfrac{2}{3}kV^{-1/3}\frac{dV}{dx}, \tag{4.15}$$

where $V = V_0 - \pi r^2 x$. Therefore, the equation of meniscus motion in capillary flow from an egg-shaped pendant droplet is as follows:

ATTENTION: The Singapore Copyright Act applies to the use of this document. Nanyang Technological University Library

$$x=\frac{1}{\sqrt{4\pi\eta}}\sqrt{2\pi r\gamma\cos\theta\left(t-t_0\right)+\int_{t_0}^{t}-\gamma\left[V^{2/3}\frac{dk}{dx}+\tfrac{2}{3}kV^{-1/3}\frac{dV}{dx}\right]dt+x_0^2}. \tag{4.16}$$

With regard to the steady state equation of meniscus motion, it is possible to calculate the empirical values of k. Thus, resolving equation (4.3) for k as an unknown variable it follows that:

$$\frac{dk}{dx}-\frac{\frac{2}{3}\pi r^2k}{\left(V_0-\pi r^2x\right)}=\frac{2\pi r\cos\theta-\dfrac{8\pi\eta x\dot{x}}{\gamma}}{\left(V_0-\pi r^2x\right)^{2/3}}$$

The solution of this first order ordinary differential equation is as follows:

$$k=\left(1-\frac{\pi\left(\frac{x}{r}\right)}{\left(\frac{V_0}{r^3}\right)}\right)^{-\frac{2}{3}}\left[\frac{2\pi\left(\frac{x}{r}\right)\cos\theta}{\left(\frac{V_0}{r^3}\right)^{\frac{2}{3}}}-\frac{4\pi\left(\frac{\eta\dot{x}}{\gamma}\right)\left(\frac{x}{r}\right)^2}{\left(\frac{V_0}{r^3}\right)^{\frac{2}{3}}}+k_0\right]. \tag{4.17}$$

Using experimental values of meniscus position x and velocity $\dot{x}$, empirical values of k and correspondingly dk/dx to be used in equation (4.16) are obtained.

Further insight shows that the egg-shaped model is a generalization of the spherical and spheroidal models. According to the definition of $k=A/V^{2/3}$ (equation (4.14)) in which k is a relating parameter between surface area and volume of a 3-D geometry, for sphere it follows that:

$$k_{sphere}=\sqrt[3]{36\pi},\quad \frac{dk_{sphere}}{dx}=0, \tag{4.18}$$

and for spheroid it follows that:

ATTENTION: The Singapore Copyright Act applies to the use of this document. Nanyang Technological University Library

$$k_{spheroid} = \left[\left(\frac{2\pi}{2.598} \right)^3 \frac{1}{b/a} \right]^{\frac{1}{3}} \cdot \left(\frac{b}{a} + \frac{\cos^{-1} \frac{b}{a}}{\sqrt{1-\left(\frac{b}{a}\right)^2}} \right) \tag{4.19}$$

in which for $b/a = 0.3817$ it results in:

$$k_{spheroid} = 5.526, \quad \frac{dk_{spheroid}}{dx} = 0 \tag{4.20}$$

Substitution of $b/a = 0.38$ gives $k_{spheroid} = 5.53$ and $dk_{spheroid}/dx = 0$. It is noted that $dk/dx \neq 0$ in the egg-shaped model plays an important role in satisfactory prediction of meniscus displacements, because it provides a correction to errors in calculating the real values of k. The initial value of k (k_0 in equation(4.17)) is taken to be equal to k of sphere, because initially the pendant droplet resembles a spherical geometry. This can also be justified by Bond number values being initially less than 1 for all of our solutions (see Table 4-2). In this table, R_0 is obtained from initial volume V_0 being equal to 10 µl in all of the experiments.

Table 4-2: Bond number values of initial pendent droplets.

Liquid concentration	4:1 glycerol/water	6:1 glycerol/water	8:1 glycerol/water	10:1 glycerol/water	Pure glycerol
Bo $\left(\rho g R_0^2/\gamma\right)$	0.32	0.33	0.34	0.34	0.35

ATTENTION: The Singapore Copyright Act applies to the use of this document. Nanyang Technological University Library

Dynamic contact angle

The other variable parameter of this capillary flow is the local contact angle (θ). As discussed in Sec. Dynamic contact angle, the local contact angle becomes dynamic (θ_d) when the liquid front advances on solid surface. The driving energy (due to the out of balance surface tension force) is dissipated at the moving front by various modes of energy dissipation. Molecular kinetics theory (MKT) relates this dissipative effect to solid-liquid molecular interactions introducing a fictitious friction at the moving liquid wetting front in the process of layer by layer advancement of liquid molecules on adsorption sites on the solid surface. The dynamics of wetting thus depends significantly on the friction coefficient (ζ) of this liquid wetting front [44].

4. Results and discussion

According to equation (4.2), the ratio of surface tension force in capillary flow from a pendant droplet to that of an infinite reservoir is as follows:

$$\frac{F_{ST}\big|_{\text{droplet reservoir}}}{F_{ST}\big|_{\text{infinite reservoir}}} = 1 - \frac{\left(\frac{dA_{la,1}}{dx}\right)}{2\pi r\cos\theta}. \tag{4.21}$$

Since $dA_{la,1}/dx < 0$ the above ratio is always greater than 1. This validates the generation of an extra force due to the change in droplet surface area. This extra force leads to meniscus displacement at higher rates. More rapid motion is also justified from the ratio of meniscus displacements (supposing $x_0\left(t_0 = 0\right) = 0$):

ATTENTION: The Singapore Copyright Act applies to the use of this document. Nanyang Technological University Library

$$\frac{x_{\text{droplet reservoir}}}{x_{\text{infinite reservoir}}} = \sqrt{1+\frac{\int_0^t -\frac{dA_1}{dx}.dt}{2\pi r\cos\theta.t}} \tag{4.22}$$

$$\frac{\dot{x}_{\text{droplet driven}}}{\dot{x}_{\text{infinite reservoir}}} = \left[1+\frac{\int_0^t -\frac{dA_1}{dx}.dt}{2\pi r\cos\theta.t}\right]^{\frac{-1}{2}} \cdot \left[1+\frac{-\frac{dA_1}{dx}}{2\pi r\cos\theta}\right] \cong \left[1+\frac{-\frac{dA_1}{dx}}{2\pi r\cos\theta}\right]^{\frac{1}{2}} \tag{4.23}$$

As a result, the displacement of the liquid meniscus in the droplet-driven capillary flow is longer and the rate of displacement is higher due to the existence of the extra force. The approximation used in equation (4.23) (i.e. $\int_0^t \left[\left(dA_1/dx\right)/2\pi r\cos\theta.t\right]dt \cong \left(dA_1/dx\right)/2\pi r\cos\theta$) is valid at initial stages of capillary flow where the variation of droplet outer surface area with respect to the liquid column length is roughly the same.

In the theoretical analysis, the two main parameters of the flow are the dimensionless droplet geometry parameter (k) which relates surface area to volume, and the dynamic contact angle (θ_d). Three models are proposed to describe the pendant droplet geometry. It is shown that the egg-shaped model is a generalization of spherical and spheroidal models. However, it is stated that $dk/dx \neq 0$ in the egg-shaped model provides a correction to errors in the calculation of real values of k.

Figure 4-9, Figure 4-10 and Figure 4-11 show the distribution of k as obtained from equation (4.17). The general increase in k values is due to the elongation of the liquid droplet during capillary flow (Figure 4-5). However, the reduction in k values in some experiments with 300 µm capillary may be due to liquid covering the outer surface of the capillary which is stated to be a problem with this capillary diameter. Despite, the similar trend in k distributions in all of the experiments is promising. Moreover, MKT with characteristic parameters ζ, λ and

ATTENTION: The Singapore Copyright Act applies to the use of this document. Nanyang Technological University Library

K_W^0 is used to interpret the dynamic behavior in contact angle. Table 4-3 summarizes the values of ζ, λ, and K_W^0 being almost in the same range. These values are obtained by the procedure explained in Chapter 3.

Table 4-3: Physical properties and dynamic parameters of the capillary flow from a pendant droplet.

Liquid-solid system	$\gamma\,[N/m]$	$\eta\,[Pa.s]$	$\zeta\,[Pa.s]$	$\lambda\,[nm]$	K_W^0	ζ/η
80% glycerol-DI water	0.0652	0.08128	50	0.45	0.80×10^6	615
86% glycerol-DI water	0.0647	0.16527	50	0.42	1.17×10^6	303
89% glycerol-DI water	0.0643	0.32522	50	0.40	1.20×10^6	154
91% glycerol-DI water	0.0640	0.45377	50	0.39	1.22×10^6	110
Pure glycerol	0.0625	0.934	400	0.44	0.13×10^6	428

Figure 4-12, Figure 4-13 and Figure 4-14 show the comparison between the experimental data and the predictions using spherical, spheroidal and egg-shaped models. Data of surface tension driven flow from an infinite reservoir are also provided in these figures. It is obvious that the meniscus displacement in capillary flow from a liquid droplet (a finite reservoir) is faster than that from an infinite reservoir. However, the difference is more pronounced as the contact angle is higher [129]. This is because for high contact angles the contribution of surface tension force due to droplet surface area change (the second term in right hand side of equation (4.2)) is much more dominant in the total surface tension force than the contribution due to meniscus curvature inside the capillary (the first term in right hand side of equation (4.2)). Subplots of Figures 26 to 28 (under 4 to 1 mixture plot) show contact angles ranging

ATTENTION: The Singapore Copyright Act applies to the use of this document. Nanyang Technological University Library

90^o to 30^o, 90^o to 60^o, and 90^o to 80^o for 300 µm, 500 µm, and 700 µm capillaries, respectively. Higher contact angle in larger capillary diameters is related to higher We numbers ($2r\rho\dot{x}^2/\gamma$) for which inertia effects are stronger at the meniscus edge near the solid surface resulting in a blunter meniscus. Moreover, it is obvious that comparing to 300 µm capillary, the droplet with initial diameter of about 2.7 mm (this value is obtained from the initial volume of the liquid pendant droplet assumed as a sphere and being about 10 µL) is relatively more finite for 500 µm and 700 µm capillaries. Thus the difference between experiment and capillary flow from an infinite reservoir is lesser, the smaller is the capillary diameter. It is also found that the egg-shaped model provides the best prediction among the three models. The discrepancy between the experimental data and the spheroidal and spherical models is due to the simplifications of these two models. However, the spheroidal model predicts slightly better displacements.

ATTENTION: The Singapore Copyright Act applies to the use of this document. Nanyang Technological University Library

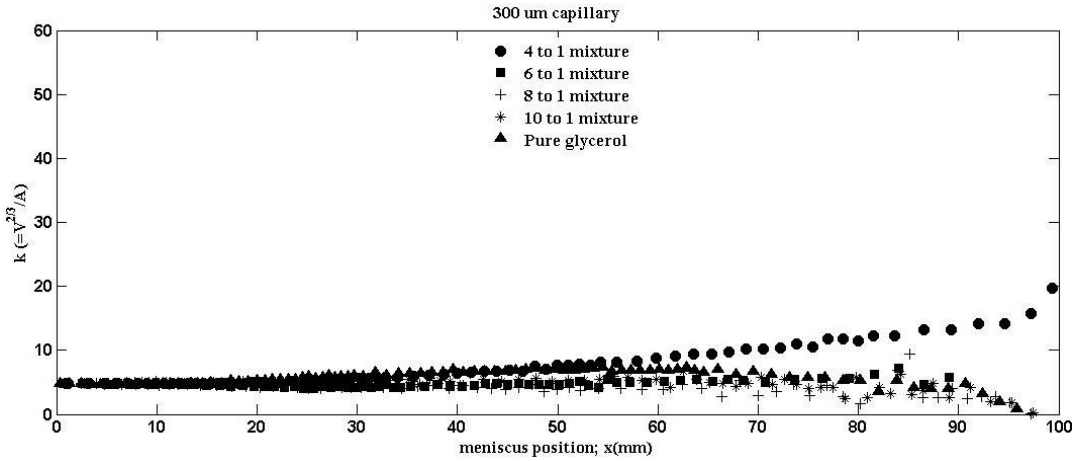

Figure 4-9: *k* distribution versus meniscus position (x) in 300 µm capillary.

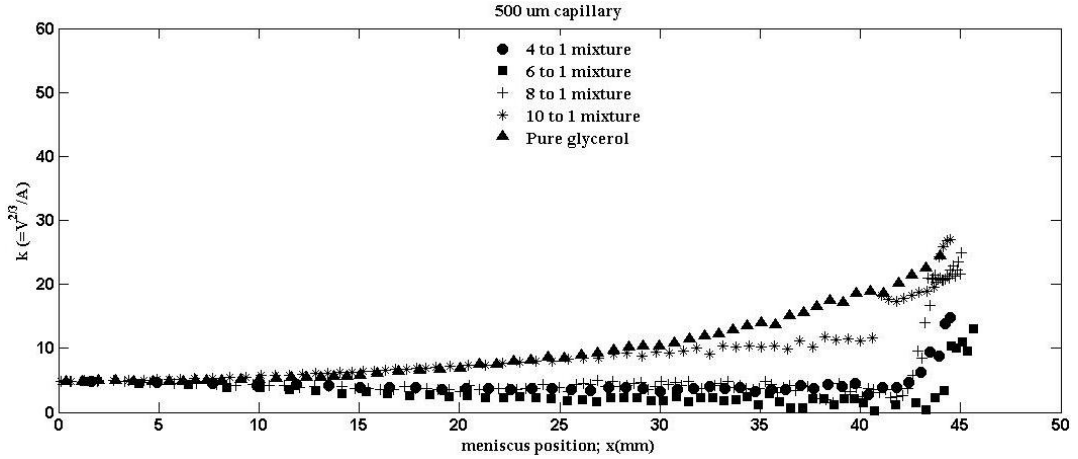

Figure 4-10: *k* distribution versus meniscus position (x) in 500 µm capillary.

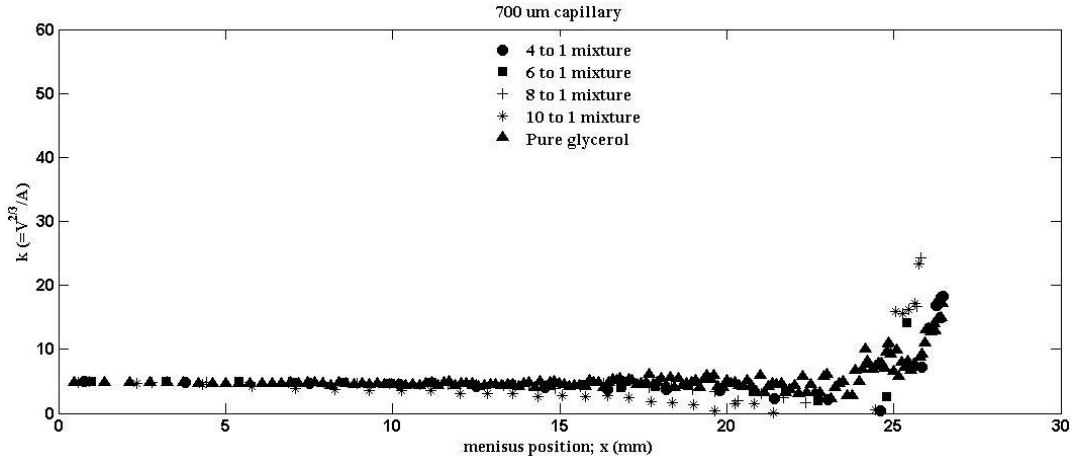

Figure 4-11: *k* distribution versus meniscus position (x) in 700 µm capillary.

ATTENTION: The Singapore Copyright Act applies to the use of this document. Nanyang Technological University Library

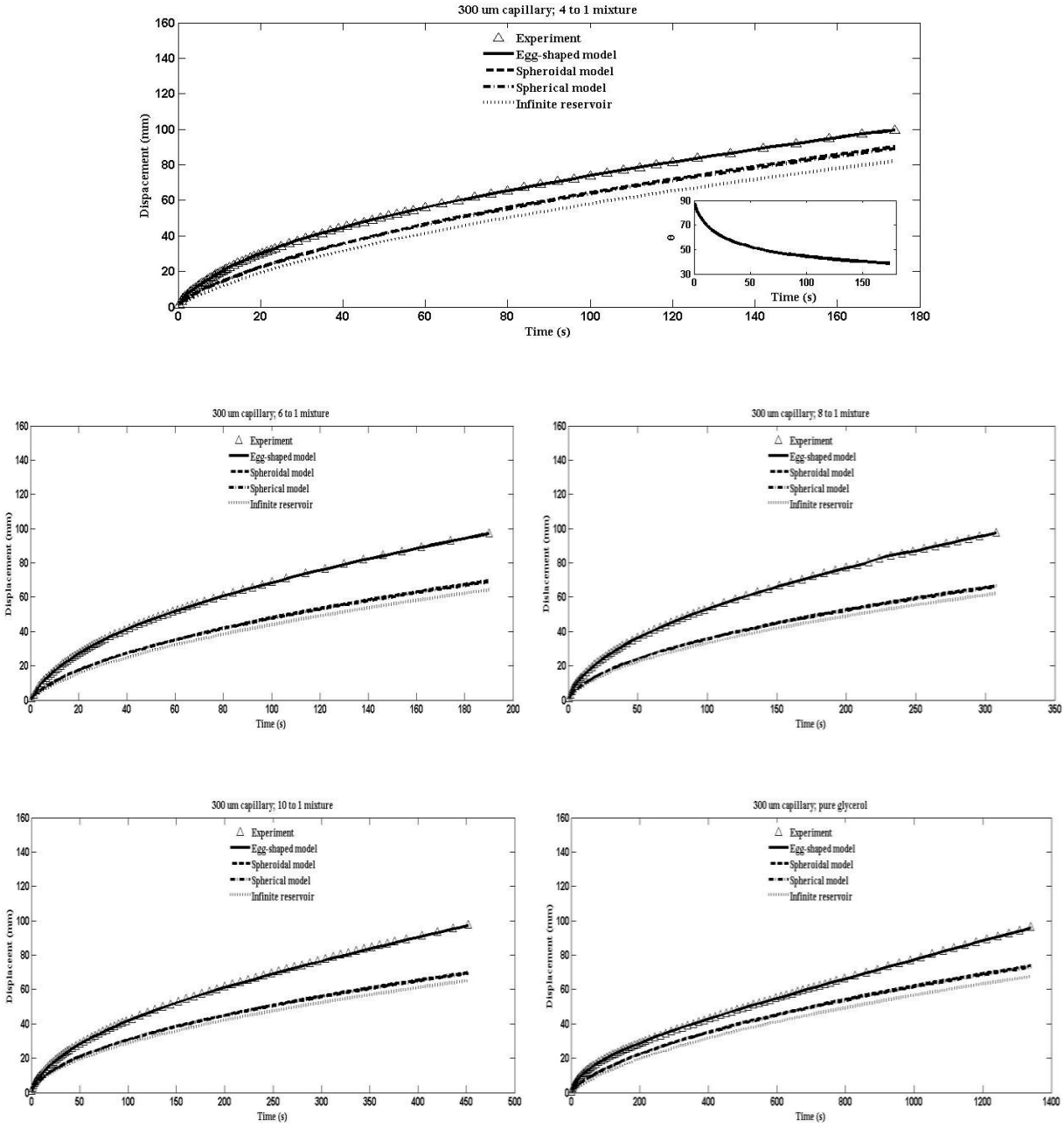

Figure 4-12: Comparison between experiment and numerical calculations of spherical, spheroidal and egg-shaped models, and surface tension driven flow from an infinite reservoir in 300 µm capillary.

ATTENTION: The Singapore Copyright Act applies to the use of this document. Nanyang Technological University Library

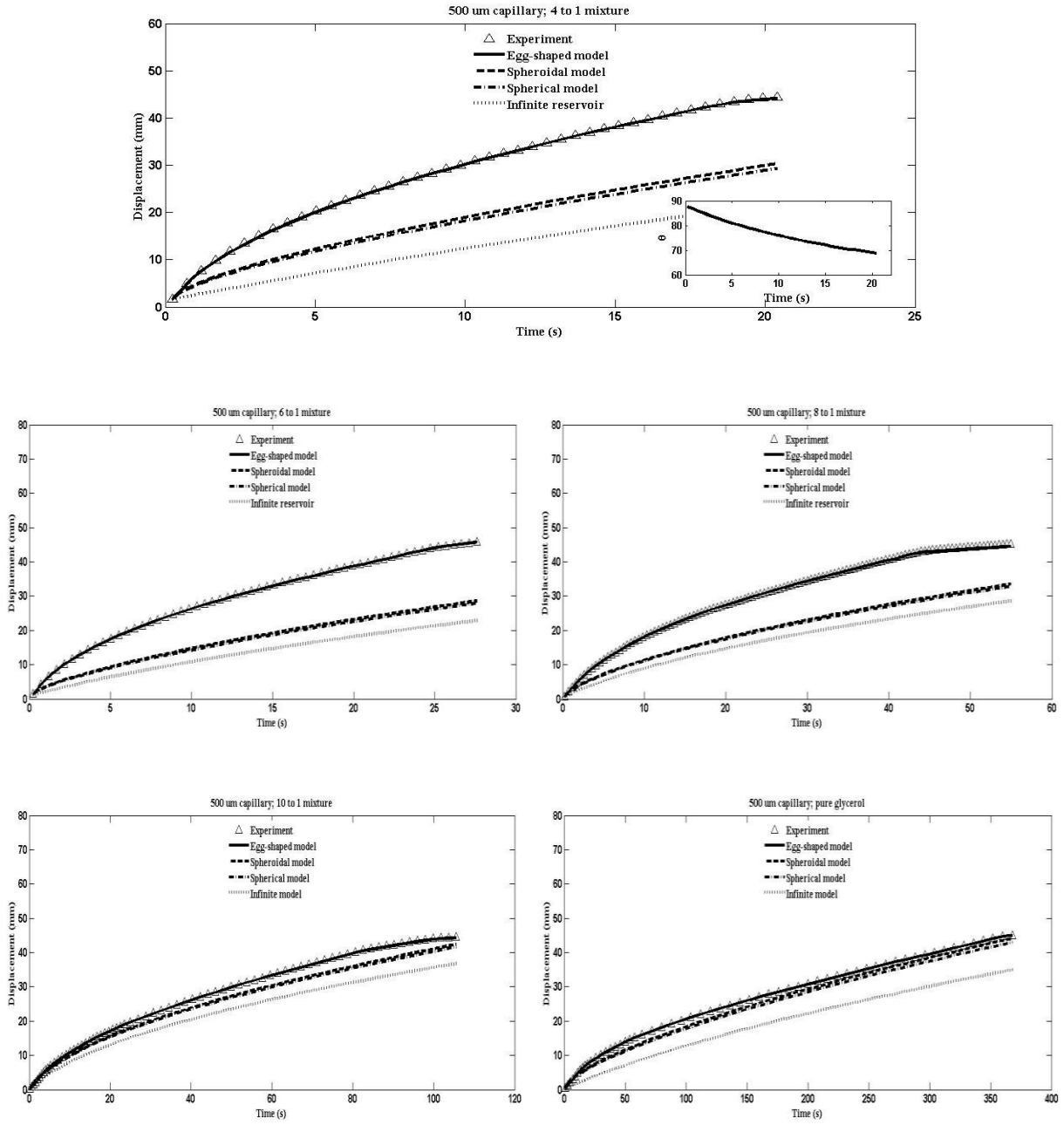

Figure 4-13: Comparison between experiment and numerical calculations of spherical, spheroidal and egg-shaped models, and surface tension driven flow from an infinite reservoir in 500 µm capillary.

ATTENTION: The Singapore Copyright Act applies to the use of this document. Nanyang Technological University Library

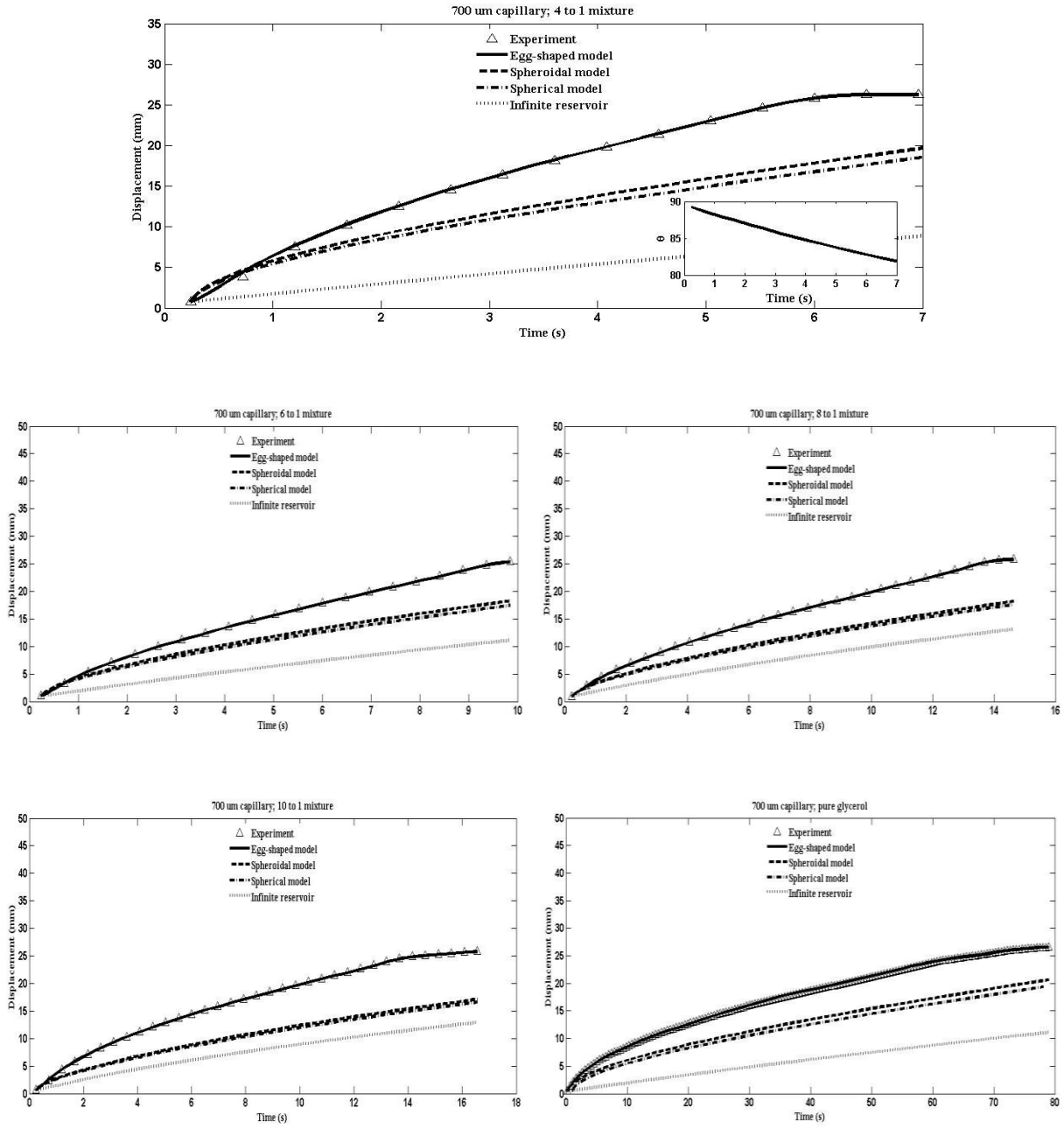

Figure 4-14: Comparison between experiment and numerical calculations of spherical, spheroidal and egg-shaped models, and surface tension driven flow from an infinite reservoir in 700 µm capillary.

ATTENTION: The Singapore Copyright Act applies to the use of this document. Nanyang Technological University Library

Chapter 5: Characterization of surface tension and contact angle of TiO_2 – DI water nanofluids

1. Introduction

In continuance of Chapters 3 and 4, it is intended to study wetting properties, i.e. surface tension and contact angle of nanofluids (this chapter), and spreading and capillarity of nanofluids (next chapter). A potential application of nanofluids is the cooling of microelectronic devices. Underfill flow process in flip chip technology is another important application in MEMS in which an underfill material (a nanofluid) is driven by surface tension into the chip-to-substrate stands off created by an array of solder bumps. The nanofluid will help to minimize thermal stresses in such systems. Other applications include spin coating in MEMS and detergent systems. However, few studies have been reported on wetting properties of nanofluids. Thus, characterization of the surface tension and contact angle of nanofluids, and understanding the physics involved in nanofluid spreading and capillarity are essential for flow control purposes in these applications.

The objective of this chapter is to investigate the effect of nanoparticles on surface tension and contact angle of nanofluids. Experiments were carried out for TiO_2 nanoparticles (15 nm) – DI water nanofluids of various nanoparticle volume concentrations ranging from 0.05% to 2%. With the FTA200 system, surface tension of these nanofluids was measured by using the pendant droplet method, and equilibrium contact angle was determined by using the sessile droplets on a borosilicate glass slide.

ATTENTION: The Singapore Copyright Act applies to the use of this document. Nanyang Technological University Library

2. Preparation of TiO_2 – DI water nanofluids

The choice of TiO_2 nanoparticles for the purpose of these experiments is that these particles are cheap and commercially available. They have simple spherical geometry Vafaei et al. (2006) studied contact angle of bismuth telluride nanoparticles and Sefiane et al. (2008) studied contact angle of aluminum nanoparticles. Nevertheless, due to agglomeration and clustering of nanoparticles, nanofluids cannot be prepared by simply dispersing nanoparticles in the carrier liquids. Proper mixing, homogenizing and stabilizing are essential steps to be taken. Characteristics of a well-dispersed nanofluid are homogeneity, stability and durability. No chemical change of the base liquid must also be assured. There are mainly two techniques to prepare nanofluids:

1. Single-step technique in which evaporation (of a source material under vacuum condition) and condensation (the inert gas condensation technique) and dispersion are used in a single step to produce nanofluids.

2. Two-step technique in which available commercial nanoparticles (which are produced in large scales by the evaporation and condensation technique) are dispersed and homogenized in a base liquid.

Despite the advantage of the single-step technique in reduced agglomeration and thus increased stability, the two-step method is more common, because commercial nanoparticles are produced cheaply in large amounts and can be easily dispersed in various liquids. Various techniques are then essential to reduction of the agglomeration of particles. These methods are ultrasonication, control of pH and addition of surfactants. These methods alter the surface properties of the suspended particles and thus decrease the tendency to form particle clusters. As compared to the single-step method, the two-step technique works well for oxide nanoparticles, while it is less successful with metallic particles (see ref. [130]).

ATTENTION: The Singapore Copyright Act applies to the use of this document. Nanyang Technological University Library

In the present project, the two-step method was used to prepare to-be-tested nanofluids. 15 nm TiO_2 nanoparticles were purchased from Nanostructured and Amorphous Materials Inc., and mixed with DI water. Various nanoparticle concentrations ranging from 0.05% to 2% (by volume) were used in experiment. The solutions were then added with oleic acid surfactant (purchased from Riedel-de Haën). It is noted that the selection of surfactants should depend mainly on the properties of the solutions and particles. Oleic acid surfactant has been reported to be capable of stabilizing TiO_2 – DI water nanofluids (see ref. [131]). Since oleic acid is less dense than DI water, drops of oleic acid were observable on the surface of the solution after addition; thus, the solution needed to be stirred for 8 hours by using magnetic stirrer till no droplets was observable at the surface. Finally, in order to break particle clusters and agglomerations, the nanosolution was sonicated for 100 minutes using Sonicator 3000 (20 kHz and 80 kW, MISONIX). A 5-sec pulsation and 20-sec off were used as the sonication program. With this program and employing ice bath, the temperature of the nanofluid was maintained at 25^{o}C during the sonication process.

Stability of nanosuspensions

Homogeneity and well dispersion of nanoparticles in the base liquid are important factors affecting thermophysical properties as well as stability of the solution. Thus, different methods or combinations of them are usually employed to disperse the particles properly; these methods are sonication, addition of electrolytes and addition of surface acting agents. However, despite these efforts, the affinity to form clusters is so high that the nanofluids prepared by the two-step method are weakly stable, changing in properties even after minutes of sonication (see ref. [132]). Hence, it is necessary to ensure the relative stability and durability of the nanosuspensions prior to experiments.

ATTENTION: The Singapore Copyright Act applies to the use of this document. Nanyang Technological University Library

In order to ensure the stability and durability of these nanofluids, different sonication time intervals were explored. For this reason, in these experiments the solutions were sonicated over several time intervals from 50 min to 150 min and viscosity of the solution after each time interval was measured (see ref. [132]). With this method, a saturation sonication time[8] could be obtained, after which there was no more change in the viscosity of the solution. It is noted that both the viscosity and surface tension could be chosen as the reference thermophysical property to obtain the saturation sonication time; however, viscosity was preferred because of its lower sensitivity on experimental uncertainties. Figure 5-1 and Figure 5-2 show the viscosity as function of sonication period for 1% and 2% TiO_2 – DI water nanofluids, respectively. Obviously, a stable value of viscosity was obtained after 100 min and roughly after 50 min of sonication for 2% and 1 % concentration respectively. The period of 100 min was used as a criterion for other (more dilute) nanofluids.

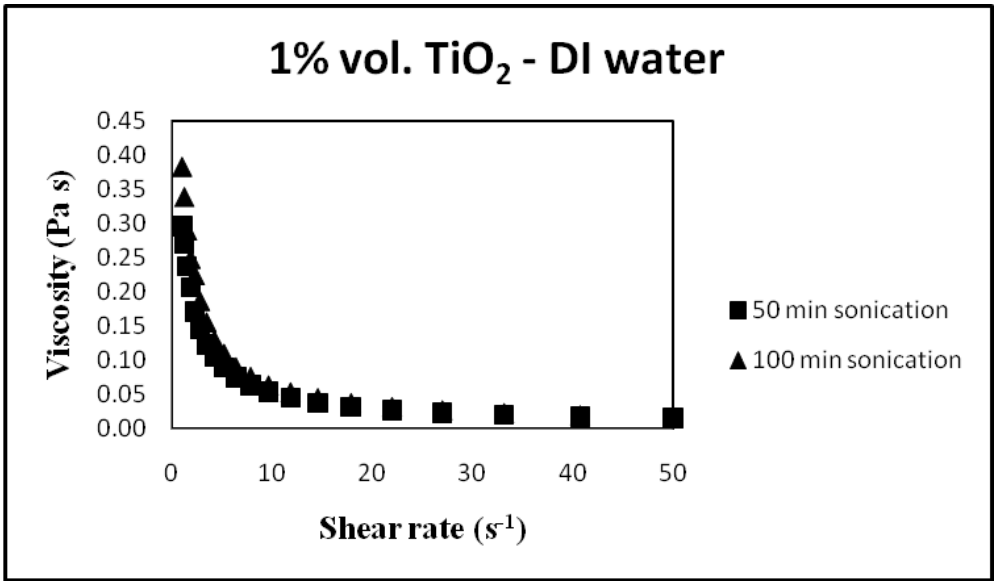

Figure 5-1: Viscosity saturation as function of sonication period for 1% vol. TiO_2 – DI water.

[8] Saturation sonication time refers to a sonication period after which there is no more change in a particular thermophysical property. In this work, viscosity was chosen as the reference thermophysical property.

ATTENTION: The Singapore Copyright Act applies to the use of this document. Nanyang Technological University Library

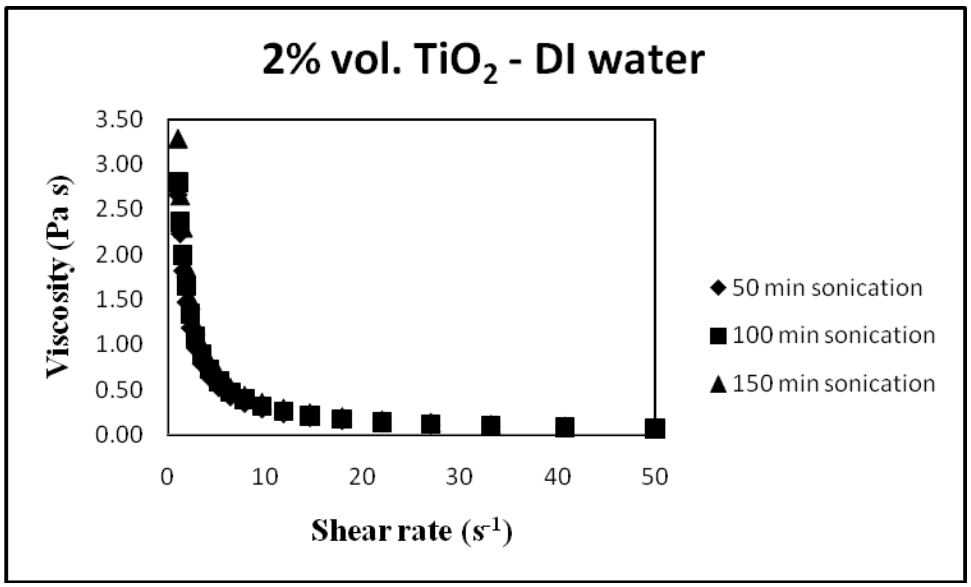

Figure 5-2: Viscosity saturation as function of sonication period for 2% vol. TiO_2 – DI water.

In order to monitor the dispersity, size and clustering of nanoparticles, transmission electron microscope (TEM) and particle size analyzer were used. TEM photographs show that the solution contains clusters of different sizes (levels) in addition to mono-dispersion of nearly-actual-size (15 nm) nanoparticles. This confirms that the addition of oleic acid surfactant and proper period of sonication are suitable for reducing cluster formation and lowering effective particle size. Spherical geometry of TiO_2 nanoparticles is also observed in the solution (see Figure 5-3). The particle clusters are mainly due to interparticle attractions and large particle density. The clusters increase the effective size of particles in the solution and have drastic effects on thermophysical properties of the solution.

ATTENTION: The Singapore Copyright Act applies to the use of this document. Nanyang Technological University Library

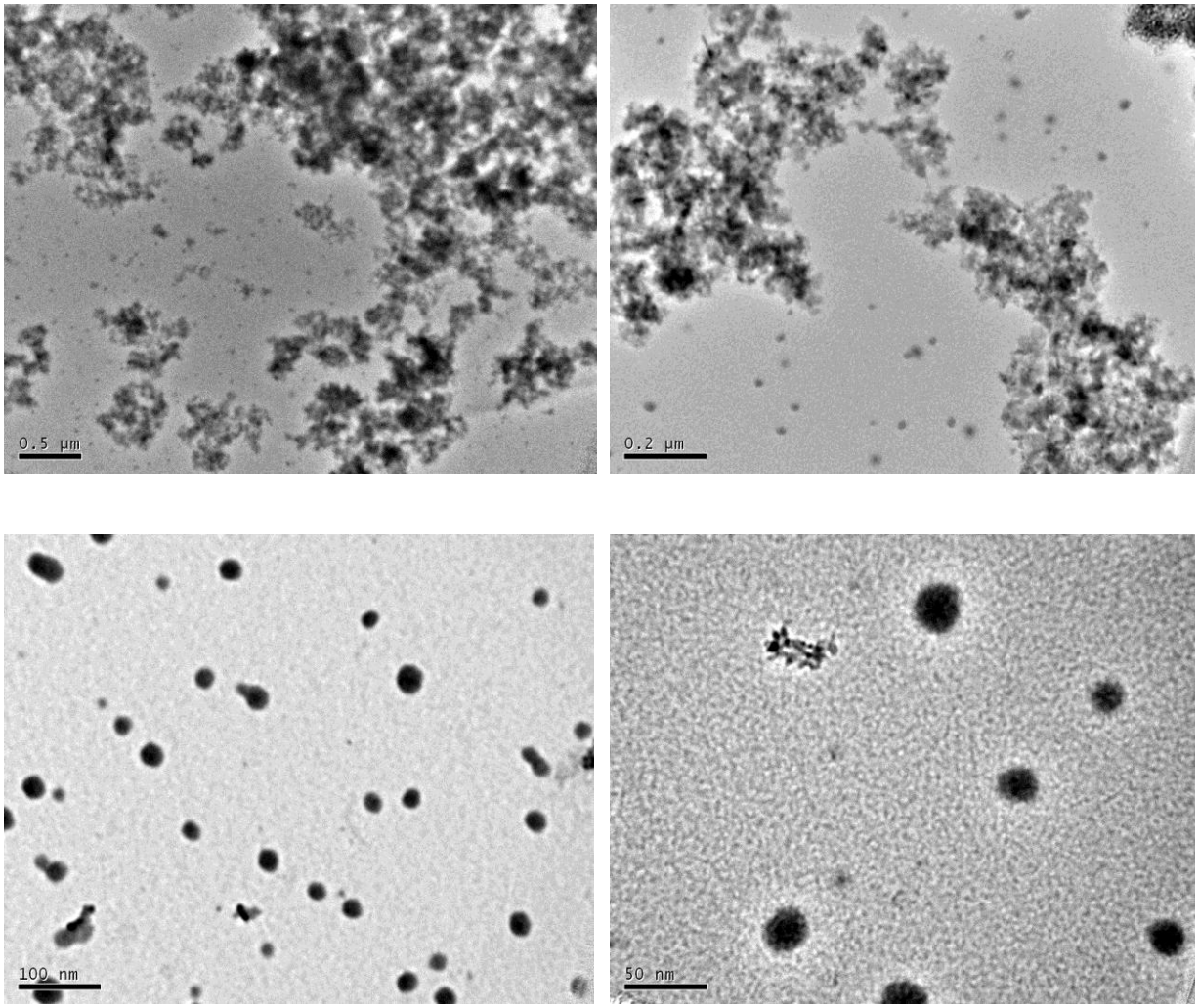

Figure 5-3: TEM photograph of 15 nm TiO_2 nanoparticles in DI water.

The particle size analyzer uses Dynamic Light Scattering (DLS) principle to measure the effective size of agglomerated particles in a Brownian suspension. When a laser beam is incident onto a particle, most of it is transmitted and a small amount is scattered. The intensity of the scattered light which is proportional to the size of the particle is auto-correlated to the following expression:

$$C(t) = Ae^{-2\Gamma t} + B, \tag{5.1}$$

ATTENTION: The Singapore Copyright Act applies to the use of this document. Nanyang Technological University Library

in which *A* and *B* are instrumental constants and Γ is the relaxation rate that is dependent on the effective (hydrodynamic) size of particles d_{eff}, and the square of the scattering vector size *q*:

$$\Gamma = \left[\frac{k_{\text{B}} T}{3\pi\eta_{\text{b}} d_{\text{eff}}} \right] q^2. \tag{5.2}$$

The term in brackets of equation (5.2) is based on Einstein's formula of Brownian diffusion. The scattering vector ($q = (4\pi n/\lambda_{\text{beam}})\sin(\theta/2)$) is a function of the index of refraction in water ($n \simeq 1.336$), the wavelength of the incident beam ($\lambda_{\text{beam}} = 671$ nm) and the scattering angle ($\theta = 90^{\text{o}}$). Table 5-1 shows the effective particle diameter of (actually) 15 nm TiO_2 particles in 0.05% vol. solution with oleic acid concentrations ranging 0 to 0.01% vol.

The surface charge of the nanoparticles was also measured using the zeta potential analyzer (ZetaPlus, Brookhaven Instruments Corporation). This equipment is used to measure zeta potential and the corresponding electrostatic repulsive forces between nanoparticles in a nanofluid (see Ref. [133]). The effects from the electrokinetic properties on thermal conductivity of nanofluids have been studied before (see Ref. [134]); however, studying the effect of surface charge on surface tension of nanofluids has not yet been addressed. The net charge on nanoparticle surface changes ion distribution in the regions near nanoparticle interface, increasing the concentration of counter ions. Thus, an electrical double layer is formed in the nearby region of the interface. This double layer consists of two sub-layers: an inner region in which ions bound relatively tightly to the surface, and an outer region where a balance of electrostatic forces and random thermal motion determines the ion distribution. The potential in the outer region decays with increasing distance from the surface and at sufficient distance; it reaches the bulk solution value (taken to be zero). The zeta potential is the value at the interface of the two-sub regions. Zeta potential is therefore a function of the

ATTENTION: The Singapore Copyright Act applies to the use of this document. Nanyang Technological University Library

surface charge of the particle, any adsorbed layer at the interface, and the nature and composition of the surrounding suspension medium. Based on Smoluchowski's formula, the zeta potential ζ has the following relation with the electrophoresis mobility U_e [135]:

$$U_e = \frac{\varepsilon}{\eta_b}\zeta \tag{5.3}$$

where ε $(=78.9\varepsilon_0)$ is the dielectric constant of the dispersion medium and ε_0 is the permittivity in vacuum environment. Table 5-1 shows the zeta potential of TiO_2 particles in 0.05% vol. solution for various surfactant concentrations ranging from 0 to 0.01% vol. Table 5-1 also shows that for higher surfactant concentrations, although the value of the effective diameter did not change in a systematic manner, the value of zeta potential increased with surfactant concentration. This means that for higher surfactant concentration these nanofluids are more stable; however, as will be shown later in this chapter, for higher values of surfactant concentration (more than 0.01%), the surface tension is reduced significantly, rendering the surface tension force to smaller values. This is indeed not of interest in these experiments where the surface tension force is the only driver force in the experiments. Finally it is noted that since for concentrations higher than 0.05% vol. nanoparticles, the nanofluid is opaque and unable to transmit light, no more than 0.05% vol. concentration was selected for the measurements of particle size and zeta potential. Three measurements were conducted for each test and an averaged value was taken.

ATTENTION: The Singapore Copyright Act applies to the use of this document. Nanyang Technological University Library

Table 5-1: Effective diameter and zeta potential of 15 nm TiO_2 particles in 0.05% vol. solution.

Surfactant vol. concentration	**0%**	**0.005%**	**0.01%**
d_{eff} **(nm)**	232.5	281	269
ζ **(mV)**	-21.61	-23.35	-25

3. Experimental investigation

Measurement of surface tension

Measurement of the surface tension of fluids can be carried out precisely by using the pendant droplet method. Surface tensions of various fluids like polymers, liquid crystals, and other low-molar-mass liquids were measured using this method (see Refs. [136, 137]). In this method, precautions like cleanliness of syringe, needle and needle tip are very important. Contaminants such as dust and oil can lower the surface energy at the tip, resulting in inaccurate data. The washing procedure is the same as proposed in *Sec.* Materials and methods, in Chapter 3. The FTA200 system (see Figure 3-1) is equipped with a syringe pump which allows pumping out (or pumping in) of liquids with rates ranging 1.3 to 126.8 μL s^{-1}. For the present experiments, nanofluids were initially pumped out of the syringe at a very small rate namely 1.3 μL s^{-1} to minimize inertia effects. Small pumping velocity is of extreme importance due to its effect on the geometry of the droplet and consequently on the value of the surface tension measured by the pendant droplet method. The volume of the pendant

ATTENTION: The Singapore Copyright Act applies to the use of this document. Nanyang Technological University Library

droplet should also be kept at its maximum so that the weight of the droplet is always balanced by the surface tension force failing which an inaccuracy in the surface tension measurement may occur. The maximum pendant droplet volume changes for different fluids due to the difference in their surface tension and density; thus the proper value should be obtained by trial and error. Due to evaporation effects, measurements should also be performed right after the pendant droplet reaches to its maximum volume. The maximum volume for these nanofluids was roughly 10 μl (see Figure 5-4). In the FTA200 system, the surface tension is determined on the basis of the Laplace equation (equation (2.1)):

$$\Delta p = \gamma\left(\frac{1}{R_1}+\frac{1}{R_2}\right) \tag{5.4}$$

where Δp is the (interfacial) pressure difference across any arbitrary point on the interface, and R_1 and R_2 are the two radii of curvature at that point measured form the profile of the droplet. Δp can be determined using the gravity and density difference across the interface as follows:

$$\Delta p = \Delta\rho g h \tag{5.5}$$

where $\Delta\rho$ is the density difference across the interface, and h is the height of droplet measured from the apex. Thus, the only unknown variable is the surface tension γ, which can be obtained by curve-fitting the captured droplet image with the droplet profile determined by the Laplace equation.

ATTENTION: The Singapore Copyright Act applies to the use of this document. Nanyang Technological University Library

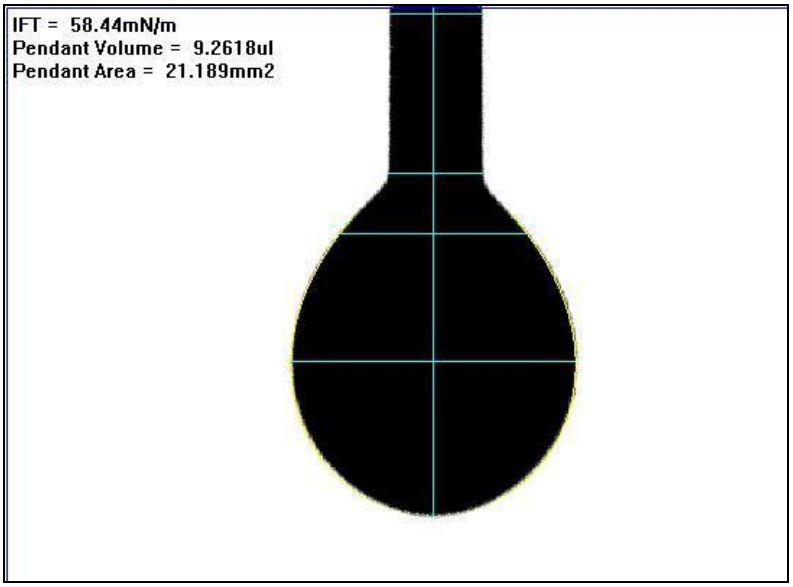

Figure 5-4: Pendant droplet image analyzed by the FTA200 software to measure surface tension.

Measurement of contact angle

In these experiments, photographs of sessile droplets of nanofluids were used to measure the contact angle [138]. These sessile droplets were cast on borosilicate glass slides (see Figure 5-5). The nanofluid was initially pumped out of the syringe at a very small rate (e.g., 1 μL s^{-1}) and detached from syringe needle tip as soon as it touched the surface of the solid. Pre-cleaned dry slides were used immediately after unpacking. Essentially, we found that if the glass slides are washed, during the drying process (with pressurized air or heating in oven which were the methods that we used) they are prone to contamination (e.g. with tissue fibers or oil) due to solid surface energy. The sessile droplet volume was maintained at 6 μl. With this volume, the sessile droplet formed a spherical geometry with the radius of its equivalent sphere being smaller than the capillary length $L_C = \sqrt{\gamma/\rho g}$. Thus in the FTA200 system, which is capable of using several fits (such as spherical fit, non-spherical fit, and Laplace fit) to the captured sessile droplet geometry in order to measure its contact angle, the spherical fit was used in these experiments. The non-spherical fit results in different right and left angles for the sessile droplet. It was observed that for the dense solution, namely 2% vol., while

ATTENTION: The Singapore Copyright Act applies to the use of this document. Nanyang Technological University Library

casting over the surface of the solid, the sessile droplet deviates from a spherical geometry which could only be seen through the CCD camera. Thus for this concentration, the non-spherical fit was utilized and an average of left contact angle and right contact angle was reported as the equilibrium contact angle.

A very important consideration is the evaporation. Evaporation of the sessile droplet can drastically lower the value of the contact angle as compared to the actual wetting contact angle. For a sessile droplet of spherical cap, which has been spread on the solid surface, the base radius (r) and volume (V) are related to the contact angle (θ) by the following relationship:

$$r^3 = \left(\frac{3V}{\pi} \frac{\sin^3\theta}{2 - 3\cos\theta + \cos^3\theta} \right) \tag{5.6}$$

Using this equation, it is possible to obtain the variation in droplet volume (ΔV) with respect to its volume at equilibrium situation (V^0) as a function of equilibrium contact angle (θ^0) as follows:

$$\frac{dV}{V^0} = \left(\frac{3 - 6\cos\theta^0 + 3\cos^2\theta^0}{2 - 3\cos\theta^0 + \cos^3\theta^0} \right) d\theta \tag{5.7}$$

In order to disregard evaporation effect, a video was captured from the droplet spreading on solid surface and the equilibrium contact angle was measured at equilibrium situation (i.e. no more change in base line radius) when the change in droplet volume was less than 5% from its initial volume. This results in less than 5% error ($d\theta/\theta^0$) in the measurement of the equilibrium contact angle.

ATTENTION: The Singapore Copyright Act applies to the use of this document. Nanyang Technological University Library

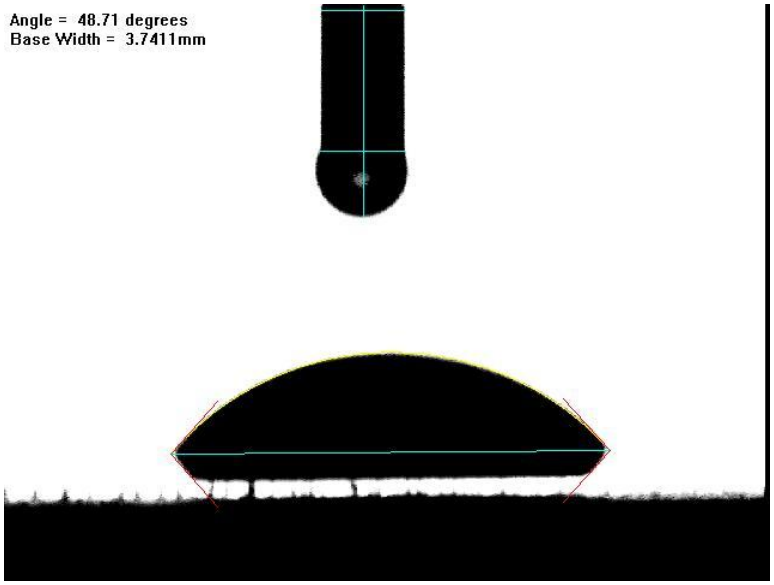

Figure 5-5: Sessile droplet image analyzed by the FTA200 software to measure equilibrium contact angle.

4. Results and discussion

Figure 5-6 shows the variation of the surface tension of TiO2-DI water nanofluids with nanoparticle concentration. At higher concentrations, the surface tension is lower and the reduction of surface tension from the relatively dilute solution (0.05% vol.) to the relatively dense solution (2% vol.) is 8.9 mN/m. In addition, the surface tension of pure DI water is 72.8 mN/m which is 9.6 mN/m higher than the surface tension of 0.05% vol. nanofluid. It has been shown that the surface tension is related to the cohesive energy (see Refs. [139-141]). The reduction in surface tension of nanofluids is attributed to the reduction in cohesive energy at liquid-air interface when nano-sized particles are added to the base liquid. In fact, this is related to the Brownian motion of nanoparticles within the liquid. The Brownian motion can disperse the nanoparticles located at the liquid-air interface to new orientation with lower level of the total free energy of interface. Consequently, this will reduce the surface tension (see Ref. [142]).

ATTENTION: The Singapore Copyright Act applies to the use of this document. Nanyang Technological University Library

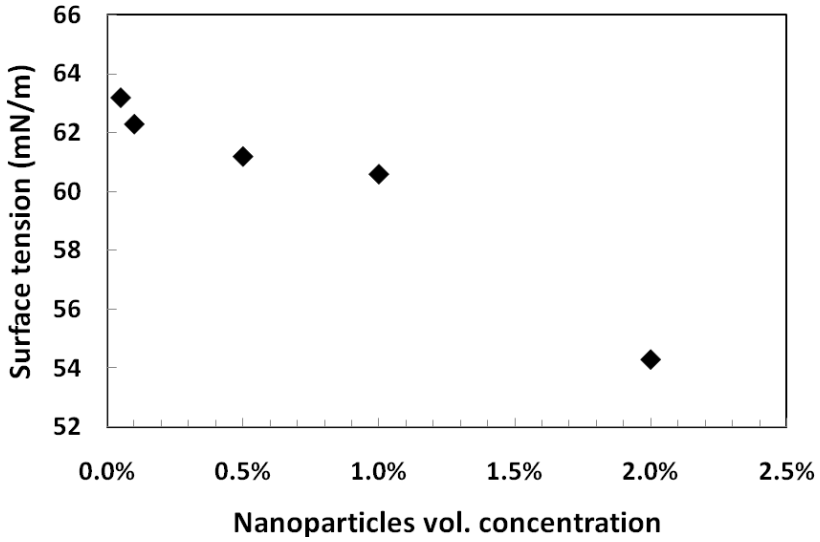

Figure 5-6: Variation of the surface tension of TiO_2 - DI water nanofluids with nanoparticles vol. concentration.

The presence of surfactant molecules can also reduce the surface tension. Surfactant's dual-nature molecules with a hydrophilic head and a hydrophobic tail always locate themselves at the liquid-air interface (with the head towards the water molecules and the tail towards the air molecules) in such a way to minimize the interfacial energy (see Ref. [143]). In order to examine this effect, surface tension measurements were also performed for two types of nanofluids, (i) one without the addition, and (ii) the other with addition of 0.05% vol. of oleic acid surfactant. Table 5-2 and Figure 5-7 show that the surface tension is a strong function of surfactant concentration. It was found that the dependency of surface tension on nanoparticle concentration is weak comparing to the dependency on surfactant concentration. It is reported that nanoparticles can also function as surfactant molecules because nanoparticles can be absorbed onto the interface to cause a reduction in the surface tension (see Ref. [143]).

Finally based on these experimental results, 0.01% vol. concentration of oleic acid surfactant was added for the measurements of equilibrium contact angle (the next section), and performing spreading and capillarity experiments (the next chapter). This is because for this value of surfactant concentration, the nanofluids are stable for almost one day. Although a

ATTENTION: The Singapore Copyright Act applies to the use of this document. Nanyang Technological University Library

higher surfactant concentration (e.g., 0.05%) results in solutions of higher stability and durability, the resulting surface tensions are smaller than 0.01% vol. concentration of oleic acid (see Table 5-2). Indeed, this is not desirable in the capillary flow experiments where the surface tension force is the only driver force.

Table 5-2: Surface tension of TiO_2 – DI water nanofluids for various surfactant concentrations.

Surfactant vol. concentration	**Nanoparticle vol. concentration**				
	0.05%	**0.1%**	**0.5%**	**1%**	**2%**
	Surface tension (mN/m)				
0%	71	70.8	70.3	69.8	65.9
0.01%	63.2	62.3	61.2	60.6	54.3
0.05%	50.3	50.1	49.9	49.6	49

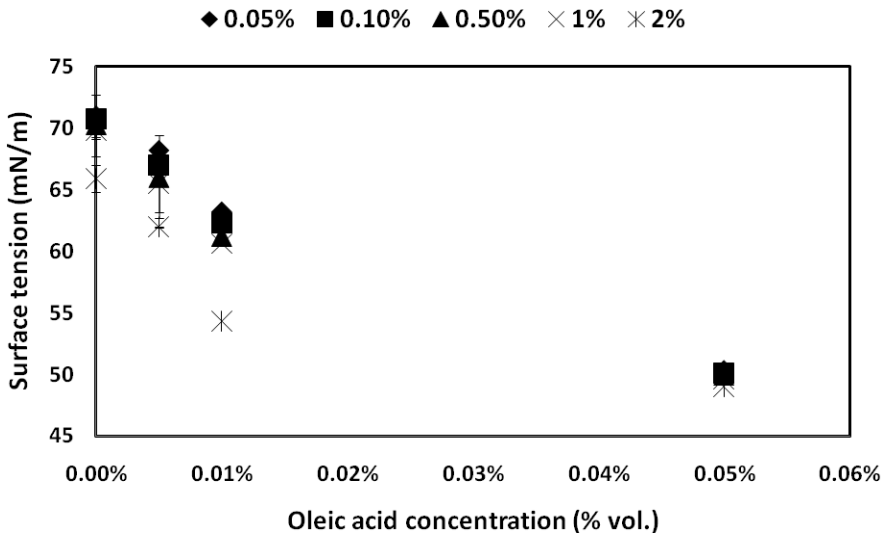

Figure 5-7: Surface tension of TiO_2 - DI water nanofluids.

Figure 5-8 shows the variation of the equilibrium contact angle of TiO_2 – DI water nanofluids with nanoparticle concentration. It is shown that the equilibrium contact angle increases with nanoparticle concentration. Similar trend was partially observed in contact angles

ATTENTION: The Singapore Copyright Act applies to the use of this document. Nanyang Technological University Library

measurements for the bismuth telluride - DI water nanofluids on glass and silicon substrates by Vafaei et al. in 2006 and for the aluminum - ethanol nanofluids on Teflon-AF coated substrates by Sefiane et al. in 2008. In order to provide a better understanding of the observed phenomena, it is necessary to consider the underlying mechanisms responsible for the shape and contact angle of droplets on solid surface. When a small droplet is in contact with a solid surface, each of the three solid-liquid, solid-vapor (or gas), and liquid-vapor interfaces has a certain amount of energy called interfacial energy far from the three-phase contact line, γ_{sl}, γ_{sv} and γ, respectively. Near the contact line, the energy structure is more complex and depends on the various types of the solid-liquid, liquid-particle and solid-particle interactions [36]. Conventionally (Young's equation (2.2)), the value of the contact angle at the equilibrium situations (θ^0) is related to the far field interfacial energies without taking into consideration of the physics involved in the region near the contact line; it follows that:

$$\gamma \cos\theta^0 = \gamma_{sv} - \gamma_{sl} \tag{5.8}$$

In the presence of nanoparticles, the contact angle should be related to the stability of thin films containing nanoparticles [82], which is related to the surface forces between surfaces encapsulating the thin film and structural and depletion effects resulting from the ordering of nanoparticles within the film [26]. When a nanofluid wets a solid surface, these surface forces together with structural and depletion effects result in a so-called disjoining pressure within the thin film adjacent to the bulk nanofluid. In this region, the nanofluid changes from a thick fluid film to a microscopic thin film at which the disjoining pressure dominates the behavior of the fluid film, thus affecting the equilibrium shape and contact angle (θ^0) of the droplet on solid surface. The disjoining pressure is expressed as follows [86]:

$$\Pi(H) = \Pi_m(H) + \Pi_e(H) + \Pi_s(H) \tag{5.9}$$

ATTENTION: The Singapore Copyright Act applies to the use of this document. Nanyang Technological University Library

where $\prod_m$, $\prod_e$ and $\prod_s$ are the van der Waals, electrostatic, and structural and depletion interactions, respectively, and H is the liquid film thickness. The van der Waals and electrostatic components have been well defined in the DLVO theory [144]. The structural and depletion component are also defined in Trokhymchuk et al. (2001) [82]. The disjoining pressure results in an excess energy in the film (film interaction energy) as follows:

$$W(H) = \int_{\infty}^{H} \prod(H)dh \tag{5.10}$$

This film energy contributes to the spreading in the same manner as the interfacial tension energies do. Hence, two subsequent steps are considered in the spreading of nanofluid droplets. First, due to the imbalance of the three interfacial tension energies, the contact line moves and the contact angle decreases. A thin nanofluid wedge then forms at the proximity of the three-phase contact line, which confines patterned nanoparticles in the wedge height that ranges from one nanoparticle diameter to tens nanoparticle diameter. This results in additional pressure, which facilitates the spreading of the nanofluid if the disjoining pressure is positive. Higher particle volume fractions increase the disjoining pressure and thus enhance the spreading behavior of nanofluids, resulting in smaller equilibrium contact angles [82]. However, our experimental results show disagreement to this theory. This suggests the existence of other mechanisms controlling the spreading and equilibrium shape and contact angle of nanofluid droplets. Finally, based on FTA200 specification (which was also examined prior to our experiments) the uncertainty in contact angle measurement due to standard deviation is less than 1 degree. This is however less than the error associated with each contact angle measurement in our experiments being about 2 degrees. The averaged contact angle values as reported in Table 5-3 and shown Figure 5-8 are almost beyond the range of experimental uncertainty.

ATTENTION: The Singapore Copyright Act applies to the use of this document. Nanyang Technological University Library

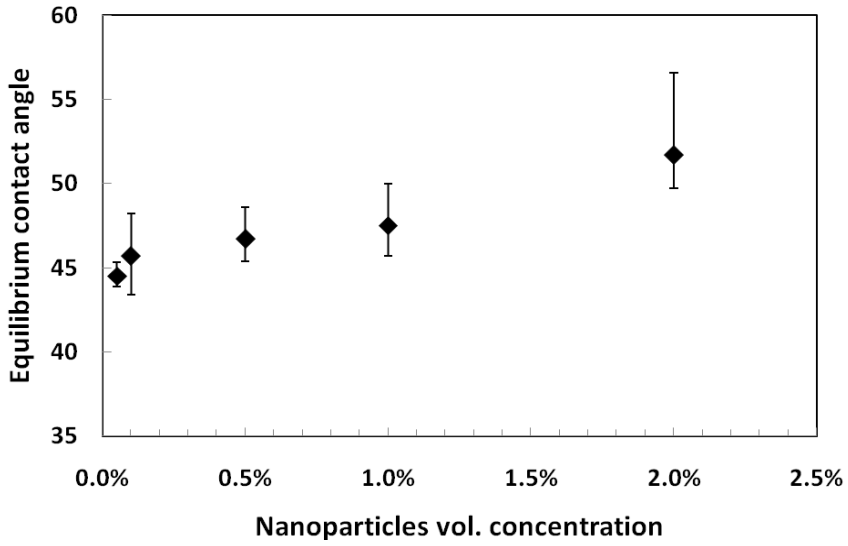

Figure 5-8: Variation of the equilibrium contact angle of TiO2 - DI water nanofluids with nanoparticles vol. concentration.

The experiments of Vafaei et al. [85] showed that the smaller nanoparticles have stronger effects on decreasing the contact angle. This indicates that larger nanoparticles existing in the wedge film exhibit reduced degrees of enhanced wetting. In our present experiments, agglomeration and clustering of nanoparticles, which result in larger averaged (effective) particle size, were inevitable, although rigorous mixing and homogenizing of nanofluids was performed to minimize the formation of clusters. In fact the average nanoparticle size for the dilute solution 0.05% vol. measured by using Particle Size Analyzer was about 250 nm (see Table 5-1). The same measurement for higher concentrations of nanoparticles was impossible due to the instrument limitations. It is likely that much more agglomerations have occurred in nanofluids of higher concentrations as there are more particle-particle interactions due to the decreased average distance between the nanoparticles in the bulk nanofluid. Thus, the effective nanoparticle size for the higher concentration nanofluids can be larger, and the number of nanoparticles in the wedge film can be lower. In line with Vafaei's et al. findings, this suggests reduced degrees of enhanced wetting due to the smaller nanoparticle effects at the wedge film for the higher concentration nanofluids (i.e. higher equilibrium contact angles).

ATTENTION: The Singapore Copyright Act applies to the use of this document. Nanyang Technological University Library

Finally, adsorption of nanoparticles to the solid surface can result in surface modification and pinning of contact line to the new adsorption sites on solid surface. Based on the molecular kinetics theory of Blake and De Coninck [44] liquid advancement on solid surface is a process of successive attachment of liquid molecules to the successive adsorption sites on solid surface in a desired direction. Recent experiments have shown that this theory is accurate in predicting experimental contact angles (see Ref. [145]). Nanoparticles may be adsorbed to these sites such that they not only change the solid-fluid interfacial characteristics, but also pin the contact line motion (see Ref. [146, 147]). With regard to equation (5.8), γ_{sv} is a constant (independent of nanoparticle concentration) and γ is shown to be a weak function of nanoparticles concentration. Thus, the only term that can change with respect to nanoparticles concentration is the solid-liquid interfacial tension γ_{sl}. Table 5-3 shows the variation of γ_{sl} (while keeping γ_{sv} as a constant) with respect to nanoparticles vol. concentration. This suggests that nanoparticles are adsorbed onto the solid surface, especially in the wedge film abutting the bulk nanofluid. In fact, adsorbed nanoparticles change the solid-liquid interfacial tension, also roughen the solid surface to result in pinning of the contact line. The effect is, however, more prominent for higher particle concentrations, leading to higher contact angles.

ATTENTION: The Singapore Copyright Act applies to the use of this document. Nanyang Technological University Library

Table 5-3: Variation in γ_{sl} with respect to nanoparticles concentration.

Nanoparticle concentration	**surface tension** (mN/m)	**contact angle** °	$\gamma_{SV} - \gamma_{SL} = \gamma_{LV} \cos\theta^0$
0.05%	63.2	44.5	45.1
0.10%	62.3	45.7	43.5
0.50%	61.2	46.7	42.0
1%	60.6	47.5	40.9
2%	54.3	51.7	33.7

ATTENTION: The Singapore Copyright Act applies to the use of this document. Nanyang Technological University Library

Chapter 6: Spreading and capillarity of TiO_2 – DI water nanofluids

1. Introduction

Many industrial operations such as spin coating, painting and lubrication are based on spreading of fluids over solid surfaces. The fluid may be a simple liquid (as in Refs. [148-150]) or a complex fluid such as a paint, an ink or a dye (as in Refs. [151, 152]). In this regard, carrier liquids containing nano-sized particles, i.e. nanofluids, are very important in applications such as heat transfer and fluid mechanics. For many years, the physics involved in surface tension driven flow of simple liquids has received considerable attention and important physical factors influencing such flows have been clarified for a long time (see Refs. [36, 153-156]). For nanofluids, however, there is a lack of consistent study on wetting dynamics, spreading and capillarity.

In capillary action of nanofluids, the driving energy is a combination of the out of equilibrium surface tension energy ($\gamma_n\left(\cos\theta^0-\cos\theta\right)$), and film interaction energy ($W\left(H\right)$) [83, 84, 86]. The driving energy is however balanced by various dissipative mechanisms acting on the microscopic region near the contact line. De Gennes (1985) [36] performed the first rigorous study on the types of dissipative mechanisms and defined three regions where these dissipations occur. Local dissipation ($T\sum_l$) which occurs in the proximity of the three-phase contact line due to adhesive and cohesive interactions between solid molecules and liquid molecules, precursor-film viscous dissipation ($T\sum_f$) which occurs in a region of about 10 nm from the contact line, and wedge-film viscous dissipation ($T\Sigma_W$) which occurs behind the

ATTENTION: The Singapore Copyright Act applies to the use of this document. Nanyang Technological University Library

precursor film due to lubricating and rolling flow patterns in the wedge film. Although there is no quantitative experimental law for the flow patterns in the precursor film and thus is usually ignored [36], broadly speaking, there are two theories for the local and wedge film dissipations, the molecular kinetic theory and the hydrodynamic theory, respectively.

The objective of this chapter is to investigate the effect of nanoparticle concentration on the spreading and capillarity of nanofluids. For the spreading part, TiO_2 (15 nm) – DI water nanofluids of various nanoparticle volume concentrations ranging from 0.05% to 2% were used. For the capillary flow part, these nanofluids were used in 1% and 2% concentration with two different configurations: finite reservoir (pendant droplet) and infinite reservoir (a beaker with an inlet arm). With the FTA200 system, dynamic contact angle and meniscus motion were monitored. In the theoretical analysis, Lagrange's equation of motion incorporated with Rayleigh's dissipation functions were used to derive the drag forces. Also reported in this chapter are the viscosities of these nanofluids. Viscosity data are essential for any experiment; the data will then be used in the theory. For these nanofluids there is no consistent data on the viscosity at low shear rates, namely less than 50 s^{-1}.

2. Experimental investigation

Measurement of viscosity

The viscosity of TiO_2 - DI water nanofluids was measured with a controlled low shear rate rheometer (Contraves, Low Shear 40). The equipment was set to measure the viscosity for shear rates ranging from 0 to 50 s^{-1}. This corresponds to flow in capillaries. Nanofluids having 0.005% to 2% vol. nanoparticle concentration with 0.001% vol. oleic acid surfactant concentration were produced in the laboratory. Viscosity measurements were carried out at 25.9^{o}C. Special care was taken to perform measurements right after the sonication to

ATTENTION: The Singapore Copyright Act applies to the use of this document. Nanyang Technological University Library

minimize sedimentation and clustering effects. If the sonicated nanofluid is left long before the experiments, clustering and sedimentation are inevitable, heavy sediments will gather at the bottom of the cup and the rheometer will measure a wrong viscosity.

Measurement of spreading

In experiments of equilibrium contact angle, which was reported in *Sec*. Measurement of contact angle, Chapter 5, a video was captured from sessile droplet while it was spreading over solid surface from initial contact to equilibrium position using the CCD camera attached to the FTA200 system (see Figure 6-1). This video was then used to measure the dynamic contact angle of these nanofluids during spreading. The spatial resolution was estimated to be about 50 μm on the basis of the focused area and the camera pixel size. The temporal resolution was estimated based on the frame speed of the CCD camera as 30 fps. For each experimental condition, three measurements were conducted, and an average was taken to represent the experimental data.

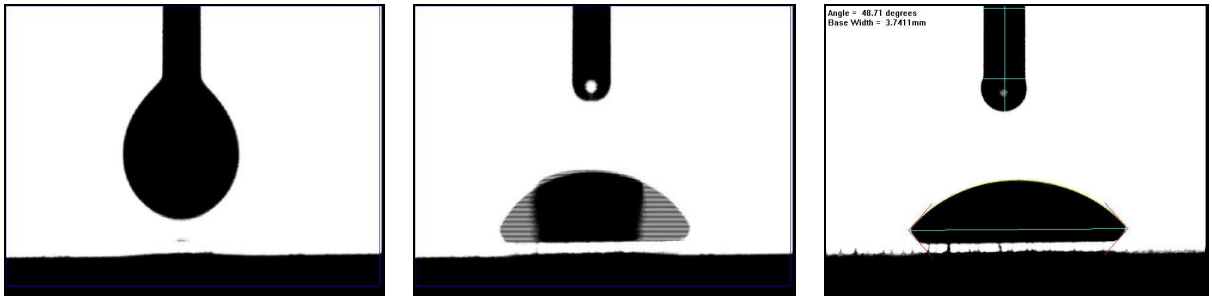

Figure 6-1: Droplet images taken by the CCD camera attached to FTA200 system. (Left) nanofluid is pumping out of the syringe needle, (Middle) onset of touch of the droplet with solid surface, and (Right) spreading over solid surface.

Measurement of capillary flow

Experiments on capillary flow behavior of nanofluids were done on the same set-up as previously used in experiments of Chapters 3 and 4. The only difference was in the filling fluid which was a nanofluid. Nanofluids with 1% and 2% vol. nanoparticle concentrations

ATTENTION: The Singapore Copyright Act applies to the use of this document. Nanyang Technological University Library

were used. Two different configurations were utilized to represent the reservoir: beaker with an inlet arm to represent an infinite reservoir, and pendant droplet to represent a finite reservoir. For infinite reservoir configuration, capillaries were aligned to the center of the inlet arm; the beaker was then filled with nanofluids up to height not exceeding the capillary centerline to minimize hydrostatic effects (see Figure 6-2). For finite reservoir configuration, droplets of roughly 10 ± 0.4 µl were pumped out of the syringe by the FTA200 system. Capillaries were aligned to the center of the pendant droplets (see Figure 6-3). It was observed that the capillary filling experiments with more dilute concentrations (namely less than 1% vol.) were unable to be performed because the CCD camera could not capture the very fast motion of the meniscus. Also, the translation stage was incapable of rapid side to side motion. Many efforts were made to capture the meniscus of less than 1% vol. concentration nanofluids but none of which were successful.

Figure 6-2: Capillary flow experiments in infinite reservoir configuration (beaker with an inlet arm). On the left side, figure shows 2% vol. nanofluid coming out of the inlet arm. Capillary is 500 µm diameter.

ATTENTION: The Singapore Copyright Act applies to the use of this document. Nanyang Technological University Library

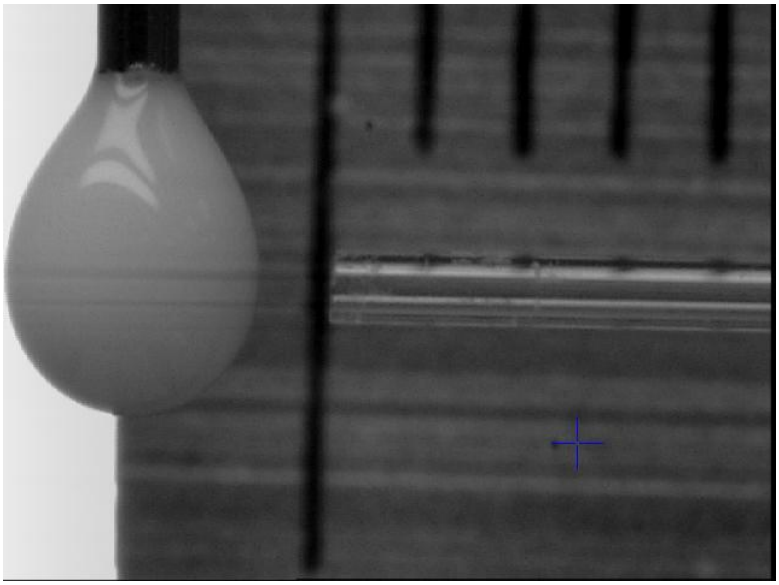

Figure 6-3: Capillary flow experiments in finite reservoir configuration (pendant droplet). Nanofluid is 2% vol. concentration. Capillary is 500 µm diameter.

3. Theoretical investigation

Empirical analysis of viscosity

It was observed (see Figure 6-13) that TiO_2 – DI water nanofluids of 0.5%, 1% and 2% vol. nanoparticle concentrations exhibit shear thinning viscosity (non-Newtonian behavior) in shear rates lower than 20 s^{-1}. At shear rates more than 20 s^{-1}, Newtonian behavior was observed for all solutions. For dilute solutions 0.1% and 0.05% vol. concentration weak non-Newtonian behavior (i.e. slight decrease in viscosity with shear rate) was also observed. Based on these observations and knowing (see Figure 6-13) that the viscosity of these nanofluids at shear rates beyond 20 s^{-1} is a constant function of nanoparticle concentration (ϕ) [93], it is assumed that two factors, i.e. shear thinning and nanoparticle volume concentration, influence the effective viscosity of these nanofluids. The total effect can be presented by a power-law relation as follows:

ATTENTION: The Singapore Copyright Act applies to the use of this document. Nanyang Technological University Library

$$\frac{\eta_n}{\eta_b} = F(\phi) K \dot{\gamma}^{n-1} \tag{6.1}$$

where η_b is the viscosity of DI water measured as 0.000927 Pa s at 25.9°C and $F(\phi)$ is function of nanoparticle volume concentration. $K\dot{\gamma}^{n-1}$ indicates power-law relation for the shear thinning viscosity of these nanofluids with *K* as the proportionality factor and *n* as the power-law index. In equation (6.1), *n* and *K* are empirical constants which are obtained by fitting this equation to experimental data.

Theory of spreading of nanofluids

When a fluid is advancing over a solid surface, two effects contribute to the total free energy of the system: surface tension energy and film energy. The former is due to the imbalance of the three interfacial tensions near the contact line. The latter is created by the various interparticular interactions within the thin film confined between the surface of the solid and the above air; the total effect is so-called as disjoining pressure [83]. While the disjoining pressure is attributed to three mechanisms, i.e. van der Waals force, electrostatic force, and structural and depletion force, it is the structural and depletion component which is reported to be long-range in nature (as compared to van der Waals and electrostatic forces) and thus is the dominant factor in the wetting phenomena [82].

In order to model the combined effect of surface tension energy and film interaction energy, the concept of molecular kinetics theory will be used [39]. Based on this theory, the rate of displacement of the contact line is equal to the net frequency of molecular jumps over (hypothetical) adsorption sites on the surface of solid ($K^+ - K^-$) multiplied by the average distance between these sites (λ), as follows:

$$U = \lambda\left(K^+ - K^-\right) \tag{6.2}$$

ATTENTION: The Singapore Copyright Act applies to the use of this document. Nanyang Technological University Library

At equilibrium, the frequency of forward motion (K^+) and frequency of backward motion (K^-) are equal to each other. The net equilibrium frequency of molecular displacements (K_W^0) based on Eyring's theory of absolute reaction rates can be obtained follows:

$$\begin{aligned} U &= \lambda\left(K^+ - K^-\right) \xrightarrow{\text{at equilibrium}} K^+ = K^- = K_W^0 \\ K_W^0 &= \left(\frac{k_B}{h}\right)\exp\left(\frac{-\Delta G_W^*}{Nk_BT}\right) \quad \left[= K^+ = K^-, \text{ at equilibrium}\right] \end{aligned} \tag{6.3}$$

where ΔG_W^* is the free energy of the system. The imbalance of interfacial tension energies changes ΔG_W^*; thus, the frequencies of fluid molecular motion on solid surface also change increasing in one direction (say forward) and decreasing in the opposite direction (backward). This leads to a net displacement in forward direction with a net (out of equilibrium) frequency of wetting (K_W) as follows:

$$\begin{aligned} K^{\pm} &= \left(\frac{k_B}{h}\right)\exp\left(\frac{-\Delta G_W^*}{Nk_BT} \pm \frac{\gamma\left(\cos\theta^0 - \cos\theta\right)}{2nk_BT}\right) \\ K_W &= K^+ - K^- = \left(\frac{2k_B}{h}\right)\exp\left(\frac{-\Delta G_W^*}{Nk_BT}\right)\sinh\left[\frac{\gamma\left(\cos\theta^0 - \cos\theta\right)}{2nk_BT}\right] \\ K_W &= 2K_W^0 \sinh\left[\frac{\gamma\left(\cos\theta^0 - \cos\theta\right)}{2nk_BT}\right] \end{aligned} \tag{6.4}$$

The basic molecular kinetic theory does not include the film interaction energy as the other source of alteration to the total free energy of the system.

Using the same concept and assuming that:

1. combined effect from the out of balance interfacial tension energies and film interaction energy contribute to the total free energy of system, and

ATTENTION: The Singapore Copyright Act applies to the use of this document. Nanyang Technological University Library

2. both the out of balance interfacial tension energies and film interaction energy increase the frequency of motion in forward direction,

it is possible to obtain the following frequencies of motion in forward and backward directions:

$$K^{\pm} = \left(\frac{k_B}{h}\right)\exp\left(\frac{-\Delta G_W^*}{Nk_BT} \pm \frac{\gamma\left(\cos\theta^0 - \cos\theta\right)}{2nk_BT} \pm \frac{\left[\int_H^\infty \Pi(h)dh\right]}{2nk_BT}\right) \tag{6.5}$$

where $\Pi(H)$ is the disjoining pressure and $\int_H^\infty \Pi(h)dh$ is the film interaction energy. Thus the net frequency of motion is as follows:

$$K_W = \left(\frac{2k_B}{h}\right)\exp\left(\frac{-\Delta G_W^*}{Nk_BT}\right)\sinh\left(\frac{1}{2nk_BT}\left[\gamma\left(\cos\theta^0 - \cos\theta\right) + \int_H^\infty \Pi(h)dh\right]\right) \tag{6.6}$$

Inserting this equation into equation (6.2) gives the following equation for the velocity of the contact line:

$$U = 2K_W^0\lambda\sinh\left(\frac{1}{2nk_BT}\left[\gamma\left(\cos\theta^0 - \cos\theta\right) + \int_H^\infty \Pi(h)dh\right]\right) \tag{6.7}$$

For small arguments of $\sinh$, this equation reduces to a linear form as follows:

$$U = \frac{K_W^0\lambda}{nk_BT}\left[\gamma\left(\cos\theta^0 - \cos\theta\right) + \int_H^\infty \Pi(h)dh\right] \tag{6.8}$$

where $nk_BT/K^0\lambda$ was previously termed as the coefficient of friction at the vicinity of the three-phase contact line with the same dimension as the bulk dynamic viscosity:

$$\zeta = \frac{nk_BT}{K_W^0\lambda} \tag{6.9}$$

ATTENTION: The Singapore Copyright Act applies to the use of this document. Nanyang Technological University Library

Inserting equation (6.9) into equation (6.8) and changing the equal sign to approximately equal sign in order to include other dissipation mechanisms such as wedge film dissipation, the following equation can be obtained:

$$\zeta U \approx \left[\gamma \left(\cos\theta^0 - \cos\theta \right) + \int_H^\infty \Pi(h) dh \right] \tag{6.10}$$

Structural and depletion components of the disjoining pressure

In Chapter 2, Sec. Disjoining pressure, it was stated that in 2001 Trokhymchuk et al. [82] developed equations (2.43) and (2.44) for the excess film energy and disjoining pressure. For the film thickness higher than one particle diameter, these equations consist two terms: an asymptotic form (first term on the right hand side) and a correction term (second term on the right hand side) as follows:

$$W(H) = W_0 \cos\left(\omega H + \phi_1\right) e^{-\kappa H} + W_1 e^{-\delta(H-d)} \quad \text{for } H \geq d \tag{6.11}$$

$$\Pi(H) = \Pi_0 \cos\left(\omega H + \varphi_2\right) e^{-\kappa H} + \Pi_1 e^{-\delta(H-d)} \quad \text{for } H \geq d \tag{6.12}$$

For film thickness smaller than one particle diameter, the following equations govern the excess film energy and the disjoining pressure:

$$W(h) = -P(d-h) - 2\sigma \quad \text{for } 0 < h < d \tag{6.13}$$

$$\Pi(h) = -P \quad \text{for } 0 < h < d \tag{6.14}$$

Equations (6.11) to (6.14) give good trends in comparison with the exact numerical calculations of the excess film interaction energy and disjoining pressure formulas (equations 8 and 9 in Ref. [82])[9].

[9] Derivations of the exact formulas are based on the inverse Laplace transform functions. These functions are very complicated and thus simpler forms, i.e. (6.11) and (6.12), are used in literature.

ATTENTION: The Singapore Copyright Act applies to the use of this document. Nanyang Technological University Library

Nevertheless, for particle volume fractions less than 0.04, δ becomes negative and the corrections terms $W_1 e^{-\delta(H-d)}$ in equation (6.11) and $\prod_1 e^{-\delta(H-d)}$ in equation (6.12) grow with no bound; this results in infinite film interaction energy ($W\left(H\right)$) and infinite disjoining pressure ($\prod(H)$) which are physically unreasonable. Typical comparisons of equations (6.11) and (6.12) excluding the correction terms (i.e. excluding the second terms on the right hand side of equations (6.11) and (6.12)) at particle volume fractions ranging 0.1 to 0.5 show that the asymptotic forms capture the film interaction energy and the disjoining pressure distributions for the majority of the film thickness, while minor discrepancies arise only at thickness equal to one particle diameter (see Figure 6-4 and Figure 6-5).

In the present study, volume fractions of nanoparticles range from 0.0005 to 0.02 are examined. As a result, for the calculation of the film interaction energy and disjoining pressure, asymptotic forms of equations (6.11) and (6.12) (without the correction terms) are used as follows:

$$W\left(H\right) = W_0 \cos\left(\omega H + \phi_1\right) e^{-\kappa H} \qquad \text{for } H \geq d \tag{6.15}$$

$$\prod(H) = \prod_0 \cos\left(\omega H + \varphi_2\right) e^{-\kappa H} \qquad \text{for } H \geq d \tag{6.16}$$

ATTENTION: The Singapore Copyright Act applies to the use of this document. Nanyang Technological University Library

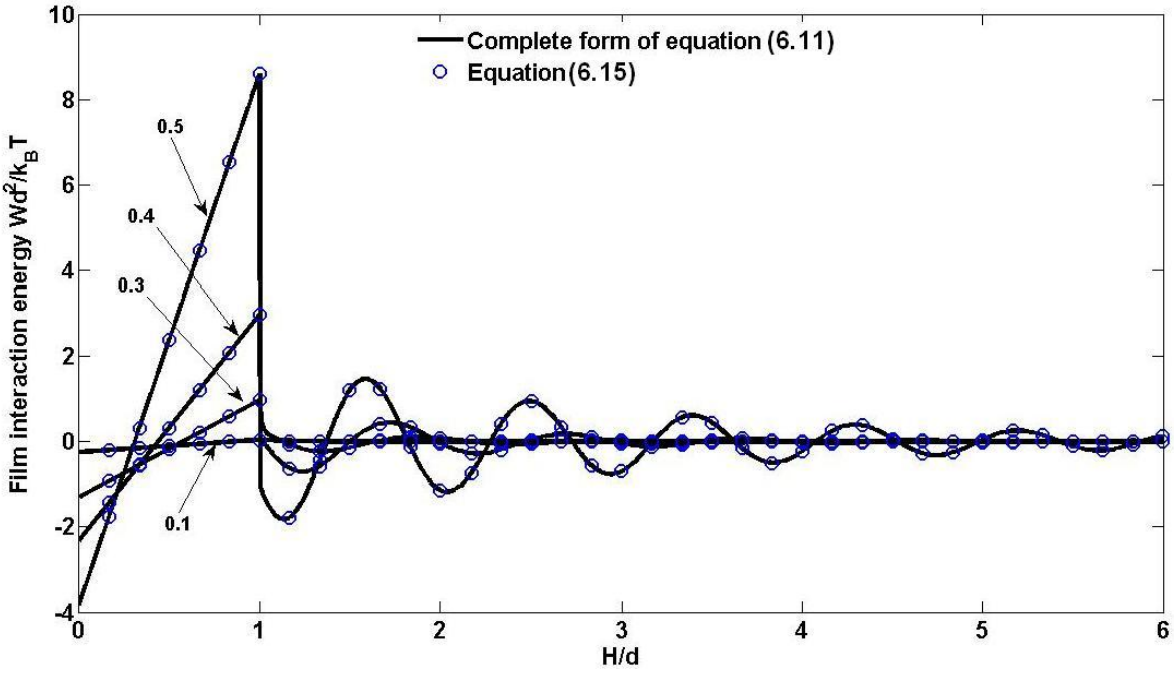

Figure 6-4: Comparison between equation (6.11) (complete form of the film interaction energy) and equation (6.15) (asymptotic form).

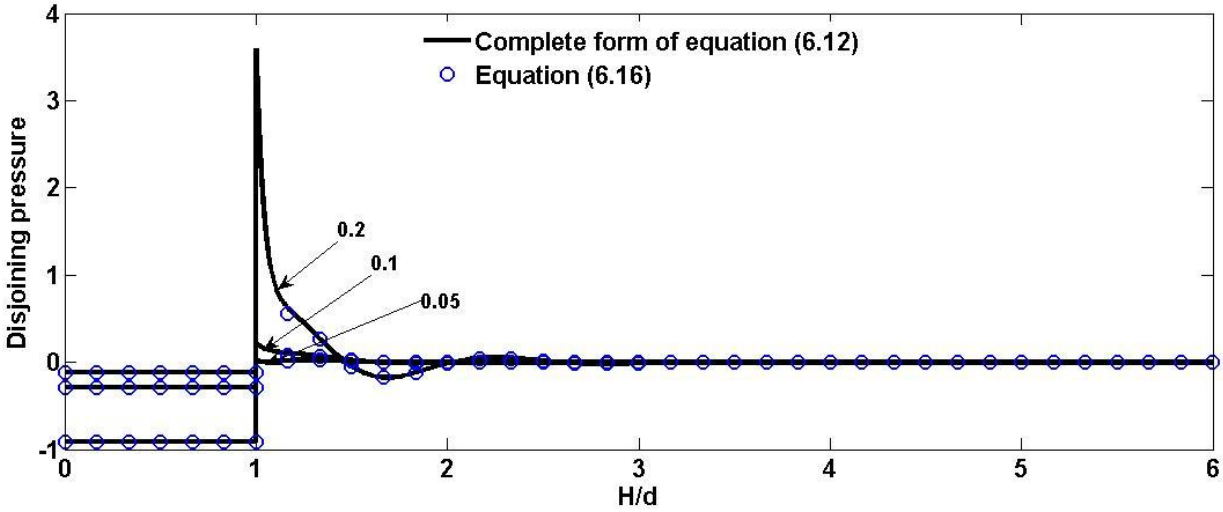

Figure 6-5: Comparison between equation (6.12) (complete form of the disjoining pressure) and equation (6.16) (asymptotic form).

After formation and during spreading, the film thickness (H) changes from the proximity of the three-phase contact line to the bulk nanofluid. When the thin fluid film is at equilibrium state, the excess film energy ($W\left(H\right)$) is a minimum. The equilibrium film thickness can be calculated by equating the equation for disjoining pressure (equation (6.16)) to zero (zeros of

ATTENTION: The Singapore Copyright Act applies to the use of this document. Nanyang Technological University Library

the disjoining pressure are locations in the film thickness where the film interaction energy is a minimum or maximum). For the particle volume concentrations used in this thesis, however, Figure 6-6 to Figure 6-10 show that the location of zero disjoining pressure corresponds to a maximum in the film interaction energy. In these figures, the disjoining pressure and the film interaction energy in the Y-axis are dimensionless disjoining pressure ($=\prod d^3/k_BT$) and dimensionless film interaction energy ($=Wd^2/k_BT$) and dimensionless equilibrium film thickness is denoted as H_e/d. Although these maximums denote equilibrium states, they are unstable equilibriums. In addition from these figures, it is obvious that there is no minimum in the film interaction energy along the film thickness. Thus, one can calculate the film interaction energy at film thickness approaching zero.

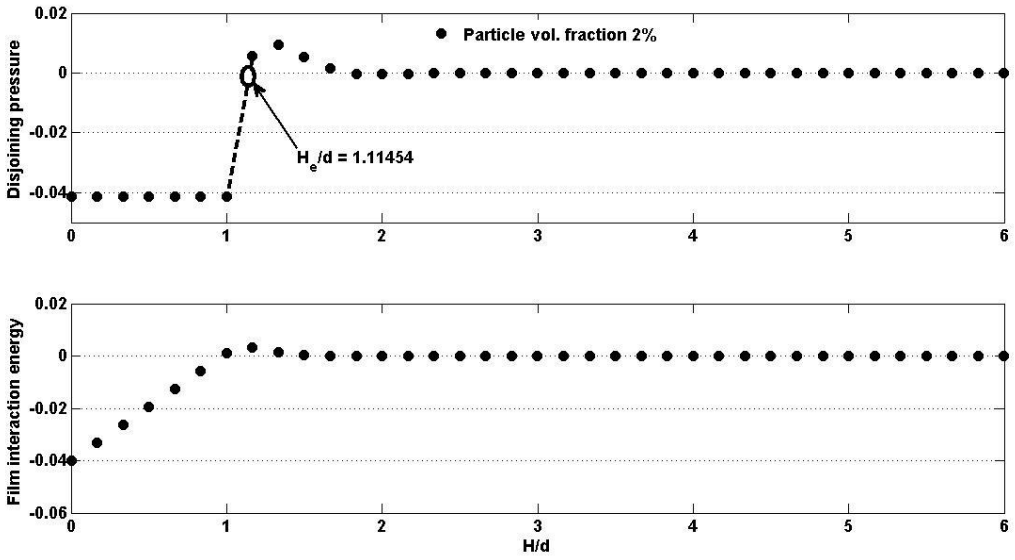

Figure 6-6: Location of equilibrium film thickness for $\phi = 2\%$.

ATTENTION: The Singapore Copyright Act applies to the use of this document. Nanyang Technological University Library

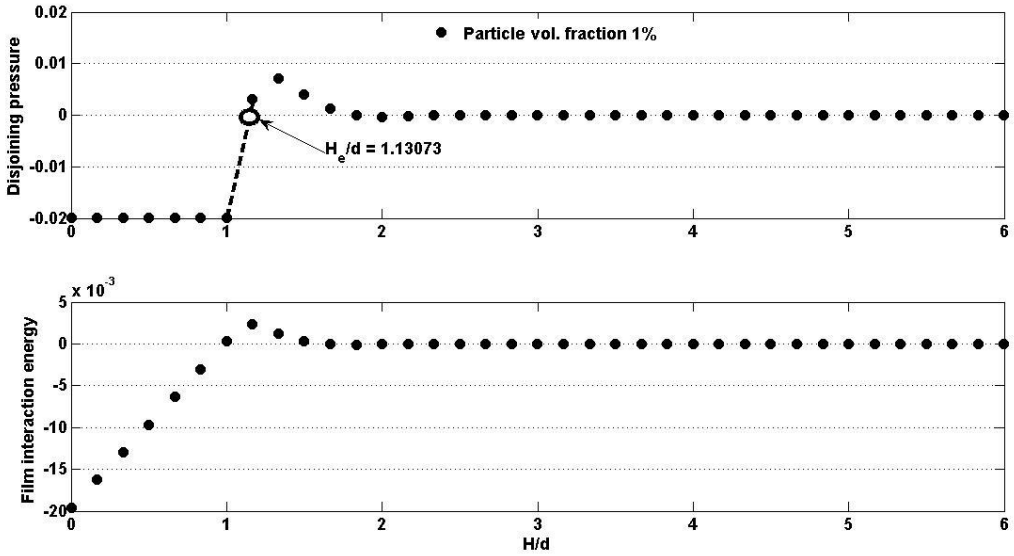

Figure 6-7: Location of equilibrium film thickness for $\phi = 1\%$.

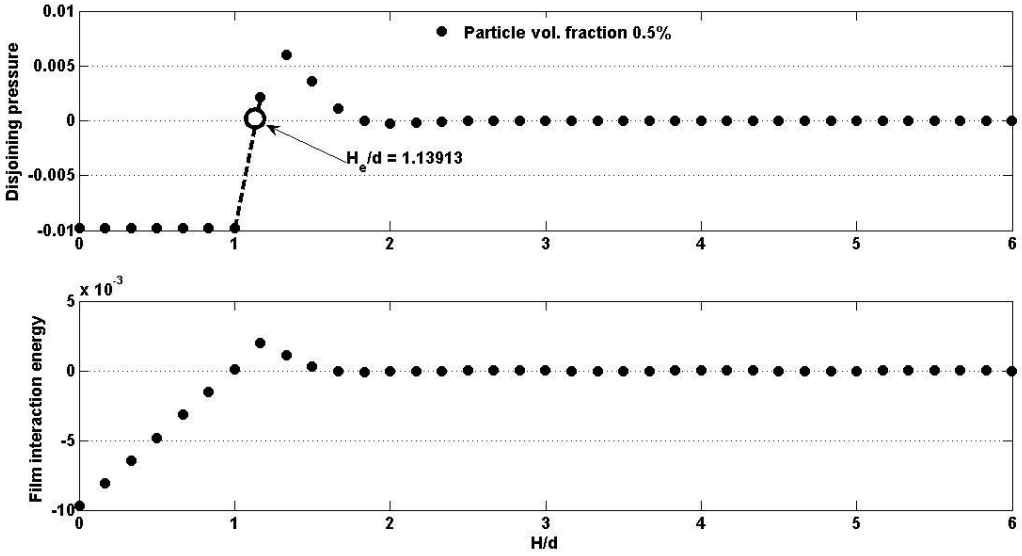

Figure 6-8: Location of equilibrium film thickness for $\phi = 0.5\%$.

ATTENTION: The Singapore Copyright Act applies to the use of this document. Nanyang Technological University Library

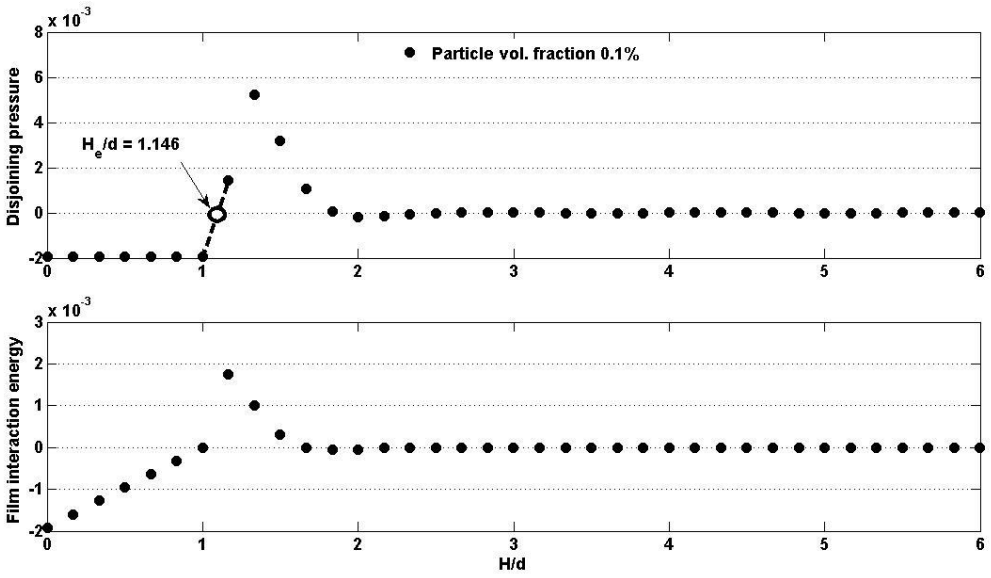

Figure 6-9: Location of equilibrium film thickness for $\phi = 0.1\%$.

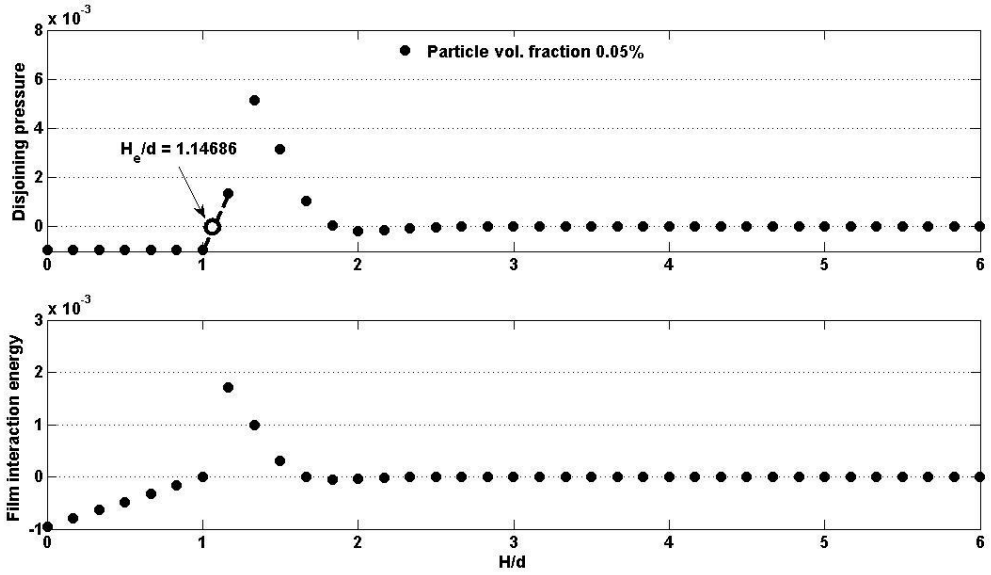

Figure 6-10: Location of equilibrium film thickness for $\phi = 0.05\%$.

Figure 6-6 to Figure 6-9 show that for particle volume fractions ranging from 0.0005 to 0.02 the location of equilibrium film thickness (which turned out to be unstable equilibrium) is larger than one particle diameter. In this region, the short-range van der Waals and repulsive interactions are insignificant. Table 6-1 shows values of the film interaction energies at the

ATTENTION: The Singapore Copyright Act applies to the use of this document. Nanyang Technological University Library

unstable film thickness (denoted by W_1) and film thickness approaching zero (denoted by W_2). The negative value for the film interaction energy at film thickness less than one particle diameter is due to depletion (osmotic) force in this region which is a retarding force. In order to correct the negative values of the film interaction energy at film thickness equal to or less than one particle diameter (which is unreasonable for hydrophilic solid surface), combined effects from van der Waals and repulsive forces, i.e. DLVO theory, should also be considered. However, at present, the characteristic parameters of the DLVO theory, such as Hamakar's constant, are not known for fluids laden with nanoparticles. Thus, further calculations are based on the unstable equilibrium film thickness (H_e/d). Table 6-1 also shows that both the structural and depletion forces increase with the particle vol. fraction. This is because higher particle concentrations in the bulk fluid results in denser patterned layers of particles within the fluid wedge, and as a result, higher structural disjoining pressure. On other hand, denser particle concentration in fluid wedge of thickness higher than one particle diameter, result in stronger osmotic pressure, i.e. higher depletion force.

Table 6-1: Equilibrium film thickness and film interaction energy for various particle vol. fractions.

Particle vol. fraction (ϕ)	**Thickness of zero disjoining pressure (H_e/d)**	**Film interaction energy ($W_1(h)$ [J/m^2]) × 10^{10}**	**Film interaction energy ($W_2(h)$ [J/m^2]) × 10^{10}**
2%	1.11454	3.4044	-41.319
1%	1.13073	2.4685	-20.144
0.5%	1.13913	2.0887	-9.9463

ATTENTION: The Singapore Copyright Act applies to the use of this document. Nanyang Technological University Library

0.1%	1.146	1.8215	-1.9694
0.05%	1.14686	1.7902	-0.98349

Dynamic contact angle

For a sessile droplet of spherical geometry, the base radius is related to the contact angle as follows:

$$r = \left(\frac{3V}{\pi} \frac{\sin^3 \theta}{2 - 3\cos\theta + \cos^3 \theta} \right)^{\frac{1}{3}}, \tag{6.17}$$

where V is the volume of the droplet. Based on this equation, the rate at which sessile droplet wets the solid surface can be written as follows [157]:

$$\frac{dr}{dt} = \frac{dr}{d\theta}\frac{d\theta}{dt} = \left[-\left(\frac{3V}{\pi} \frac{(1-\cos\theta)^6}{(2 - 3\cos\theta + \cos^3 \theta)^4} \right)^{\frac{1}{3}} \right] \frac{d\theta}{dt}. \tag{6.18}$$

It has been stated that in capillary action of liquids laden with nanoparticles, the driving energy per unit length of the contact line is a combination of the out of balance surface tension energy and the film interaction energy as follows:

$$f_{\text{dri}} = \gamma\left(\cos\theta^0 - \cos\theta\right) + W\ (H) \tag{6.19}$$

In this section, it is aimed to develop a sophisticated equation of contact line motion which incorporates the non-Newtonian behavior of these nanofluids at low shear rates in addition to the film interaction contribution to the contact line motion over the surface of the solid. It is assumed that the nanoparticles are evenly distributed in the carrier liquid; this assumption is

ATTENTION: The Singapore Copyright Act applies to the use of this document. Nanyang Technological University Library

however valid for very small Péclet numbers of order 10^{-7} for these nanofluids (see Table 2-1).

It is worth mentioning again that the spreading of nanofluids is due to two factors: first, spreading due to the imbalance of the three interfacial energies at the three-phase contact line, and second, spreading due to the excess (potential) energy of the disjoining pressure after the formation of a thin nanofluid film in front of the bulk nanofluid over the surface of the solid. Since the film forms at the final stages of droplet spreading, the film thickness can be assumed as a constant (i.e. $\partial H_{\Pi}/\partial t = 0$, in which the subscript Π denotes film thickness with effective disjoining pressure, namely less than six-particle diameter.) In the present study, it is assumed that the constant film thickness value corresponds to the primary zero of the disjoining pressure (See Sec. Structural and depletion components of the disjoining pressure).

It was also mentioned that two channels of energy dissipation are broadly considered in capillary flow which dissipate the driving energies: viscous dissipation and molecular kinetic dissipation [33]. Viscous dissipation occurs within two regions of different characteristic thicknesses, i.e. wedge film and precursor film. The apparent (macroscopic) contact angle is photographed in the wedge film. Ahead of the precursor film and in the proximity of the three-phase zone, movement of the fluid is governed by a molecular process in which molecules attach to adsorption sites on solid surface and the driving energy is partially dissipated to activate this process. The total dissipation per unit length of the contact line is usually expressed as follows:

$$T\Sigma_w + T\Sigma_f + T\Sigma_l \tag{6.20}$$

ATTENTION: The Singapore Copyright Act applies to the use of this document. Nanyang Technological University Library

in which $T\Sigma_w$, $T\Sigma_f$ and $T\Sigma_l$ are the dissipations in the wedge film, precursor film and proximity of the three-phase contact line, respectively. The formation of the precursor film for different pairs of solid and liquid is still unclear, although it has been proven for volatile liquids, and non-polar liquids [36]. Due to unknown flow patterns within the precursor film, $T\Sigma_f$ is usually dropped from equation (6.20). Calculation of $T\Sigma_l$ is based on the molecular kinetics theory which at low velocities gives the following equation [36]:

$$T\Sigma_l = \frac{\zeta U^2}{2} \tag{6.21}$$

where ζ is the coefficient of contact line friction (see equation (6.9)). For the purpose of calculating $T\Sigma_w$, the Navier-Stokes equation should be solved in the region of the wedge film toward the bulk nanofluid. For these non-Newtonian nanofluids, power law relation was used to exhibit the dependency of the effective viscosity on shear rate as follows:

$$\eta_n = \eta_b F(\phi) K \dot{\gamma}^{n-1}. \tag{6.22}$$

Figure 6-11 shows schematic diagram of the nanofluid flow in the wedge film. For film thickness (H) much smaller than the length ρ, i.e. $H \ll \rho$, the flow field can be assumed as quasi-1D and the steady state[10] Navier-Stokes equation of fluid motion is:

$$\frac{\partial p}{\partial x} = \frac{\partial}{\partial z}\left(\eta_n \frac{\partial u}{\partial z}\right) \tag{6.23}$$

[10] The steady state assumption is because the capillary flow Reynolds number (Re) and Weber number (We) are very small (see for example Table 3-1), thus inertia effect is insignificant comparing to capillary force and viscous drag force.

ATTENTION: The Singapore Copyright Act applies to the use of this document. Nanyang Technological University Library

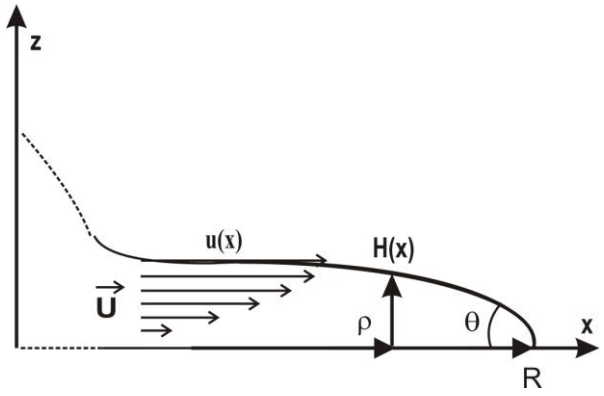

Figure 6-11: Schematic diagram of the nanofluid flow in the fluid wedge.

The pressure p can be obtained from the balance of gravity pressure and capillary pressure (i.e. pressure drop across the fluid-air interface). From Laplace equation (2.1) it follows that:

$$p_{z=H} - p_{\text{air}} = \gamma_n \left(\frac{1}{R_1} + \frac{1}{R_2} \right) \tag{6.24}$$

where R_1 and R_2 are the two principal radii at an arbitrary point (x, H) on the interface. The curvature $(1/R_1 + 1/R_2)$ can be obtained from the geometry of the fluid-air interface as follows:

$$\left(\frac{1}{R_1} + \frac{1}{R_2} \right) = \frac{-\left(\frac{\partial^2 H}{\partial x^2} \right)}{\left(1 + \left(\frac{\partial H}{\partial x} \right)^2 \right)^{3/2}} \tag{6.25}$$

Inserting equation (6.25) in equation (6.24), and adding the hydrostatic (gravity) pressure ($\rho g (H - z)$), the pressure field within the fluid wedge can be written as follows:

$$p = p_{\text{air}} + \rho g (H - z) - \gamma \frac{\left(\frac{\partial^2 H}{\partial x^2} \right)}{\left(1 + \left(\frac{\partial H}{\partial x} \right)^2 \right)^{3/2}} \tag{6.26}$$

ATTENTION: The Singapore Copyright Act applies to the use of this document. Nanyang Technological University Library

Integration of equation (6.23) with respect to z and assuming no stress boundary condition at the free fluid-air interfaces:

$$\left.\frac{\partial u}{\partial z}\right|_{z=H} = 0 \tag{6.27}$$

leads to:

$$\frac{\partial p}{\partial x}(H - z) = \eta_b F(\phi) K \left(\frac{\partial u}{\partial z}\right)^n \tag{6.28}$$

Integration of equation (6.28) with respect to z and assuming no slip boundary condition at the solid surface:

$$u_{z=0} = 0 \tag{6.29}$$

gives the following expression for the flow field velocity:

$$u = \frac{1}{\left(\eta_b F(\phi) K\right)^{\frac{1}{n}}} \left(\frac{\partial p}{\partial x}\right)^{\frac{1}{n}} \frac{n}{n+1} \left(H^{\frac{1}{n}+1} - (H - z)^{\frac{1}{n}+1} \right) \tag{6.30}$$

In fact in surface tension driven flows, it is usually assumed that the average fluid velocity ($\bar{u} = \int_0^H u dz \Big/ H$) is equal to the contact line velocity (U). Thus, the contact line velocity is obtained as follows:

ATTENTION: The Singapore Copyright Act applies to the use of this document. Nanyang Technological University Library

$$U = \frac{n}{n+1}\frac{1}{\left(\eta_b F(\phi) K\right)^{\frac{1}{n}}}\left(\frac{\partial p}{\partial x}\right)^{\frac{1}{n}}\frac{1}{H}\left\langle\left(\int_0^H H^{\frac{1}{n}+1}dz - \int_0^H (H-z)^{\frac{1}{n}+1}dz\right)\right\rangle$$
$$= \frac{1}{\left(\eta_b F(\phi) K\right)^{\frac{1}{n}}}\left(\frac{\partial p}{\partial x}\right)^{\frac{1}{n}}\left(\frac{n}{1+2n}\right)H^{\frac{1}{n}+1} \tag{6.31}$$

Hence, the flow field velocity as function of contact line velocity can be written as follows:

$$u = \frac{2n+1}{n+1}U\left(1-\left(1-\frac{z}{H}\right)^{\frac{1}{n}+1}\right) \tag{6.32}$$

Accordingly, shear rate can also be written as follows:

$$\frac{\partial u}{\partial z} = \frac{2n+1}{n}U\left(\frac{1}{H}\right)\left(1-\frac{z}{H}\right)^{\frac{1}{n}} \tag{6.33}$$

The viscous dissipation integrated over the wedge film thickness can be written as follows [36]:

$$\int_0^H \tau\left(\frac{\partial u}{\partial z}\right)dz = \int_0^H \eta_n\left(\frac{\partial u}{\partial z}\right)^2 dz \tag{6.34}$$

Substituting equation (6.22) into equation (6.34) and integrating, it follows that:

$$\int_0^H \tau\left(\frac{\partial u}{\partial z}\right)dz = \int_0^H \eta_b F(\phi) K\left(\frac{\partial u}{\partial z}\right)^{n+1} dz$$
$$= \int_0^H \eta_b F(\phi) K\left(\frac{2n+1}{n}U\left(\frac{1}{H}\right)\left(1-\frac{z}{H}\right)^{\frac{1}{n}}\right)^{n+1} dz$$
$$= \eta_b F(\phi) K\left(\frac{2n+1}{n}\right)^{n+1}\left(\frac{1}{H}\right)^{n+1} U^{n+1}\int_0^H \left(1-\frac{z}{H}\right)^{\frac{n+1}{n}} dz \tag{6.35}$$
$$= \eta_b F(\phi) K\left(\frac{2n+1}{n}\right)^{n}\left(\frac{1}{H}\right)^{n} U^{n+1}$$

ATTENTION: The Singapore Copyright Act applies to the use of this document. Nanyang Technological University Library

Thus, the total viscous dissipation in the wedge film per unit length of the contact line is as follows:

$$T\,\Sigma_W = \int_0^{r-x_m}\left[\int_0^H \tau\left(\frac{\partial u}{\partial z}\right)dz\right]d\rho = \eta_b F(\phi) K\left(\frac{2n+1}{n}\right)^n U^{n+1}\left\{\int_0^{r-x_m}\left[\left(\frac{1}{H}\right)^n\right]d\rho\right\} \tag{6.36}$$

where x_m is the cut-off length (similar to the so-called slip length in Hydrodynamic theory) because the above integration excludes the cut-off length [36]. Without consideration of this characteristic length, dissipation of energy at the contact line will grow infinitely. For small contact angles and thin wedge film, the following relation persists between ρ and H :

$$\frac{H}{r-\rho} = \tan\theta \simeq \theta \tag{6.37}$$

Inserting equation (6.37) into equation (6.36) and integrating, the following equation can be obtained as the total viscous dissipation in the wedge film per unit length of the contact line:

$$\begin{aligned} T\,\Sigma_W &= \eta_b F(\phi) K\left(\frac{2n+1}{n}\right)^n U^{n+1}\left\{\int_0^{r-x_m}\left[\left(\frac{1}{(r-\rho)\theta}\right)^n\right]d\rho\right\} \\ &= \eta_b F(\phi) K\left(\frac{2n+1}{n}\right)^n U^{n+1}\frac{1}{\theta^n}\left[\frac{r^{1-n}-x_m{}^{1-n}}{1-n}\right] \end{aligned} \tag{6.38}$$

Combining equations (6.21) and (6.38), the total dissipation due to molecular effects and viscous effects can be obtained as follows:

$$T\,\Sigma_{l+W} = \frac{\zeta U^2}{2} + \eta_b F(\phi) K\left(\frac{2n+1}{n}\right)^n U^{n+1}\frac{1}{\theta^n}\left[\frac{r^{1-n}-x_m{}^{1-n}}{1-n}\right] \tag{6.39}$$

Derivation of the total dissipation function with respect to the contact line velocity will result in the total drag force, as follows:

ATTENTION: The Singapore Copyright Act applies to the use of this document. Nanyang Technological University Library

$$f_{drag} = \frac{\partial T \Sigma_{l+W}}{\partial U} = \zeta U + \eta_b F(\phi) K \left(\frac{2n+1}{n}\right)^n \left(\frac{1+n}{1-n}\right) U^n \frac{1}{\theta^n} \left[r^{1-n} - x_m{}^{1-n} \right] \quad (6.40)$$

Equating the total drag force with the total driving force (equation (6.19)) gives the equation of contact line motion as follows:

$$\gamma_n \left(\cos\theta^0 - \cos\theta\right) + W\left(H_\Pi\right) = \zeta U + \eta_b F(\phi) K \left(\frac{2n+1}{n}\right)^n \left(\frac{1+n}{1-n}\right) \frac{1}{\theta^n} \left[r^{1-n} - x_m{}^{1-n} \right] U^n \quad (6.41)$$

It is noted that r is the base radius of the sessile droplet (which is of millimeter length scale) and x_m is the slip length (which is of nanometer length scale). Thus, $r \gg x_m$, and consequently $r^{1-n} \gg x_m{}^{1-n}$. Neglecting $x_m{}^{1-n}$ equation (6.41) reads:

$$\gamma_n \left(\cos\theta^0 - \cos\theta\right) + W\left(H_\Pi\right) = \zeta U + \eta_b F(\phi) K \left(\frac{2n+1}{n}\right)^n \left(\frac{1+n}{1-n}\right) r^{1-n} \frac{U^n}{\theta^n} \quad (6.42)$$

Substituting r with equation (6.17), equation (6.42) reads:

$$\gamma_n \left(\cos\theta^0 - \cos\theta\right) + W\left(H_\Pi\right) =$$

$$\zeta U + \eta_b F(\phi) K \left(\frac{2n+1}{n}\right)^n \left(\frac{1+n}{1-n}\right) \frac{\left(\frac{3V}{\pi} \frac{\sin^3\theta}{2-3\cos\theta+\cos^3\theta}\right)^{\frac{1-n}{3}} U^n}{\theta^n} \quad (6.43)$$

Equation (6.43) shows the dynamic contact angle of a spreading nanofluid (θ) as function of contact line velocity, solid-liquid interactions, interparticular interactions and non-Newtonian viscosity.

Finally, substituting U with $dr/dt = (dr/d\theta) \times (d\theta/dt)$ (see equation (6.18)) the following evolution equation can be obtained for the dynamic contact angle:

ATTENTION: The Singapore Copyright Act applies to the use of this document. Nanyang Technological University Library

$$\gamma_n\left(\cos\theta^0-\cos\theta\right)+W\left(H_\Pi\right)=\zeta\left[-\left(\frac{3V}{\pi}\frac{\left(1-\cos\theta\right)^6}{\left(2-3\cos\theta+\cos^3\theta\right)^4}\right)^{\frac{1}{3}}\right]\frac{d\theta}{dt}$$
$$+\eta_b F\left(\phi\right)K\left(\frac{2n+1}{n}\right)^n\left(\frac{1+n}{1-n}\right)\left[\left(\frac{3V}{\pi}\frac{\sin^3\theta}{2-3\cos\theta+\cos^3\theta}\right)^{\frac{1}{3}}\right]^{1-n} \qquad (6.44)$$
$$\times\left[\left(\frac{3V}{\pi}\frac{\left(1-\cos\theta\right)^6}{\left(2-3\cos\theta+\cos^3\theta\right)^4}\right)^{\frac{1}{3}}\right]^n\left(\frac{-d\theta/dt}{\theta}\right)^n$$

Equation (6.44) cannot be solved in the above form due to the presence of the negative sign (-) to power of a decimal number (n). For this purpose, it is useful to change the dependant variable θ with its supplementary angle α $(=\pi-\theta)$. Introducing the new dependant variable α to the above equation, the following equation can be obtained:

$$\gamma_n\left(\cos\alpha-\cos\alpha^0\right)+W\left(H_\Pi\right)=\zeta\left[\left(\frac{3V}{\pi}\frac{\left(1+\cos\alpha\right)^6}{\left(2+3\cos\alpha-\cos^3\alpha\right)^4}\right)^{\frac{1}{3}}\right]\frac{d\alpha}{dt}$$
$$+\eta_b F\left(\phi\right)K\left(\frac{2n+1}{n}\right)^n\left(\frac{1+n}{1-n}\right)\left[\left(\frac{3V}{\pi}\frac{\sin^3\alpha}{2+3\cos\alpha-\cos^3\alpha}\right)^{\frac{1}{3}}\right]^{1-n} \qquad (6.45)$$
$$\times\left[\left(\frac{3V}{\pi}\frac{\left(1+\cos\alpha\right)^6}{\left(2+3\cos\alpha-\cos^3\alpha\right)^4}\right)^{\frac{1}{3}}\right]^n\left(\frac{d\alpha/dt}{\pi-\alpha}\right)^n$$

This equation is an implicit differential equation, which cannot be solved analytically, thus numerical calculations (with aid of MATLAB software) were used to solve this equation.

ATTENTION: The Singapore Copyright Act applies to the use of this document. Nanyang Technological University Library

Theory of capillary flow of nanofluids

Theory of surface tension driven capillary flow have been studied in Chapters 3 and 4; however, the final equations (equations (3.24) and (4.16)) were for Newtonian liquids. For TiO_2 – DI water nanofluids which exhibit non-Newtonian shear viscosity, the viscous drag force should be modified. Schematic of the flow is shown in Figure 6-12. For capillary flow from a pendant droplet, the configuration is the same as Figure 4-6.

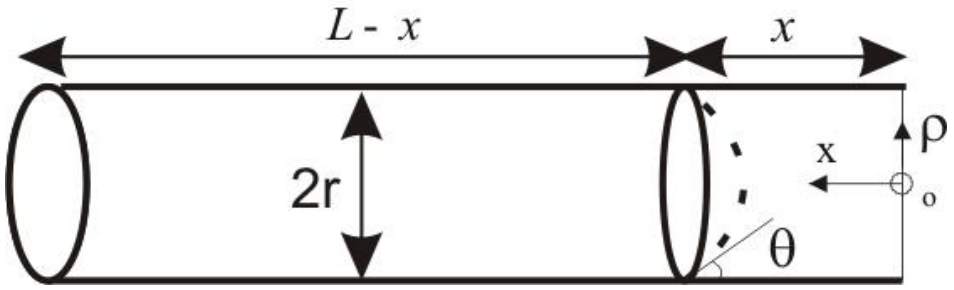

Figure 6-12: Schematic of capillary flow.

Starting from the steady-state fully developed Navier-Stokes equation of motion (see Ref. [158]):

$$\frac{dp}{dx} = \frac{1}{\rho}\frac{\partial(\rho\tau)}{\partial\rho} \tag{6.46}$$

where ρ is the radial coordinate ($0 < \rho < r$), the driver pressure p is the capillary pressure, $p = 2\gamma_n \cos\theta / r$ (Laplace's equation), $\tau = \eta_n \, \partial u/\partial\rho$ is the shear stress and η_n follows a power-law relation which is $\eta_n = \eta_b F(\phi) K (\partial u/\partial\rho)^{n-1}$, it follows that[11]:

$$\frac{2\gamma_n \cos\theta}{rx} = -\eta_b F(\phi) K \frac{1}{\rho}\frac{\partial\left[\rho\left(-\frac{\partial u}{\partial\rho}\right)^n\right]}{\partial\rho} \tag{6.47}$$

[11] See *Sec.* Theoretical investigation, Chapter 3, for details on how to insert the surface pressure p into the continuum Navier-Stokes equation of motion.

ATTENTION: The Singapore Copyright Act applies to the use of this document. Nanyang Technological University Library

Integrating both sides of equation (6.47) with respect to ρ and applying the following boundary condition:

$$\left.\frac{\partial u}{\partial \rho}\right|_{\rho=0} = 0 \tag{6.48}$$

it follows that:

$$\frac{\partial u}{\partial \rho} = -\sqrt[n]{\frac{\gamma_n \cos\theta}{-\eta_b F(\phi) K r x}\,\rho} \tag{6.49}$$

The second integration results in:

$$u = \sqrt[n]{\frac{\gamma_n \cos\theta}{\eta_b F(\phi) K r x}}\,\frac{n}{n+1}\left(-\rho\right)^{1+\frac{1}{n}} + C \tag{6.50}$$

where C is the constant of integration. Applying the following boundary condition:

$$u\big|_{\rho=r} = 0 \tag{6.51}$$

it follows that:

$$u = \sqrt[n]{\frac{\gamma_n \cos\theta}{\eta_b F(\phi) K r x}}\,\frac{n}{n+1}\left[\left(-\rho\right)^{1+\frac{1}{n}} - \left(-r\right)^{1+\frac{1}{n}}\right] \tag{6.52}$$

The average flow velocity (which is equal to the contact line velocity, U) can be obtained as follows:

$$\bar{u} = U = \sqrt[n]{\frac{\gamma_n \cos\theta}{\eta_b F(\phi) K r x}}\,\frac{n}{1+3n}(-1)^{\frac{1}{n}} r^{\frac{1+n}{n}} \tag{6.53}$$

Thus flow field velocity as a function of contact line velocity is as follows:

ATTENTION: The Singapore Copyright Act applies to the use of this document. Nanyang Technological University Library

$$u = \frac{1+3n}{1+n}\left[1-\left(\frac{\rho}{r}\right)^{1+\frac{1}{n}}\right]U \tag{6.54}$$

Thus, at the side wall, the shear stress can be obtained as follows:

$$\tau = \eta_b F(\phi) K \left(3+\frac{1}{n}\right)^n \frac{U^n}{r^n} \tag{6.55}$$

Finally from equation (6.49) it is possible to obtain the viscous drag force as follows:

$$F_{\text{drag}} = 2\pi x \eta_b F(\phi) K \left(3+\frac{1}{n}\right)^n \frac{U^n}{r^{n-1}} \tag{6.56}$$

From equation (4.2), the total surface tension force was calculated as follows:

$$F_\gamma = -\gamma.\left(-2\pi r\cos\theta + \frac{dA_{la,1}}{dx}\right) = 2\pi r\gamma\cos\theta - \gamma\frac{dA_{la,1}}{dx} \tag{6.57}$$

where the first term on the right hand side of equation (6.57) is the surface tension force in the capillary tube and the second term is the capillary force due to pendant droplet curvature. For the case of an infinite reservoir (beaker with an inlet arm), dropping the second term gives the right hand side of equation (6.57).

It has been stated that in capillary flow, the Reynolds number and Weber number are very small and the inertia effect is negligible as compared to the viscous drag and surface tension forces (see *Sec.* Theoretical investigation, Chapter 3). Hence, equating equations (6.56) and (6.57), which are the total drag force and the total driving force respectively, the equation of surface tension driven nanofluid motion in the capillary tube can be obtained as follows:

$$2\pi r\gamma\cos\theta - \gamma\frac{dA_{la,1}}{dx} = 2\pi x \eta_b F(\phi) K \left(3+\frac{1}{n}\right)^n \frac{U^n}{r^{n-1}} \tag{6.58}$$

ATTENTION: The Singapore Copyright Act applies to the use of this document. Nanyang Technological University Library

The important variables of equation (6.58) are the dynamic contact angle, whose dependency on the contact line velocity can be obtained from equation (6.42), contact line velocity *U*, and in case of penetration from a pendant droplet, $dA_{la,1}/dx$ is also an important factor. It is noted that in the above derivation, shear-induced particle migration in not included (see Page 28 and 29). Two reasons can be stated for this omission. First, the shear-induced particle migration which is well described by Péclet number (equation (2.39)) as opposing Brownian motion, is totally insignificant for nano-sized particles for which $Pe \ll 1$, namely in order of 10^{-7}. However, due to agglomeration and clustering of nanoparticles, the effective particle size is higher and the shear-induced particle migration may become important. But, it is only at initial stages of penetration, after which due to the rapid drop in penetration velocity (or shear rate) the Péclet number decreases very fast and the effect becomes insignificant again.

4. Results and discussion

Viscosity

In order to obtain values of *n* for these nanofluids, as shown in Figure 6-14, logarithm of the dimensionless viscosity, i.e. η_n/η_b , was plotted versus logarithm of shear rate. Linear trend (which is a characteristic of power-law fluids) is observed for 0.5% to 2% vol. concentrations. From slopes of these lines, the power-law index *n* for these nanofluids can be calculated. The power-law index for 0.05% and 0.1% vol. concentration is found to be close to 1. It is also obvious that for higher nanoparticle volume concentrations the power-law index (*n*) is lower (see Table 6-2). This indicates stronger deviations from Newtonian behavior for higher volume concentrations of these nanofluids. The proportionality factor (*K*) is shown in Figure 6-15 for various particle volume concentrations calculated by three different formulations, Kreiger's (1972), Leighton and Acrivos' (1987), and Morris and

ATTENTION: The Singapore Copyright Act applies to the use of this document. Nanyang Technological University Library

Boulay's (1999). It is observed that all formulations roughly result in the same values; however, for the purpose of further calculations Leighton and Acrivos' formula is adapted. Finally inserting curve-fitted values for *n* and *K* in equation (6.1), Figure 6-13 shows that this equation gives a good trend in comparison with experimental data.

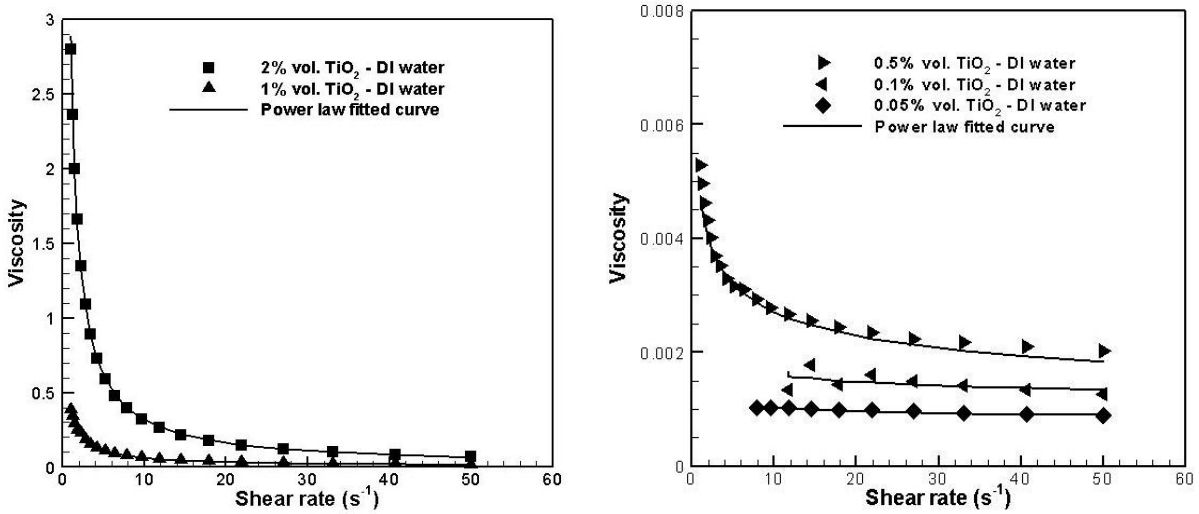

Figure 6-13: Viscosity of TiO_2 – DI water nanofluids.

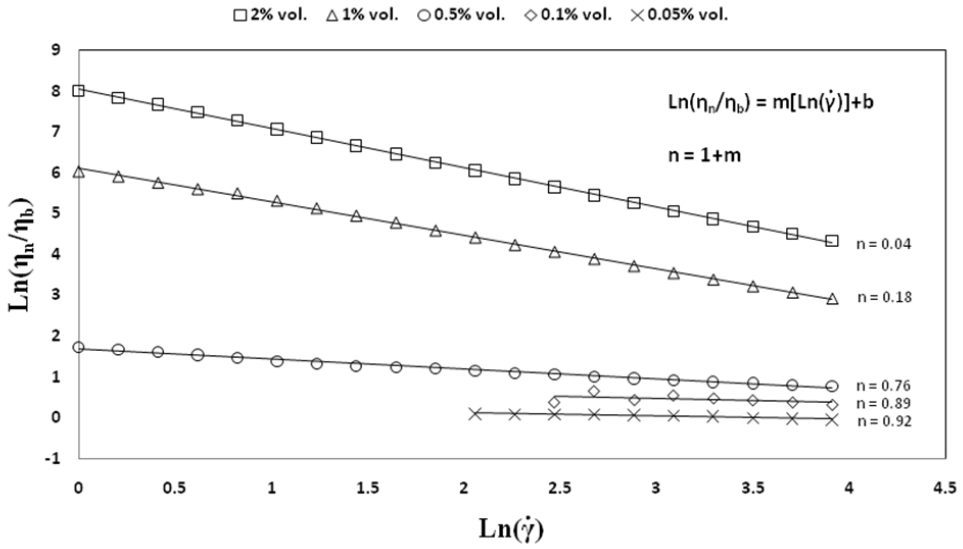

Figure 6-14: Power-law index of TiO_2 – DI water nanofluids.

ATTENTION: The Singapore Copyright Act applies to the use of this document. Nanyang Technological University Library

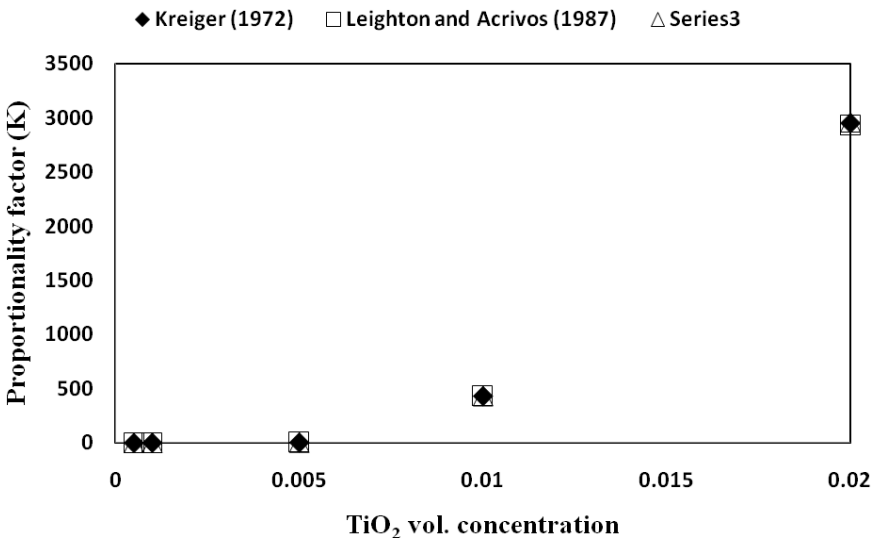

Figure 6-15: Variation of proportionality factor (K) with respect to particle volume fraction.

Table 6-2: Properties of power-law behavior of nanofluids at low shear rates.

TiO_2 vol. concentration (ϕ)	Power-law index (n)	Proportionality factor (K)
2%	0.04	2932
1%	0.18	432
0.5%	0.76	5
0.1%	0.89	2
0.05%	0.92	1

Spreading

Figure 6-16 shows dynamic contact angle of TiO_2 – DI water nanofluids with nanoparticle volume concentration ranging from 0.05% to 2%. Due to the limitation in camera speed (30 fps) the onset when the pendant droplet suddenly touches the surface of the solid cannot be

ATTENTION: The Singapore Copyright Act applies to the use of this document. Nanyang Technological University Library

determined accurately. The very fast spreading of the nanofluid over the solid surface was also unable to be captured and only shadows of the edge were visible (see Figure 6-17). Hence, the time-axis in Figure 6-16 is shifted from the real zero time to a new time where all of the captured images were readable by the software to measure the contact angle.

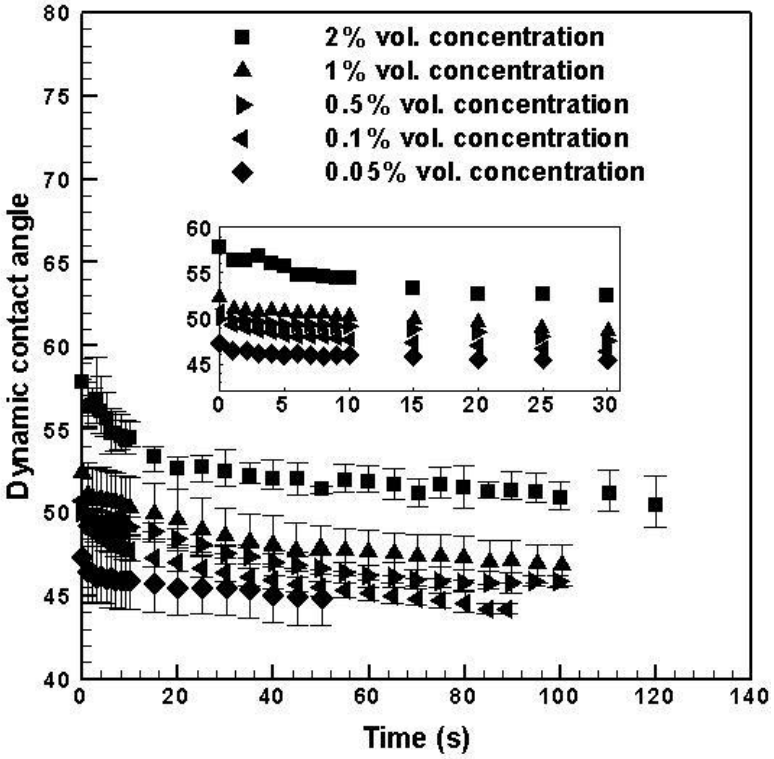

Figure 6-16: Dynamic contact angle of TiO_2 - DI water nanofluids.

ATTENTION: The Singapore Copyright Act applies to the use of this document. Nanyang Technological University Library

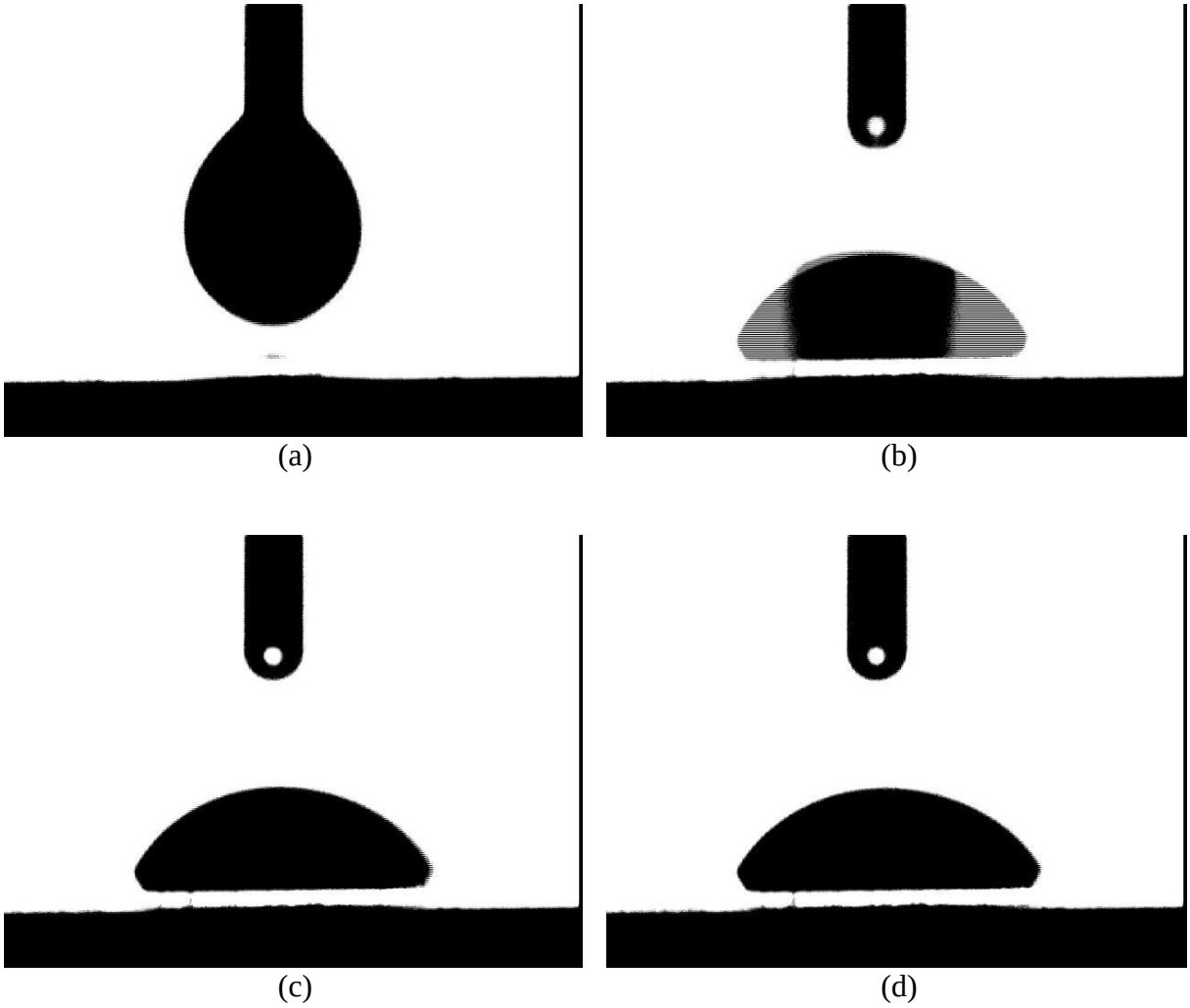

Figure 6-17: Subsequent images of a nanofluid touching a solid surface and the very rapid initial spreading. The software can only measure the contact angle of the image (d). The time interval between two images is 0.04 s.

From Figure 6-16 it is obvious that for higher nanoparticle concentrations the dynamic contact angles are higher. Spreading of these nanofluids start from a primary region where the contact angle changes rapidly followed by a region where the contact angle changes gradually. In the primary region (which is about 30 seconds) contact line velocity is higher and thus most of the dissipations occur in the wedge film ($T\Sigma_w$). In the secondary region due to a smaller contact line velocity, the dominant dissipative mechanism is the contact line dissipation ($T\Sigma_l$). Nanoparticles can affect both these mechanisms with complex interparticle interactions. Without nanoparticles, it has been stated that there are two flow patterns in the wedge film: rolling pattern and lubricating pattern [36]. Nanoparticles in the

ATTENTION: The Singapore Copyright Act applies to the use of this document. Nanyang Technological University Library

wedge film can change these flow patterns and result in more complex field structures. As a result of these interparticle interactions, dissipation is stronger in the wedge film[12]. Adsorption of nanoparticles to the surface of the solid can also affect the contact line dissipation by changing surface properties at the solid surface and resulting in new adsorption sites on the solid surface. Pinning of contact line also happens due to the same effect. In theory, it is not possible to model all these effects, and only simple models which can accommodate some of these effects can be developed. Comparison of experimental data of TiO_2 – DI water nanofluid spreading with the theory (equation (6.44)) is shown in Figure 6-18. It is obvious that the theory is giving a qualitative trend in comparison with experiments. The mean squared error (MSE) for all of the concentrations is less than 1.3. MSE is measured from the following equation:

$$\mathrm{MSE} = \frac{1}{n}\sum_{i=1}^{n} e_i^2 \tag{6.59}$$

where e_i is the difference between the observed data and the fitted model.

It is finally noted that the solution to the implicit equation (6.45) resulted in complex values for dynamic contact angle of 0.05% and 0.1% vol. concentrations, in which the imaginary part is very small namely in the order of 10^{-2} while the real part is in the order of 10^2. In Figure 6-18, the real parts of the data are used to compare with experiments. Although complex data are unphysical (only mathematically acceptable), solution to the highly non-linear and very stiff equation (6.45) needs more advanced numerical algorithms such as Richardson extrapolation, Bulirsch-Stoer method etc to handle these types of equations. It is also noted that for the solution of this equation, experimental data were used for n, K and γ; droplet volume (V) was also fixed at 6 μl for all of the mixtures, which might be different due

[12] Such study seems to be rare in literature.

ATTENTION: The Singapore Copyright Act applies to the use of this document. Nanyang Technological University Library

to experimental errors. Correction of the developed equations which result in the final form of equation (6.45) is asserted by dynamic contact angles of 0.5%, 1% and 2% vol. concentrations which are completely real values.

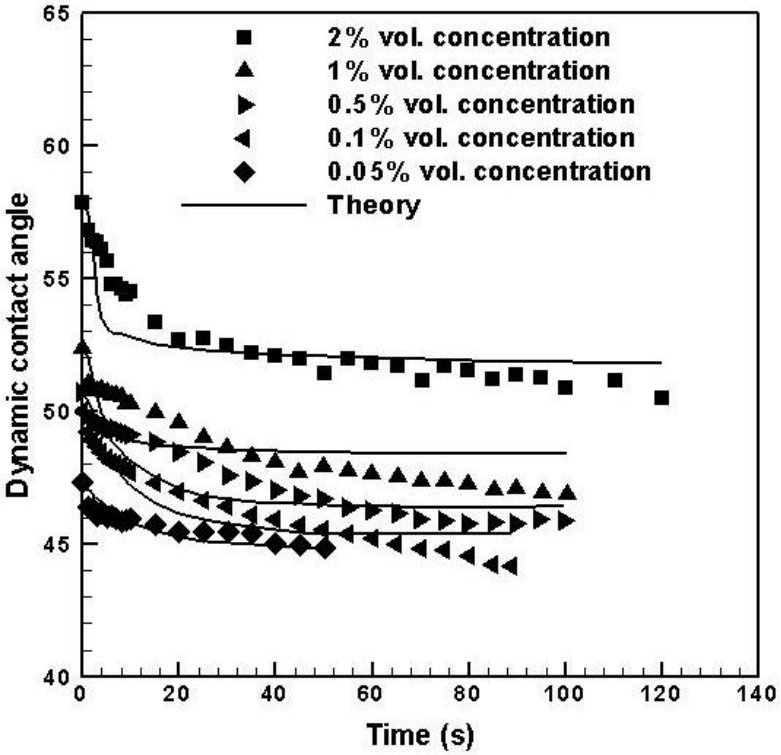

Figure 6-18: Comparison of experimental data of TiO_2 – DI water nanofluid spreading with theory.

Table 6-3 shows values of ζ (coefficient of friction at the contact line). It is obvious that for higher nanoparticle concentrations, ζ is smaller. As ζ denotes dissipation of energy at the contact line ($T\sum_l = \zeta U^2/2$, equation (6.21)), smaller values of this parameter (at higher nanoparticle concentration as compared to lower nanoparticle concentrations) reveal that most dissipation happens at the wedge film ($T\sum_W$) for higher nanoparticle concentrations. This is however attributed to the presence of a large amount of nanoparticles in the wedge film and the corresponding changes in the flow field thereof. Despite lower nanoparticle concentrations, the nanoparticle have less effect on the flow field of the wedge film, thus most of the dissipations happen at the contact line. Also shown in the Table 6-3 are the

ATTENTION: The Singapore Copyright Act applies to the use of this document. Nanyang Technological University Library

theoretical equilibrium contact angles, θ^0_{theory}, which give the least MSE for the present theoretical calculations.

Table 6-3: Parameters and error of fitted model.

Nanoparticle concentration	ζ	θ^0_{theory}	$\theta^0_{\text{exp.}}$	**MSE**
2%	32	45.5	51.7	1.2
1%	99	48.2	47.5	1
0.5%	464	46.4	46.7	0.4
0.1%	483	45.3	45.7	0.3
0.05%	486	44.8	44.5	0.1

Capillary flow

Penetration of TiO_2 – DI water nanofluids into glass capillaries was observed to be unstable due to the unevenness of the nanofluid column. It was observed that initially the nanofluid penetrated the glass capillary (seemingly) with the exact bulk concentration; however, after an initial penetration length of about 1 cm, the penetrating nanofluid was observed to be less concentrated. The judgment is however based on intensity of white color of these nanofluids (see Figure 6-19). This effect is attributed to the higher affinity of glass to absorb water than mixture of water with titanium oxide nanoparticles. Figure 6-19 shows that the white color density of a penetrating nanofluid (2%) pendant droplet is changing from 7 cm to 1 cm, being most concentrated in 7 cm and least concentrated in region of 1 cm.

ATTENTION: The Singapore Copyright Act applies to the use of this document. Nanyang Technological University Library

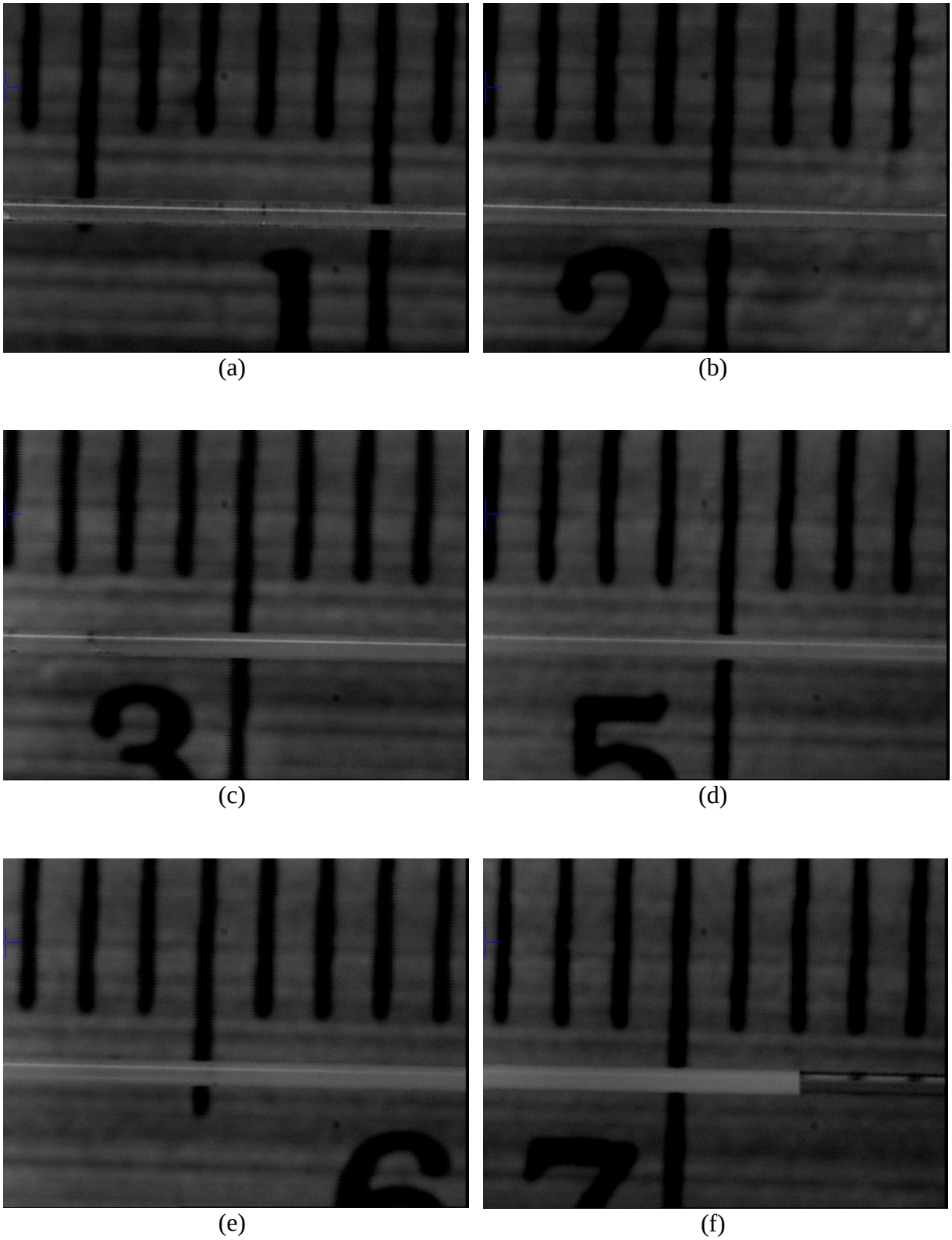

(a) (b) (c) (d) (e) (f)

Figure 6-19: Decrease in white color density from 7 cm (f) to 1 cm (a). Images are for 2% TiO_2 - DI water nanofluid in 300 µm capillary.

ATTENTION: The Singapore Copyright Act applies to the use of this document. Nanyang Technological University Library

By adsorption of dilute nanofluid instead of the actual dense nanofluid, less number of nanoparticles was adsorbed in the capillary tube and remained nanoparticles accumulated at the capillary entrance; this resulted in an intense white color at the capillary entrance due to accumulation of nanoparticles (see Figure 6-20).

Figure 6-20: An intense white color nanofluid present at the capillary entrance.

It is noted that for these experiments, the nanofluids were used right after sonication and no sedimentation was observed for the duration of experiments. To ensure that no air bubbles were present in the solution, it was ultra-sonicated with ultra sonic bath (Fisher Ultrasonic Cleaner 4000) for 10 minutes. It is noted that penetration of air bubbles could easily plug the capillary channel.

Another instability occurred specifically in beaker with an inlet arm configuration. It was observed that after a rapid meniscus wake the flow gradually slowed down and eventually stopped. The length at which the meniscus stopped was less than 10 cm and differed for different capillary diameters. For 700 μm capillary it happened namely at 6 cm while for 300 μm capillary the nanofluid stopped penetrating two times; the primary stop was near 2 cm. It was found that more insertion of the capillary tube into the beaker inlet arm would re-start the

ATTENTION: The Singapore Copyright Act applies to the use of this document. Nanyang Technological University Library

penetration. This instability is also attributed to the above mentioned effect in which the accumulation of nanoparticles at the capillary entrance blocked nanofluid from penetrating into the capillary tube. In order to solve this problem, the capillary tube was initially inserted 5 mm (from the surface of contact with the nanofluid) into the inlet arm; this however resulted in complete penetration of the nanofluid.

Near the capillary entrance (namely from 0 to 1 cm) a train of plugs of dilute nanofluid and concentrated nanofluid was also observed (see Figure 6-21). The train formed when the nanofluid with accumulated nanoparticles was suddenly sucked in the capillary tube, after which a dilute solution was again sucked in. These instabilities were however less evident in 1% vol. nanofluid than in 2% vol.

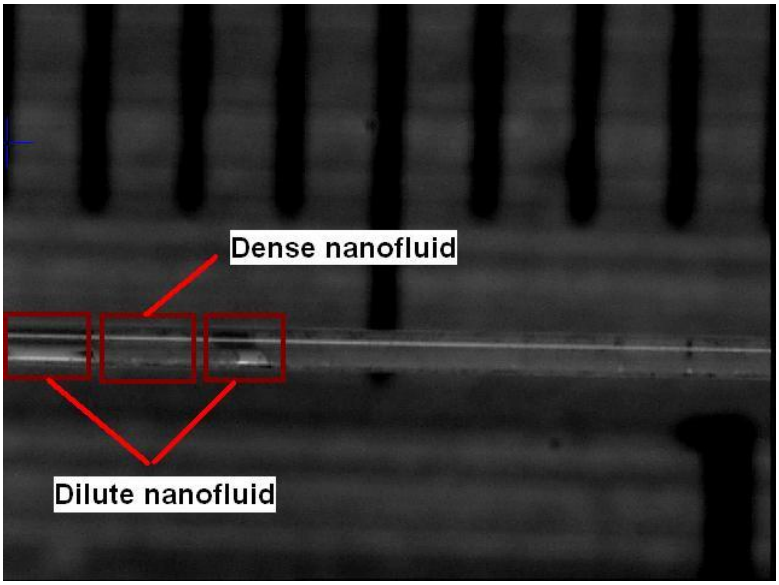

Figure 6-21: Train of plugs of dilute - dense nanofluid near capillary entrance.

Theory of capillary flow of nanofluids was derived in equation (6.58). This equation is however coupled with equations (6.42) and (4.15) to account for the dynamic contact angle and pendant droplet shape change respectively. The system of equations is as follows:

ATTENTION: The Singapore Copyright Act applies to the use of this document. Nanyang Technological University Library

$$\begin{cases} \text{A:} & 2\pi r\gamma\cos\theta - \gamma\dfrac{dA_{la,1}}{dx} = 2\pi x\,\eta_b F(\phi)K\left(3+\dfrac{1}{n}\right)^n \dfrac{U^n}{r^{n-1}} \\ \text{B:} & \gamma\left(\cos\theta^0 - \cos\theta\right) + W\left(H_\Pi\right) = \zeta U + \eta_b F(\phi)K\left(\dfrac{2n+1}{n}\right)^n \left(\dfrac{1+n}{1-n}\right) r^{1-n}\dfrac{U^n}{\theta^n} \\ \text{C:} & \dfrac{dA_{la,1}}{dx} = (V_0 - \pi r^2 x)^{2/3}\dfrac{dk}{dx} - \pi^{\frac{2}{3}} r^2 k\left(V_0 - \pi r^2 x\right)^{-1/3} \end{cases} \quad (6.60)$$

In equation (6.60), part A is a non-linear explicit ordinary differential equation. Solution to this equation can be easily done by numerical calculations such as Runge-Kutta 4th order method if the dynamic contact angle is an explicit function of velocity U. Despite, as is shown in part B, dynamic contact angle of non-Newtonian fluids is an implicit function of U. Part C also contains the non-dimensional pendant droplet geometry function (k) and its derivative (dk/dx) which has been previously obtained semi-empirically from experimental data (see *Sec.* Results and discussion, Chapter 4). Solution to this system of equations needs a numerical code to be written for this purpose[13]. However it is possible to simplify this equation and solve it with Runge-Kutta method using MATLAB. For this purpose it is assumed that the contact angle remains constant equal to the equilibrium contact angle (θ^0); also, the pendant droplet retains a spherical geometry with $k = \sqrt[3]{36\pi}$. Based on these simplifications, equation (6.60) reads:

$$2\pi r\gamma\cos\theta^0 + \tfrac{2}{3}\pi\gamma r^2 k\left(V_0 - \pi r^2 x\right)^{-1/3} = 2\pi x\,\eta_b F(\phi)K\left(3+\frac{1}{n}\right)^n \frac{U^n}{r^{n-1}} \quad (6.61)$$

Capillary flow from a beaker with an inlet arm

Figure 6-22 to Figure 6-24 show capillary flow of 2% and 1% TiO_2 – DI water nanofluids in 300, 500 and 700 μm capillary tubes. After the very fast initial wake of the meniscus, the displacement of the nanofluid in the capillary tube is gradual due to high viscous drag force.

[13] Advanced numerical algorithms such as Richardson extrapolation, Bulirsch-Stoer method can be used to handle these types of equations.

ATTENTION: The Singapore Copyright Act applies to the use of this document. Nanyang Technological University Library

Error bars are mainly due to the instabilities of nanofluid flow in these experiments. It was observed that if the capillary tube was inserted 5 mm from the nanofluid free surface into the beaker inlet arm, the nanofluid would travel the total length of the capillary tube. Otherwise, it was observed that the flow stopped at some distances before reaching to the capillary exit. From these figures, it is obvious that the rate of displacement in 2% is less than in 1% due to its higher viscosity. As compared to capillary flow in 500 and 700 μm capillary tubes, the difference between 1% nanofluid and 2% nanofluid displacements (experimental data) is less in 300 μm capillary tube. This effect is however attributed to adsorption of very dilute nanofluid instead of the actual concentrated nanofluid which occurs more prominently in 300 μm than in 500 and 700 μm capillary tubes due to its smaller size. This means that in capillary flow of 2% nanofluid in 300 μm capillary tube adsorption of very dilute nanofluid whose viscosity, surface tension etc. is closer to that of 1% nanofluid happens more significantly. It is also obvious that the same difference is less in 500 μm capillary tube than in 700 μm capillary tube.

Also shown in these figures are theoretical calculations of equation (6.61) with $k = 0$ and comparisons with experimental data. It is obvious that the simplified model overestimates capillary penetration at initial stages due to exclusion of dissipation of driver energy due to contact line friction and wedge film friction. Despite, after the initial stage, the model underestimates the experimental data. This is due to the above mentioned instability of nanofluid penetration when a dilute solution of less viscosity is absorbed instead of the true concentration of the nanofluid which is more viscous. The difference between theory and experiment is also higher in 2% nanofluid than in 1% nanofluid. Due to the very complex flow patterns and present instabilities which are due to complex interparticular interactions, modeling of this phenomenon is impossible.

ATTENTION: The Singapore Copyright Act applies to the use of this document. Nanyang Technological University Library

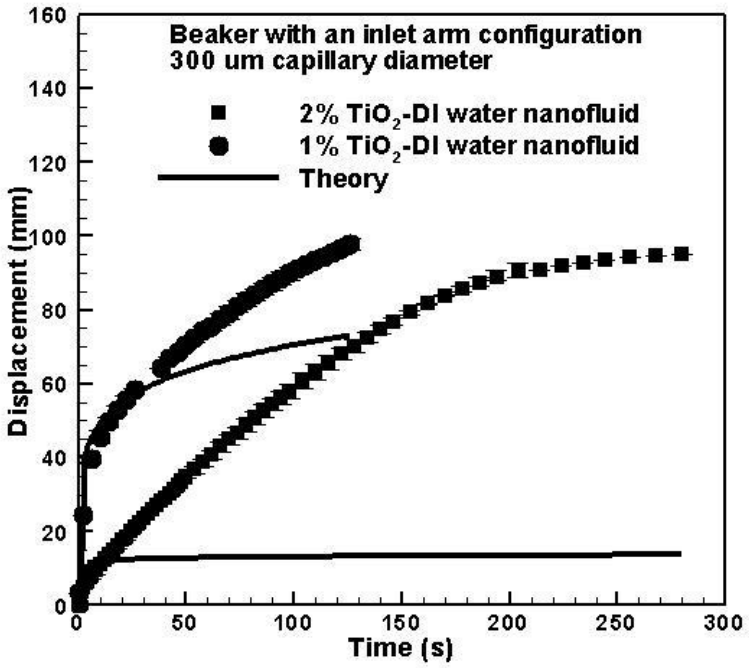

Figure 6-22: Capillary flow of 2% and 1% TiO_2 - DI water nanofluid in 300 µm capillary tube (beaker with an inlet arm configuration).

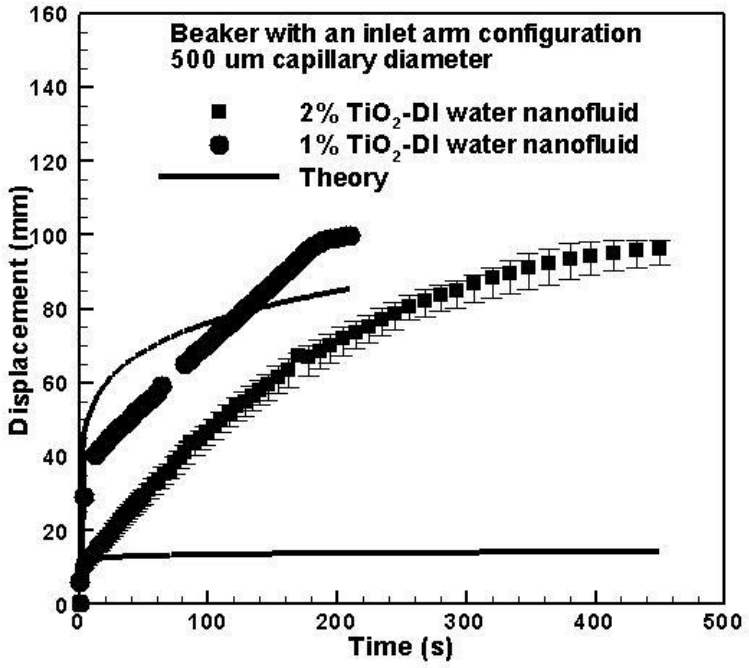

Figure 6-23: Capillary flow of 2% and 1% TiO_2 - DI water nanofluid in 500 µm capillary tube (beaker with an inlet arm configuration).

ATTENTION: The Singapore Copyright Act applies to the use of this document. Nanyang Technological University Library

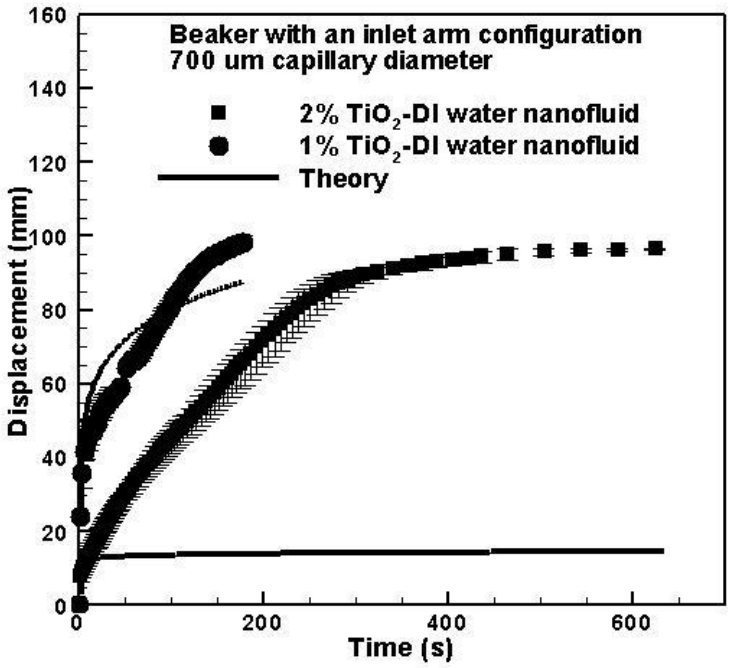

Figure 6-24: Capillary flow of 2% and 1% TiO_2 - DI water nanofluid in 700 µm capillary tube (beaker with an inlet arm configuration).

Capillary flow from a pendant droplet

Figure 6-25 to Figure 6-27 show capillary flow of 2% and 1% TiO_2 – DI water nanofluids in 300, 500 and 700 µm capillary tubes. The initial stage of penetration is very fast, followed by gradual displacement of the meniscus in the capillary tube. Error bars are mainly due to the instabilities of nanofluid flow in such experiments. In 300 µm capillary tube, the pendant droplet displaces the total length of the capillary tube; while penetration length in 500 µm and 700 µm capillaries are roughly 40 mm and 30 mm respectively. It is obvious that the rate of displacement in 2% is less than in 1% due to its higher viscosity. It is also obvious that in 300 µm capillary as compared to 500 and 700 µm capillaries, the difference between 1% nanofluid and 2% nanofluid is less. This is attributed to the instabilities (such as adsorption of very dilute nanofluid instead of the real concentrated nanofluid) which happen earlier and more prominent in 300 µm than in 500 and 700 µm capillary tubes. 500 and 700 µm capillary

ATTENTION: The Singapore Copyright Act applies to the use of this document. Nanyang Technological University Library

tubes have larger surface area and thus it is easier for the nanofluid to flow through the capillary tube. It is obvious that the same difference is less in 500 μm capillary tube than in 700 μm capillary tube.

Also shown in Figure 6-25 to Figure 6-27 are theoretical calculations of equation (6.61) and comparisons with experimental data. It is obvious that at initial stages of capillary flow the model overestimates the experimental data. This is because the simplified model excludes dissipation of driver energy due to contact line friction and wedge film friction. However, after the initial stage, the model underestimates the experimental data. This is due to the above mentioned instability of nanofluid penetration when a dilute solution is absorbed instead of the true higher concentration of the nanofluid. The other effect is the pendant droplet shape change. It was elaborated in Chapter 4 that the pendant droplet does not retain a spherical geometry during the process. Although a spherical approximation is used in this model as simplification to the complex form of equation (6.60), this approximation is only valid at initial stages of capillary flow after which deviation from a spherical geometry was shown to increase the rate of penetration.

For flow of 1% vol. concentration nanofluid in 700 μm capillary tube, it is obvious that the model overestimates the experimental data entirely since the penetration length is very small and the above mentioned instability does not occur in this case. As for the agreement between experimental data and theory, it is obvious that the model gives a better agreement for 1% vol. concentration than 2% vol. concentration. This is also attributed to the same instability which is more prominent in 2% vol. concentration than 1% vol. concentration.

ATTENTION: The Singapore Copyright Act applies to the use of this document. Nanyang Technological University Library

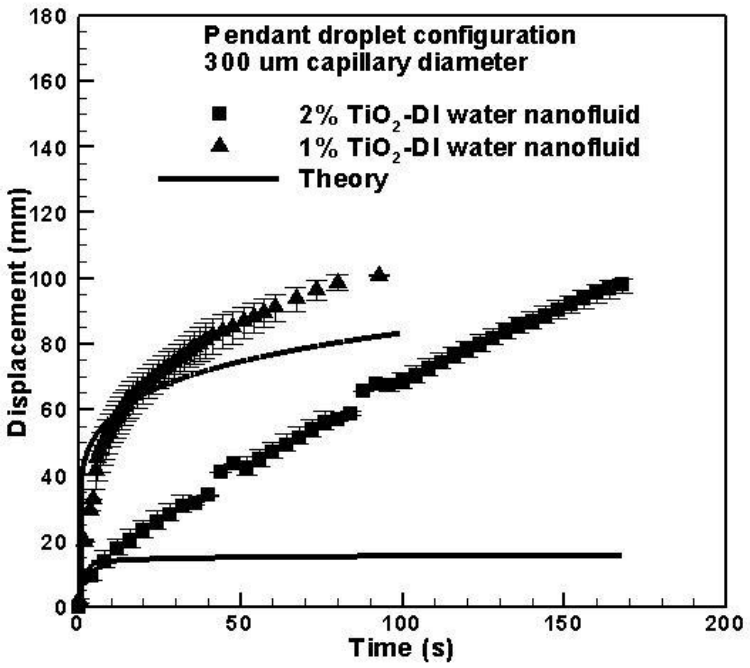

Figure 6-25: Capillary flow of 2% and 1% TiO_2 - DI water nanofluid in 300 µm capillary tube (pendant droplet configuration).

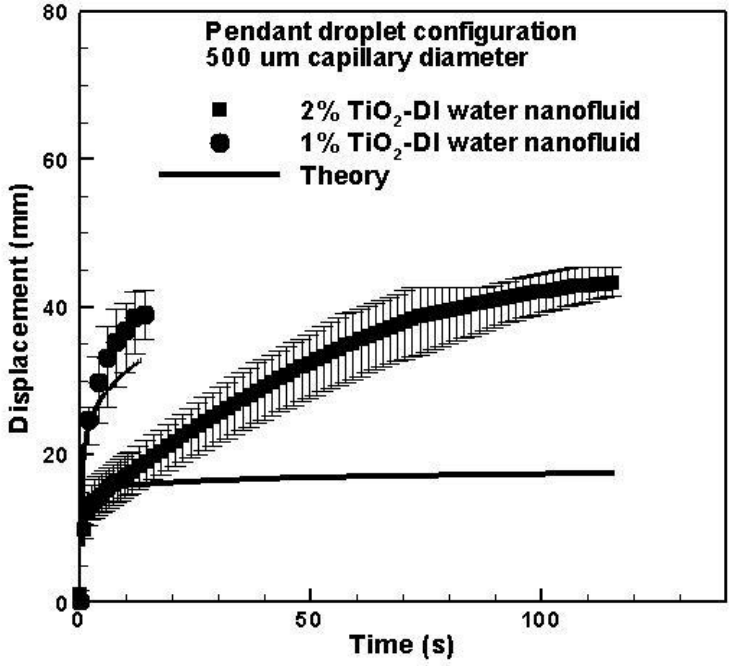

Figure 6-26: Capillary flow of 2% and 1% TiO_2 - DI water nanofluid in 500 µm capillary tube (pendant droplet configuration).

ATTENTION: The Singapore Copyright Act applies to the use of this document. Nanyang Technological University Library

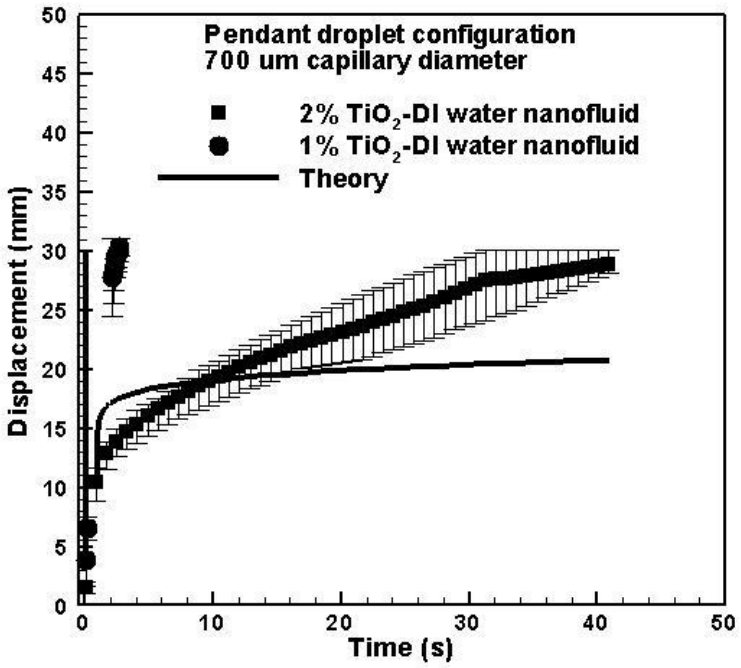

Figure 6-27: Capillary flow of 2% and 1% TiO_2 - DI water nanofluid in 500 µm capillary tube (pendant droplet configuration). For 1%, due to the very rapid motion of the meniscus only few points could be captured.

ATTENTION: The Singapore Copyright Act applies to the use of this document. Nanyang Technological University Library

Chapter 7: Conclusions and recommendations

1. Conclusions

In this thesis, it is aimed to investigate surface tension driven capillary flow of simple and complex fluids. As simple fluid, mixtures of glycerol and DI water are used, while as complex fluid, TiO_2 – DI water nanofluids are used. Initially (and as the basis for studying capillary flow behavior of nanofluids), capillarity of glycerol-DI water solutions of various glycerol concentrations are studied in two novel configurations. Firstly, surface tension driven flow in closed-end capillaries are studied with emphasis on the effects of pneumatic pressure of trapped air. Controlled experiments were carried out to examine the influence of capillary size and liquid viscosity on such capillary flow. It is found that the total distance travelled by the liquid column in a smaller radius capillary is longer. Although the viscosity of the liquids used in these experiments has little effect on the maximum displacement, a more viscous liquid shows a lower wetting velocity and thus takes a longer time to reach the maximum displacement. Additional experiments were performed with the attachment of syringes to provide larger enclosed air volume at the end of capillary. It is observed that for a larger attached volume, the total displacement is longer. The results of this study further suggest a potential application for the use of pneumatic pressure of trapped air as a controlling means to manipulate meniscus position and wetting velocity in capillary flows. Secondly, this thesis presents an investigation into the capillary flow from a pendant droplet. Controlled experiments were performed with liquid pendant droplets as finite sized reservoirs to examine the effect of reservoir size on capillary flow behavior and rate of penetration of liquids. It is observed that the change in pendant droplet surface area has significant effects on the dynamic behavior of such capillary system resulting in faster displacement of the

ATTENTION: The Singapore Copyright Act applies to the use of this document. Nanyang Technological University Library

meniscus. This method is also of practical importance where minute quantity of liquids is introduced in capillary systems. Based on these studies, the physicochemical and physical-statistical parameters controlling surface wettability and capillarity are understood. In continuance, spreading kinetics and capillary flow behavior of nanofluids are studied. This part of thesis elucidates the effects of nanoparticles and nanoparticle concentration on capillary and wetting properties of nanofluids. Firstly, the effects from nanoparticle concentration on the surface tension and equilibrium contact angle of TiO_2 – DI water nanofluids are studied. Surface tension measurements show that the higher is the nanoparticle concentration the lower is the surface tension. The Brownian motion of nanoparticles in the nanofluid-air interface is resulting in this reduction. Nanoparticles can also behave like surfactant molecules and be absorbed onto the interface, thus make a bridge between nanofluid and the surrounding air abating the surface tension. Measurements of equilibrium contact angle show that the higher is the nanoparticle concentration the higher is the nanofluid equilibrium contact angle. Two mechanisms are functioning to control the equilibrium shape and contact angle of nanofluid droplets on the solid surface. The first mechanism is attributed to agglomeration and clustering of nanoparticles which result in a reduction of the number of nanoparticles in the thin film in front of the bulk nanofluid. The second mechanism is attributed to adsorption of nanoparticles onto the solid surface resulting in solid surface modification and pinning of contact line. The study on the spreading dynamics of nanofluids reveals the effects of structural and depletion components of the disjoining pressure on the non-Newtonian nature of these nanofluids. Spreading starts from a primary region where the contact angle changes rapidly and most of the dissipations occur in the wedge film followed by a region where the contact angle changes gradually and the dominant dissipative mechanism is the contact line dissipation. Nanoparticles in the wedge film can change lubricating and rolling flow patterns and result in complex flow field

ATTENTION: The Singapore Copyright Act applies to the use of this document. Nanyang Technological University Library

structures thereof. Adsorption of nanoparticles to the solid surface influences the contact line dissipation. Finally, capillary flow behavior of nanofluids is studied. It was observed that due to the higher affinity of glass capillary to adsorb DI water than the mixture of DI water with TiO_2, the flow becomes unstable in sense that the concentration of penetrated nanofluid reduces gradually, and a train of plugs of concentrated nanofluid and dilute nanofluid forms near the capillary entrance. This effect is however less apparent for larger capillary diameters which can accommodate larger nanofluid volumes. It is also less apparent for 1% TiO_2 – DI water nanofluid than 2% TiO_2 – DI water nanofluid.

2. Recommendations

Although capillary wetting and interfacial phenomena in microstructures has been studied for quite a while, it is possible to further exploit its benefits and potential applications by introduction of new designs, also using new fluids in the systems. In this regard, comprehensive experimental and theoretical work is indeed needed. Recommendations for future work are as follow:

Application based research

Focusing on potential applications of surface tension driven flow in heat transfer of micro-electronics, the feasibility of using this method in cooling of electronic components can be studied by investigating capillary flow and spreading of fluids (nanofluids in terms of enhanced cooling) over mini- and micro-surfaces.

Computational investigations

Molecular dynamics and other computational methods such as Lattice Boltzmann method can be used to model molecular behavior of fluids in interaction with molecules of solid in mechanism of spreading over solid surface. In-depth information can be obtained from these

ATTENTION: The Singapore Copyright Act applies to the use of this document. Nanyang Technological University Library

simulations. More specifically, for nanofluids, interactions between nano-sized particles play an important role, which can be modeled by molecular dynamics and Brownian dynamics simulations. Such study can reveal unknown ideas like adsorption of nanoparticles to the surface of solid and formation of new adsorption sites over the solid surface. Also, with aid of computational fluid dynamics, it is possible to define a thorough model for pendant droplet shape change in process of penetration of a liquid pendant droplet into a capillary tube. Effect from air molecules in high pressure portion of the capillary tube on the advancing liquid interface can also be fully understood with aid of the same computational and simulation methods. Exact solution to very complex forms of the equations of capillarity of nanofluids can also be obtained by numerical codes. In addition, it should be noted that the flow in liquid front is 2D. In this thesis, to a very good approximation (due to low Capillary numbers) this effect is ignored, also since the length of the liquid head zone does not exceed a few radii and we have monitored total penetration of liquid, the above mentioned effect is indeed insignificant. Addition of this effect, however, will result in better predictions, although it makes the theory more complicated. Thus it is recommended that the effect be considered in numerical simulations.

Research on thermophysical properties of nanofluids

There is no systematic study on the surface tension and contact angle of nanofluids. Current works are usually performed for different types of nanoparticles and different types of solid surface; results also show controversy to theory. Due to presence of nanofluids in plenty of applications based wetting and capillarity, such study is imperative. For viscosity of nanofluids the current state of literature work seems to be thorough, despite lacking supportive work in the low-shear rate region.

Research on the capillary flow of nanofluids

ATTENTION: The Singapore Copyright Act applies to the use of this document. Nanyang Technological University Library

A very novel topic of research, capillary flow behavior of nanofluids needs considerable attention. At present there is no systematic study on capillarity of nanofluids. Preparation of viscous nanofluids (e.g., nanofluids based mixture of glycerol and DI water) not only makes the experiments easier, but also makes the samples more stable, thus can emphasize the effects of nanoparticles.

ATTENTION: The Singapore Copyright Act applies to the use of this document. Nanyang Technological University Library

References

1. Middleman, S., *High speed wire coating by withdrawal from a bath of viscoelastic liquid.* Polymer Engineering and Science, 1978. **18**(5): p. 355-358.
2. Grundke, K., et al., *Studies on the wetting behaviour of polymer melts on solid surfaces using the Wilhelmy balance method.* Colloids and Surfaces A: Physicochemical and Engineering Aspects, 1996. **116**(1-2): p. 93-104.
3. Masaaki Oda, S.S.H.Y.T.F., *Multilayer coating by drawing a thin plastic fiber through a polymer solution.* Asia-Pacific Journal of Chemical Engineering, 2008. **3**(1): p. 63-69.
4. Denoyel, R., I. Beurroies, and B. Lefevre, *Thermodynamics of wetting: information brought by microcalorimetry.* Journal of Petroleum Science and Engineering, 2004. **45**(3-4): p. 203-212.
5. Sciffer, S.D., G.M. Evans, and J.A. Lucas, *Hydrodynamic meniscus profiles in creeping flow.* Chemical Engineering Science, 1998. **53**(24): p. 4129-4133.
6. Schramm, L.L., E.N. Stasiuk, and M.D. Gerrard, *Surfactants and their applications.* Annual Reports on the Progress of Chemistry, Section C, 2003. **99**: p. 3–48.
7. Chaudhury, M.K., *Complex fluids: Spread the word about nanofluids.* Nature, 2003. **423**(6936): p. 131-132.
8. Skalak, R. and P.I. Branemark, *Deformation of Red Blood Cells in Capillaries.* Science, 1969. **164**(3880): p. 717-719.
9. Lominadze, D. and G. McHedlishvili, *Red Blood Cell Behavior at Low Flow Rate in Microvessels.* Microvascular Research, 1999. **58**(2): p. 187-189.
10. Secomb, T.W., R. Hsu, and A.R. Pries, *Blood Flow and Red Blood Cell Deformation in Nonuniform Capillaries: Effects of the Endothelial Surface Layer.* Microcirculation, 2002. **9**(3): p. 189-196.
11. Eijkel, J.C. and A. van den Berg, *Young 4ever--the use of capillarity for passive flow handling in lab on a chip devices.* Lab on a Chip, 2006. **6**(11): p. 1405-8.
12. Jeong, J.H., et al., *Measurement of RBC deformation and velocity in capillaries in vivo.* Microvascular Research, 2006. **71**(3): p. 212-217.
13. Berthier, E. and D.J. Beebe, *Flow rate analysis of a surface tension driven passive micropump.* Lab on a Chip, 2007. **7**(11): p. 1475-1478.
14. Ju, J., et al., *Backward flow in a surface tension driven micropump.* Journal of Micromechanics and Microengineering, 2008. **18**(8): p. 087002.
15. McHedlishvili, G. and N. Maeda, *Blood flow structure related to red cell flow: a determinant of blood fluidity in narrow microvessels.* Japanese Journal of Physiology, 2001. **51**: p. 19-30.
16. Huang, W., R.S. Bhullar, and Y.C. Fung, *The Surface-Tension-Driven Flow of Blood From a Droplet Into a Capillary Tube.* Journal of Biomechanical Engineering, 2001. **123**(5): p. 446-454.
17. Wapner, P.G. and W.P. Hoffman, *Utilization of surface tension and wettability in the design and operation of microsensors.* Sensors and Actuators B: Chemical, 2000. **71**(1-2): p. 60-67.

ATTENTION: The Singapore Copyright Act applies to the use of this document. Nanyang Technological University Library

18. Hisamoto, H., et al., *Capillary-Assembled Microchip for Universal Integration of Various Chemical Functions onto a Single Microfluidic Device.* Analytical Chemistry, 2004. **76**(11): p. 3222-3228.
19. Atencia, J. and D.J. Beebe, *Controlled microfluidic interfaces.* Nature, 2005. **437**(7059): p. 648-655.
20. Erickson, D., D. Li, and C.B. Park, *Numerical Simulations of Capillary-Driven Flows in Nonuniform Cross-Sectional Capillaries.* Journal of colloid and interface science, 2002. **250**(2): p. 422-430.
21. Tsori, Y., *Discontinuous Liquid Rise in Capillaries with Varying Cross-Sections.* Langmuir, 2006. **22**(21): p. 8860-8863.
22. Jicun Lu, S.C. Busch, and D.F. Baldwin, *Solder wetting in a wafer-level flip chip assembly*, in *51st Electronic Components and Technology Conference*. 2001: Orlando, FL, USA. p. 372-377.
23. Wan, J.W., W.J. Zhang, and D.J. Bergstrom, *Recent advances in modeling the underfill process in flip-chip packaging.* Microelectronics Journal, 2007. **38**(1): p. 67-75.
24. Zou, M., L. Cai, and H. Wang, *Adhesion and friction studies of a nano-textured surface produced by spin coating of colloidal silica nanoparticle solution.* Tribology Letters, 2006. **21**(1): p. 25-30.
25. Schramm, L.L., *The influence of suspension viscosity on bitumen rise velocity and potential recovery in the hot water flotation process for oil sands.* Journal of Canadian Petroleum Technology, 1999. **28**(3): p. 73-80.
26. Wasan, D.T. and A.D. Nikolov, *Spreading of nanofluids on solids.* Nature, 2003. **423**(6936): p. 156-159.
27. Nguyen, C.T., et al., *Heat transfer enhancement using Al2O3-water nanofluid for an electronic liquid cooling system.* Applied Thermal Engineering, 2007. **27**(8-9): p. 1501-1506.
28. Duursma, G., K. Sefiane, and A. Kennedy, *Experimental Studies of Nanofluid Droplets in Spray Cooling.* Heat Transfer Engineering, 2009. **30**(13): p. 1108 - 1120.
29. Miller, C.A. and P. Neogi, *Interfacial phenomena : equilibrium and dynamic effects*. 2nd ed. Surfactant science series ; v. 139. 2008, Boca Raton: CRC Press/Taylor & Francis. 501 p.
30. Young, T., *An Essay on the Cohesion of Fluids.* Philosophical Transactions of the Royal Society of London, 1805. **95**: p. 65-87.
31. Hartland, S., *Surface and interfacial tension : measurement, theory, and applications*. Surfactant science series ; v. 119. 2004, New York ; Basel: Marcel Dekker. x, 619 p.
32. Washburn, E.W., *The Dynamics of Capillary Flow.* Physical Review, 1921. **17**(3): p. 273-283.
33. Ralston, J., M. Popescu, and R.V. Sedev, *Dynamics of Wetting from an Experimental Point of View.* The Annual Review of Material Research, 2008. **38**: p. 23-43.
34. Richards, L.A., *Capillary conduction of liquids in porous mediums.* Physics, 1931. **1**: p. 318-333.
35. Miller, E.E. and R.D. Miller, *Physical Theory for Capillary Flow Phenomena.* Journal of Applied Physics, 1956. **27**(4): p. 324-332.
36. de Gennes, P.G., *Wetting: statics and dynamics.* Reviews of Modern Physics, 1985. **57**(3): p. 827.

ATTENTION: The Singapore Copyright Act applies to the use of this document. Nanyang Technological University Library

37. Newman, S., *Kinetics of Wetting of Surfaces by Polymers: Capillary Flow.* J. Colloid Interface Sci, 1968. **26**: p. 209–213.
38. Cherry, B.W. and C.M. Holmes, *Kinetics of wetting of surfaces by polymers.* J. Colloid Interface Sci, 1969. **29**(1): p. 174–176.
39. Blake, T.D. and J.M. Haynes, *Kinetics of liquid/liquid displacement.* J. Colloid Interface Sci, 1969. **30**(3): p. 421–423.
40. Hayes, R.A. and J. Ralston, *The molecular-kinetic theory of wetting.* Langmuir, 1994. **10**(1): p. 340-342.
41. Hamraoui, A., et al., *Can a Dynamic Contact Angle Be Understood in Terms of a Friction Coefficient?* Journal of colloid and interface science, 2000. **226**(2): p. 199-204.
42. Sobolev, V.D., et al., *Surface Tension and Dynamic Contact Angle of Water in Thin Quartz Capillaries.* Journal of colloid and interface science, 2000. **222**(1): p. 51-54.
43. Hamraoui, A. and T. Nylander, *Analytical Approach for the Lucas-Washburn Equation.* Journal of colloid and interface science, 2002. **250**(2): p. 415-421.
44. Blake, T.D. and J. De Coninck, *The influence of solid-liquid interactions on dynamic wetting.* Advances in Colloid and Interface Science, 2002. **96**(1-3): p. 21-36.
45. Martic, G., J. De Coninck, and T.D. Blake, *Influence of the dynamic contact angle on the characterization of porous media.* Journal of colloid and interface science, 2003. **263**(1): p. 213-216.
46. Vega, M.J., et al., *Experimental Investigation of the Link between Static and Dynamic Wetting by Forced Wetting of Nylon Filament.* Langmuir, 2007. **23**(21): p. 10628-10634.
47. Blake, T.D., *Dynamic contact angles and wetting kinetics.* Wettability, Marcel Dekker, New York, 1993: p. 251–309.
48. Schneemilch, M., et al., *Dynamic Wetting and Dewetting of a Low-Energy Surface by Pure Liquids.* Langmuir, 1998. **14**(24): p. 7047-7051.
49. Petrov, J.G., et al., *Dynamics of Partial Wetting and Dewetting in Well-Defined Systems.* J. Phys. Chem. B, 2003. **107**(7): p. 1634-1645.
50. Petrov, J.G., et al., *Dynamics of Partial Wetting and Dewetting of an Amorphous Fluoropolymer by Pure Liquids.* Langmuir, 2003. **19**(7): p. 2795-2801.
51. Blake, T.D., *The physics of moving wetting lines.* Journal of colloid and interface science, 2006. **299**(1): p. 1-13.
52. Huh, C. and L.E. Scriven, *Hydrodynamic model of steady movement of a solid/liquid/fluid contact line.* Journal of colloid and interface science, 1971. **35**(1): p. 85-101.
53. Phillips, M.C. and A.C. Riddiford, *Dynamic contact angles. II. Velocity and relaxation effects for various liquids.* Journal of colloid and interface science, 1972. **41**(1): p. 77-85.
54. Elliott, G.E.P. and A.C. Riddiford, *Dynamic Contact Angles and Rates of Adsorption.* Nature, 1962. **195**(4843): p. 795-796.
55. Voinov, O.V., *Hydrodynamics of wetting.* Fluid Dynamics, 1976. **11**(5): p. 714-721.
56. Thompson, P.A. and M.O. Robbins, *Simulations of contact-line motion: Slip and the dynamic contact angle.* Physical Review Letters, 1989. **63**(7): p. 766.
57. Cox, R.G., *The dynamics of the spreading of liquids on a solid surface. Part 1.* Viscous flow. J. Fluid Mech, 1986. **168**: p. 169.
58. Levine, S., et al., *A theory of capillary rise of a liquid in a vertical cylindrical tube and in a parallel-plate channel.* J. Colloid Interf. Sci, 1980. **73**: p. 136–151.

ATTENTION: The Singapore Copyright Act applies to the use of this document. Nanyang Technological University Library

59. Shikhmurzaev, Y.D., *Moving contact lines in liquid/liquid/solid systems.* Journal of Fluid Mechanics, 1997. **334**: p. 211-249.
60. Blake, T.D. and Y.D. Shikhmurzaev, *Dynamic Wetting by Liquids of Different Viscosity.* Journal of colloid and interface science, 2002. **253**(1): p. 196-202.
61. Mumley, T.E., C.J. Radke, and M.C. Williams, *Kinetics of liquid/liquid capillary rise. I: Experimental observations.* Journal of colloid and interface science, 1986. **109**(2): p. 398-412.
62. Mumley, T.E., C.J. Radke, and M.C. Williams, *Kinetics of liquid/liquid capillary rise. II: Development and test of theory.* Journal of colloid and interface science, 1986. **109**(2): p. 413-425.
63. Petrov, J.G. and P.G. Petrov, *Forced advancement and retraction of polar liquids on a low energy surface.* Colloids and Surfaces, 1992. **64**(2): p. 143-149.
64. Petrov, P.G. and J.G. Petrov, *Comparison of the static and dynamic contact angle hysteresis at low velocities of the three-phase contact line.* Colloids and Surfaces, 1991. **61**: p. 227-240.
65. Petrov, P. and I. Petrov, *A combined molecular-hydrodynamic approach to wetting kinetics.* Langmuir, 1992. **8**(7): p. 1762-1767.
66. Sedev, R.V., et al., *Dynamic Contact Angles at Low Velocities.* Journal of colloid and interface science, 1993. **159**(2): p. 392-399.
67. de Ruijter, M.J., et al., *Contact Angle Relaxation during the Spreading of Partially Wetting Drops.* Langmuir, 1997. **13**(26): p. 7293-7298.
68. Jeje, A.A., *Rates of Spontaneous Movement of Water in Capillary Tubes.* J. Coll. Interface Sci, 1979. **69**: p. 420–429.
69. Siebold, A., et al., *Effect of dynamic contact angle on capillary rise phenomena.* Colloids and Surfaces A: Physicochemical and Engineering Aspects, 2000. **161**(1): p. 81-87.
70. Quéré, D., *Inertial capillarity.* EPL (Europhysics Letters), 1997. **39**(5): p. 533.
71. Zhmud, B.V., F. Tiberg, and K. Hallstensson, *Dynamics of Capillary Rise.* Journal of colloid and interface science, 2000. **228**(2): p. 263-269.
72. Stange, M., M.E. Dreyer, and H.J. Rath, *Capillary driven flow in circular cylindrical tubes.* Physics of Fluids, 2003. **15**(9): p. 2587-2601.
73. Marmur, A., *Drop penetration into a thin porous medium.* Journal of colloid and interface science, 1988. **123**(1): p. 161-169.
74. Marmur, A., *The radial capillary.* Journal of colloid and interface science, 1988. **124**(1): p. 301-308.
75. Denesuk, M., et al., *Capillary Penetration of Liquid Droplets into Porous Materials.* Journal of colloid and interface science, 1993. **158**(1): p. 114-120.
76. Seveno, D., et al., *Spreading Drop Dynamics on Porous Surfaces.* Langmuir, 2002. **18**(20): p. 7496-7502.
77. Marmur, A., *A mechanism for complete spontaneous displacement of a liquid from a capillary.* Journal of colloid and interface science, 1989. **130**(1): p. 288-289.
78. Marmur, A., *Kinetics of displacement of a liquid from a capillary: the effect of limited reservoirs.* Chemical Engineering Science, 1989. **44**(7): p. 1511-1517.
79. Marmur, A., *Penetration and displacement in capillary systems of limited size.* Advances in Colloid and Interface Science, 1992. **39**: p. 13-33.
80. Rauscher, M. and S. Dietrich, *Wetting Phenomena in Nanofluidics.* The Annual Review of Materials Research, 2008. **38**: p. 143–72.

ATTENTION: The Singapore Copyright Act applies to the use of this document. Nanyang Technological University Library

81. Cox, R.G., *The dynamics of the spreading of liquids on a solid surface. Part 1: Viscous flow.* . J. Fluid Mech, 1986. **168**: p. 169-194.
82. Trokhymchuk, A., et al., *A Simple Calculation of Structural and Depletion Forces for Fluids/Suspensions Confined in a Film.* Langmuir, 2001. **17**(16): p. 4940-4947.
83. Chengara, A., et al., *Spreading of nanofluids driven by the structural disjoining pressure gradient.* Journal of Colloid and Interface Science, 2004. **280**(1): p. 192-201.
84. Matar, O.K., R.V. Craster, and K. Sefiane, *Dynamic spreading of droplets containing nanoparticles.* Physical Review E (Statistical, Nonlinear, and Soft Matter Physics), 2007. **76**(5): p. 056315-9.
85. Vafaei, S. and et al., *Effect of nanoparticles on sessile droplet contact angle.* Nanotechnology, 2006. **17**(10): p. 2523.
86. Sefiane, K., J. Skilling, and J. MacGillivray, *Contact line motion and dynamic wetting of nanofluid solutions.* Advances in Colloid and Interface Science, 2008. **138**(2): p. 101-120.
87. Krieger, I.M., *Rheology of monodisperse latices.* Advances in Colloid and Interface Science, 1972. **3**(2): p. 111-136.
88. Leighton, D. and A. Acrivos, *The shear-induced migration of particles in concentrated suspensions.* J. Fluid Mech, 1987. **181**: p. 415-439.
89. Morris, J.F. and F. Boulay, *Curvilinear flows of noncolloidal suspensions: The role of normal stresses.* Journal of Rheology, 1999. **43**(5): p. 1213-1237.
90. Phillips, R.J., et al., *A constitutive equation for concentrated suspensions that accounts for shear-induced particle migration.* Physics of Fluids A: Fluid Dynamics, 1992. **4**(1): p. 30-40.
91. Wang, X., X. Xu, and U.S. Choi, *Thermal Conductivity of Nanoparticle - Fluid Mixture.* Journal of Thermophysics and Heat Transfer, 1999. **13**.
92. Prasher, R., et al., *Parametric experimental study of viscosity of nanofluids*, in *Proceedings of IMECE, ASME International Mechanical Engineering Congress & Exposition*. 2006: Chicago, Illinois. p. 5-10.
93. Prasher, R., et al., *Measurements of nanofluid viscosity and its implications for thermal applications.* Applied Physics Letters, 2006. **89**(13): p. 133108-3.
94. Schmidt, A.J., et al., *Experimental investigation of nanofluid shear and longitudinal viscosities.* Applied Physics Letters, 2008. **92**(24): p. 244107-3.
95. Garg, J., et al., *Enhanced thermal conductivity and viscosity of copper nanoparticles in ethylene glycol nanofluid.* Journal of Applied Physics, 2008. **103**(7): p. 074301-6.
96. Murshed, S.M.S. and N.-T. Nguyen, *Characterization of Temperature Dependence of Interfacial Tension and Viscosity of Nanofluid.* ASME Conference Proceedings, 2008. **2008**(42924): p. 545-548.
97. Pastoriza-Gallego, M.J., et al., *A study on stability and thermophysical properties (density and viscosity) of Al[sub 2]O[sub 3] in water nanofluid.* Journal of Applied Physics, 2009. **106**(6): p. 064301-8.
98. Yu, W., et al., *Investigation of thermal conductivity and viscosity of ethylene glycol based ZnO nanofluid.* Thermochimica Acta, 2009. **491**(1-2): p. 92-96.
99. Schaflinger, U., A. Acrivos, and K. Zhang, *Viscous resuspension of a sediment within a laminar and stratified flow.* International Journal of Multiphase Flow, 1990. **16**(4): p. 567-578.

ATTENTION: The Singapore Copyright Act applies to the use of this document. Nanyang Technological University Library

100. Brady, J.F., *The rheological behavior of concentrated colloidal dispersions.* The Journal of Chemical Physics, 1993. **99**(1): p. 567-581.
101. van der Werff, J.C. and C.G. de Kruif, *Hard-sphere Colloidal Dispersions: The Scaling of Rheological Properties with Particle Size, Volume Fraction, and Shear Rate.* Journal of Rheology, 1989. **33**(3): p. 421-454.
102. Frank, M., et al., *Particle migration in pressure-driven flow of a Brownian suspension.* Journal of Fluid Mechanics, 2003. **493**(-1): p. 363-378.
103. Aussillous, P. and D. Quere, *Liquid marbles.* Nature, 2001. **411**(6840): p. 924-927.
104. Aussillous, P. and D. Quere, *Properties of liquid marbles.* Proceedings of the Royal Society A: Mathematical, Physical and Engineering Science, 2006. **462**(2067): p. 973-999.
105. McEleney, P., et al., *Liquid marble formation using hydrophobic powders.* Chemical Engineering Journal, 2009. **147**(2-3): p. 373-382.
106. S Vafaei, T.B.-T.M.Z.P.A.P.G.R. and P.M. Ajayan, *Effect of nanoparticles on sessile droplet contact angle.* Nanotechnology, 2006. **17**(10): p. 2523.
107. Trokhymchuk, A., D. Henderson, and D.T. Wasan, *A Molecular Theory of the Hydration Force in an Electrolyte Solution.* Journal of Colloid and Interface Science, 1999. **210**(2): p. 320-331.
108. Piech, M. and J.Y. Walz, *Analytical Expressions for Calculating the Depletion Interaction Produced by Charged Spheres and Spheroids.* Langmuir, 2000. **16**(21): p. 7895-7899.
109. Walley, K.P., et al., *Structure of confined alkane liquids.* The Journal of Chemical Physics, 1994. **100**(4): p. 3361-3364.
110. Kralchevsky, P.A. and N.D. Denkov, *Analytical expression for the oscillatory structural surface force.* Chemical Physics Letters, 1995. **240**(4): p. 385-392.
111. Schoen, M., T. Gruhn, and D.J. Diestler, *Solvation forces in thin films confined between macroscopically curved substrates.* The Journal of Chemical Physics, 1998. **109**(1): p. 301-311.
112. Israelachvili, J.N., *Intermolecular and Surface Forces 2nd edn (London: Academic).* 1992.
113. S M Sohel Murshed, S.-H.T. and N. Nam-Trung, *Temperature dependence of interfacial properties and viscosity of nanofluids for droplet-based microfluidics.* Journal of Physics D: Applied Physics, 2008. **41**(8): p. 085502.
114. Radiom, M., W.K. Chan, and C. Yang, *Capillary filling with the effect of pneumatic pressure of trapped air.* Microfluidics and Nanofluidics, 2009. **Accepted**.
115. *CRC handbook of chemistry and physics*. 87 ed. 1977, Cleveland, Ohio: CRC Press.
116. *Drop Shape Analysis*, in *FTA200 Software Version 2.0 User Manual*. 2002, First Ten Angstroms.
117. Clanet, C., et al., *Onset of menisci.* Journal of Fluid Mechanics, 2002. **460**(-1): p. 131-149.
118. Radiom, M., W. Chan, and C. Yang, *A study of capillary flow from a pendant droplet.* Microfluidics and Nanofluidics (Article in Press), 2009.
119. Loung, L.T., *Study of Surface Tension Driven Flow in Microchannels*, in *Mechanical and Aerospace Engineering*. 2007, Nanayang Technological University: Singapore.
120. Junting, L.J., *Study of Surface Tension Driven Flow in Microchannels*, in *Mechanical and Aerospace Engineering*. 2008, Nanyang Technological University: Singapore.

ATTENTION: The Singapore Copyright Act applies to the use of this document. Nanyang Technological University Library

121. Brackbill, J.U., D.B. Kothe, and C. Zemach, *A continuum method for modeling surface tension.* Journal of Computational Physics, 1992. **100**(2): p. 335-354.
122. Ichikawa, N. and Y. Satoda, *Interface Dynamics of Capillary Flow in a Tube under Negligible Gravity Condition.* Journal of colloid and interface science, 1994. **162**: p. 350-350.
123. Barraza, H.J., S. Kunapuli, and E.A. O'Rear, *Advancing Contact Angles of Newtonian Fluids During "High" Velocity, Transient, Capillary-Driven Flow in a Parallel Plate Geometry.* Journal of Physical Chemistry B, 2002. **106**(19): p. 4979-4987.
124. Roseveare, W.E., R.E. Powell, and H. Eyring, *The Structure and Dynamics of Liquids.* Journal of Applied Physics, 1941. **12**(9): p. 669-679.
125. Akers, H.A. and D.G. Gabler, *The molar volume of solutes in water.* Naturwissenschaften, 1991. **78**(9): p. 417-419.
126. TE-XIAN, C.L., *Study of Surface Tension Driven Flow in Microcapillaries*, in *Mechanical and Aerospace Engineering*. 2008, Nanyang Technological University: Singapore.
127. Chan, W.K. and C. Yang, *Surface-tension-driven liquid?liquid displacement in a capillary.* Journal of Micromechanics and Microengineering, 2005. **15**(9): p. 1722.
128. Marmur, A., *Kinetics of penetration into uniform porous media: Testing the equivalent-capillary concept.* Langmuir, 2003. **19**(14): p. 5956-5959.
129. Marmur, A., *Penetration of a small drop into a capillary.* Journal of colloid and interface science, 1988. **122**(1): p. 209-219.
130. Wang, X.Q. and A.S. Mujumdar, *A review on nanofluids - part I: theoretical and numerical investigations.* Brazilian Journal of Chemical Engineering, 2008. **25**(4).
131. Murshed, S.M.S., K.C. Leong, and C. Yang, *Enhanced thermal conductivity of TiO2--water based nanofluids.* International Journal of Thermal Sciences, 2005. **44**(4): p. 367-373.
132. Hong, K.S., T.-K. Hong, and H.-S. Yang, *Thermal conductivity of Fe nanofluids depending on the cluster size of nanoparticles.* Applied Physics Letters, 2006. **88**(3): p. 031901-3.
133. Wiacek, A. and E. Chibowski, *Zeta potential, effective diameter and multimodal size distribution in oil/water emulsion.* Colloids and Surfaces A: Physicochemical and Engineering Aspects, 1999. **159**(2-3): p. 253-261.
134. Lee, D., J.-W. Kim, and B.G. Kim, *A New Parameter to Control Heat Transport in Nanofluids: Surface Charge State of the Particle in Suspension.* The Journal of Physical Chemistry B, 2006. **110**(9): p. 4323-4328.
135. Hunter, R.J., *Measuring zeta potential in concentrated industrial slurries.* Colloids and Surfaces A: Physicochemical and Engineering Aspects, 2001. **195**(1-3): p. 205-214.
136. Morita, A., D. Carastan, and N. Demarquette, *Influence of drop volume on surface tension evaluated using the pendant drop method.* Colloid & Polymer Science, 2002. **280**(9): p. 857-864.
137. Rai, P.K., M.M. Denn, and C. Maldarelli, *Interfacial Tension of Liquid Crystalline Droplets.* Langmuir, 2003. **19**(18): p. 7370-7373.
138. Xu, L., et al., *Contact line mobility in liquid droplet spreading on rough surface.* Journal of Colloid and Interface Science, 2008. **323**(1): p. 126-132.
139. Schonhorn, H., *Theoretical Relationship between Surface Tension and Cohesive Energy Density.* The Journal of Chemical Physics, 1965. **43**(6): p. 2041-2043.

ATTENTION: The Singapore Copyright Act applies to the use of this document. Nanyang Technological University Library

140. Becher, P., *The calculation of cohesive energy density from the surface tension of liquids.* Journal of Colloid and Interface Science, 1972. **38**(2): p. 291-293.
141. Vavruca, I., *On the determination of the factor between cohesive energy density and surface tension.* Journal of Colloid and Interface Science, 1978. **63**(3): p. 600-601.
142. Murshed, S.M.S. and et al., *Temperature dependence of interfacial properties and viscosity of nanofluids for droplet-based microfluidics.* Journal of Physics D: Applied Physics, 2008. **41**(8): p. 085502.
143. Binks, B.P., *Particles as surfactants--similarities and differences.* Current Opinion in Colloid & Interface Science, 2002. **7**(1-2): p. 21-41.
144. Nguyen, A.V. and H.J. Schulze, *Colloidal science of flotation*. 2004, New York: Marcel Dekker. xix, 850 p.
145. Radiom, M., W. Chan, and C. Yang, *A study of capillary flow from a pendant droplet.* Microfluidics and Nanofluidics.
146. Deegan, R.D., *Pattern formation in drying drops.* Physical Review E, 2000. **61**(1): p. 475.
147. Sefiane, K. and R. Bennacer, *Nanofluids droplets evaporation kinetics and wetting dynamics on rough heated substrates.* Advances in Colloid and Interface Science. **147-148**: p. 263-271.
148. Sikalo, S., C. Tropea, and E.N. Ganic, *Dynamic wetting angle of a spreading droplet.* Experimental Thermal and Fluid Science, 2005. **29**(7): p. 795-802.
149. Carre, A. and P. Woehl, *Spreading of Silicone Oils on Glass in Two Geometries.* Langmuir, 2005. **22**(1): p. 134-139.
150. Wang, M.-J., et al., *Dynamic Behaviors of Droplet Impact and Spreading: Water on Five Different Substrates.* Langmuir, 2009. **25**(12): p. 6772-6780.
151. Smith, J.T., B.L. Viglianti, and W.M. Reichert, *Spreading Diagrams for the Optimization of Quill Pin Printed Microarray Density.* Langmuir, 2002. **18**(16): p. 6289-6293.
152. Wang, X.D., et al., *Spreading Dynamics and Dynamic Contact Angle of Non-Newtonian Fluids.* Langmuir, 2007. **23**(15): p. 8042-8047.
153. Marmur, A., *Equilibrium and spreading of liquids on solid surfaces.* Advances in Colloid and Interface Science, 1983. **19**(1-2): p. 75-102.
154. Fraaije, J.G.E.M. and A.M. Cazabat, *Dynamics of spreading on a liquid substrate.* Journal of Colloid and Interface Science, 1989. **133**(2): p. 452-460.
155. Chen, J.-D. and N. Wada, *Edge profiles and dynamic contact angles of a spreading drop.* Journal of Colloid and Interface Science, 1992. **148**(1): p. 207-222.
156. Sikalo, S., et al., *Dynamic contact angle of spreading droplets: Experiments and simulations.* Physics of Fluids, 2005. **17**(6): p. 062103-13.
157. de Ruijter, M., et al., *Effect of temperature on the dynamic contact angle.* Colloids and Surfaces A: Physicochemical and Engineering Aspects, 1998. **144**(1-3): p. 235-243.
158. White, F.M., *Fluid mechanics*. 4th ed. 1999, Boston, Mass.: WCB/McGraw-Hill. xiv, 825 p.

ATTENTION: The Singapore Copyright Act applies to the use of this document. Nanyang Technological University Library

Appendix A: Functions of the variables in the film interaction energy equation and the disjoining pressure equation

In the equation of the film interaction energy and equation of the disjoining pressure, functions of the variables are as follows (see Trokhymchuk et al. [82]):

$$W_1 = -2\sigma - W_0 \cos\left(\omega d + \varphi_W\right) e^{-\kappa d}$$

$$\Pi_1 = \rho kTZ - P - \Pi_0 \cos\left(\omega d + \varphi_\Pi\right) e^{-\kappa d}$$

$$Z = \exp\left(\beta \Delta\mu\right)$$

$$\delta = \frac{\Pi_1}{W_1}$$

Functions for the osmotic pressure P, excess chemical potential $\Delta\mu$, and the solid-fluid interfacial tension σ are as follows:

$$P = \rho kT \frac{1+\phi+\phi^2-\phi^3}{(1-\phi)^3}$$

$$\beta\Delta\mu = \phi \frac{8-9\phi+3\phi^2}{(1-\phi)^3}$$

$$\sigma = -\frac{9}{2\pi} kT \frac{\phi^2}{d^2} \frac{1+\phi}{(1-\phi)^3}$$

ATTENTION: The Singapore Copyright Act applies to the use of this document. Nanyang Technological University Library

Moreover, both the inverse decay length κ and oscillation frequency ω are explicit functions of particle volume fraction ϕ and particle diameter d as follows:

$$\kappa = \frac{1}{d}\left(4.78366 - 19.64378\phi + 37.37944\phi^2 - 30.59647\phi^3\right)$$
$$\omega = \frac{1}{d}\left(4.45160 + 7.10586\phi - 8.39671\phi^2 + 8.29751\phi^3\right)$$

Polynomial expansions for the amplitudes W_0 and $\prod_0$ and phases φ_W and φ_Π are as follows:

$$W_0 = \frac{1}{\beta d^2}\left(0.57909 + 0.83439\phi + 8.65315\phi^2\right)$$
$$\prod_0 = \frac{1}{\beta d^3}\left(4.06281 - 3.10572\phi + 76.67381\phi^2\right)$$

$$\varphi_W = 0.40095 + 2.10336\phi$$
$$\varphi_\Pi = -0.39687 - 0.3948\phi + 2.3027\phi^2$$

ATTENTION: The Singapore Copyright Act applies to the use of this document. Nanyang Technological University Library

Appendix B: Material properties

Table 1: Material properties of water, and glycerol.

Pure liquids	water	glycerol
Viscosity $[Pa.s]$	0.001002	0.780458
Density $[kg/m^3]$	1000	1261.1
Surface tension $[N/m]$	0.072	0.0625

Table 2: Material properties of aqueous glycerol solutions.

Liquid concentration	1:1 glycerol/ DI water	2:1 glycerol/ DI water	4:1 glycerol/ DI water	6:1 glycerol/ DI water	8:1 glycerol/ DI water	10:1 glycerol/ DI water
Viscosity $[Pa.s]$	0.008349	0.027625	0.08	0.16527	0.32522	0.45377
Density $[kg/m^3]$	1142	1187	1220	1231	1238	1242
Surface tension $[N/m]$	0.067	0.067	0.066	0.0647	0.0643	0.064